Bentho-pelagic transport of methanotrophs at methane gas seep sites

Parametrization, identification, and contribution to the pelagic methane sink

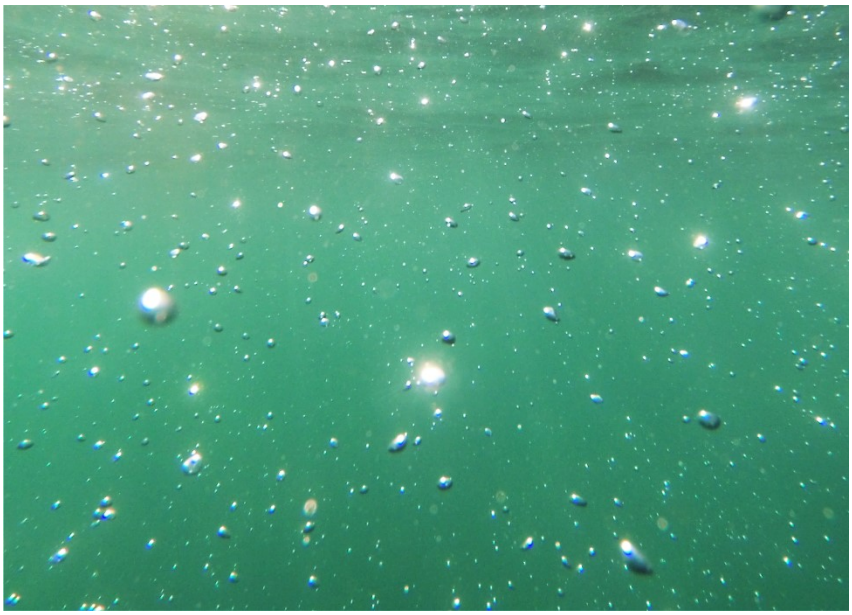

Monographische Dissertation

zur Erlangung des akademischen Grades

Doctor rerum naturalium (Dr. rer. nat.)

der Mathematisch-Naturwissenschaftlichen Fakultät

der Universität Rostock

vorgelegt von

Sebastian Friedrich Alfons Jordan

Rostock, den 11.08.2022

https://doi.org/10.18453/rosdok_id00004185

Gutachter:

Prof. Dr. Heide Schulz-Vogt, Leibniz-Institut für Ostseeforschung Warnemünde (IOW), Geomikrobiologie

Prof. Dr. Hermann W. Bange, GEOMAR Helmholtz-Zentrum für Ozeanforschung Kiel, Marine Biogeochemie

Eingereicht: 11.08.2022

Verteidigt: 18.11.2022

“One of the great dreams of humanity has been to visit other worlds. It’s starting to look as though this might be a very good idea – not just for fun and profit, but for survival.”

Terry Pratchett, Ian Stewart, Jack Cohen – The Science of Discworld

Content

I. Preface

The methods, results, discussion, and their implications described in this thesis are partially published as research articles in international scientific journals. The paragraphs from these manuscripts listed below are essentially unchanged, except for sequence or minor linguistic changes consistent with the overall concept. In particular, the appearance of figures and tables has been changed to match the overall style of this thesis.

Manuscript I, doi: 10.1038/s41598-020-61446-9

Bubble-mediated transport of benthic microorganisms into the water column: Identification of methanotrophs and implication of seepage intensity on transport efficiency

S. F. A. Jordan, T. Treude, I. Leifer, R. Janßen, J. Werner, H. Schulz-Vogt, and O. Schmale

The manuscript was published in Scientific Reports, volume 10, article number 4682 (2020).

The content and figures of this manuscript were used in chapters II, 1.1.5, 1.3, 1.3.1, 3.1.1, 3.2.1, 3.3.1, 3.3.3, 3.3.4, 3.3.5, 4.1.1, 0, 4.1.3, 4.1.4, 4.2.1, 5.1.1, 5.1.2, 5.2, 5.3.1 and their subchapters or parts of these.

Supplementary data can be accessed at:
https://www.nature.com/articles/s41598-020-61446-9

Manuscript II, doi: 10.1029/2021GL094819

Pelagic methane sink enhanced by benthic methanotrophs ejected from a gas seep

S. F. A. Jordan, U. Gräwe, T. Treude, E. M. van der Lee, J. Schneider von Deimling, G. Rehder, and O. Schmale

The manuscript was published in Geophysical Research Letters, volume 48, Issue 20, article number e2021GL094819 (2021).

The content and figures of this manuscript were used in chapters II, 1.1.2, 1.1.3, 1.1.5, 3.1.2, 3.2.2, 3.3.1, 3.3.2, 3.3.7, 3.3.8, 3.3.9, 4.3.1, 0, 4.3.3, 4.3.4, 5.3.2, 5.3.3, 5.3.4, 5.3.5, 6 and their subchapters or parts of these.

Supplementary data can be accessed at:
https://doi.io-warnemuende.de/10.12754/data-2021-0003

II. Abstract

The greenhouse gas methane is cited as a key factor in future climate change scenarios, because one of the prerequisites that would realistically enable us to achieve the 1.5-degree temperature goal by 2100 is a drastic reduction in anthropogenic methane emissions. A detailed understanding of methane sources and sinks is fundamental for these kinds of scenario models and defines the quality of the model-based forecasts. The main motivation of the present study was to obtain a better understanding of the bentho-pelagic coupling of aerobically methane-oxidizing methanotrophs and its influence on the pelagic methane sink, which is the last barrier for marine methane before it reaches the atmosphere.

One example of a bentho-pelagic exchange process, on which this thesis focuses, is the bubble-mediated transport at methane seep sites. During this exchange process, benthic methanotrophs are sorbed onto the gas-water interface of gas bubbles in the sediment and are then transported into the water column, where they are finally released. To address the complexity of the bentho-pelagic transport process and the subsequent impact of benthic methanotrophs on the pelagic methane sink, two seep sites were investigated with a combination of field campaign and modelling approaches. These two seep sites contain a variety of seep characteristics and water depths and were sampled with a bubble-catching device specifically developed for this thesis to transfer gas bubbles and associated particles into a sample cylinder. These samples were analyzed using molecular biological and biogeochemical techniques, to determine the methanotrophs' abundances, characterize their phylogeny, and define the physico-chemical environment of the water column in the surrounding of the seeps with a special emphasis on the methane concentration distribution and its microbial oxidation in the water column.

The first site investigated was the Coal Oil Point seep field, an extended seep area stretching over 3–4 km along the coast offshore of Santa Barbara (California, USA). Here, the dislocation of microorganisms from the sediment into the water column via gas bubbles released from the seabed was documented at gas-releasing vent sites. It was found that the methanotrophs transport efficiency was dependent on the volumetric gas flow, in the way that the transport rate decreased with an increasing gas flow. The bubble-mediated link between the benthic and pelagic microbial community was further supported by genetic analyses, indicating a transportation of methanotrophs of the family *Methylomonaceae* and oil degrading bacteria of the genus *Cycloclasticus* from the sediment into the water column. In addition, transported methanotrophs showed prolonged methane oxidation and growth during a three-week incubation. Based on these results, one can contend that the benthic methanotrophs are not only transported into the water column but also continue to oxidize methane.

The second part of this thesis was conducted in the North Sea at a methane point source, the well 22/4b also known as the ‘Blowout’. At this site in 1990 a drilling operation accidentally hit a shallow sedimentary gas pocket and caused a massive gas release into the water column. This catastrophic event created a 20 m deep crater, which still releases methane to date. The analysis of the upcurrent and downcurrent water masses in the vicinity of the Blowout showed an overall increase of methane concentration, methane oxidation rates and methane-oxidizing bacteria (MOB) abundances after passing the Blowout. These findings suggest the ejection of benthic MOB from the seep into the water column by two pathways: resuspension of sediments and gas-bubble-mediated transport processes. A Lagrangian particle-tracking model was applied to simulate the release of methane and MOB from the crater and the subsequent dispersion of both within the plume. According to the model, the ejection of 62 ± 40.9 L CH_4 s^{-1} and 4.29 ± 1.9 × 10^{12} MOB cells s^{-1} *in situ* from the Blowout site would produce the methane level and MOB abundance detected in the downcurrent water body. The benthic MOB inoculant substantially increased the methane oxidation capacity below the lower thermocline within the dispersing plume and thus decreased the methane turnover time by a factor of about five.

The presented work contributes significantly to the overall understanding of the bubble-mediated transport process, by defining the parameters controlling the transport efficiency and identifying the methanotrophic bacteria transported into the water column via the gas bubbles. Further, it highlights the importance of bentho-pelagic transport processes at seep sites and their positive feedback on the pelagic methane sink. Based on these results, it can be assumed that the bentho-pelagic transport processes also influence other biogeochemical cycles in seep regions.

III. Zusammenfassung

Methan ist ein klimawirksames Gas und wird in aktuellen Klima-Modellierungen als einer der Hauptakteure für das zukünftige Klimageschehen gesehen. Eine der Prämissen, die uns ermöglichen könnte die Erderwärmung auf maximal 1.5 °C bis 2100 zu begrenzen, ist eine drastische Reduktion der anthropogenen Methanemissionen. Dabei bilden genaue Kenntnisse der Methanquellen und -senken die wissenschaftliche Grundlage solcher Modelle und beeinflussen deren Präzision maßgeblich. Diese Kenntnisse sind aktuell lückenhaft. Das Ziel dieser Arbeit ist es deshalb, den bentho-pelagischen Austausch aerober methanotropher Bakterien an Gas-Seeps besser zu verstehen und dessen Einfluss auf die pelagische Methansenke zu ermitteln. Diese mikrobielle Methansenke in der Wassersäule stellt die letzte Barriere für das Methan auf dem Weg in die Atmosphäre dar.

Ein Beispiel für den Austausch zwischen Sediment und Wassersäule ist der Gasblasen-getriebene Transport von Mikroorganismen an Methan-Seeps. Zu Beginn dieses Transportprozesses werden benthische methanotrophe Mikroorganismen im Sediment an die Gas-Wasser-Grenzschicht der Gasblasen adsorbiert und folglich mit in die Wassersäule gerissen, wo sie letztendlich wieder freigesetzt werden. Um den Transport dieser methanotrophen Mikroorganismen sowie den anschließenden Verbleib und die Aktivität in der Wassersäule zu verstehen, wurden im Rahmen dieser Doktorarbeit zwei Seep-Gebiete untersucht. Ein besonderer Fokus lag hierbei auf dem Beproben der Gasblasen und daran assoziierte Partikel. Dafür wurde ein eigens für diese Studie konzipiertes Gerät verwendet, der sogenannte „Bubble Catcher“. Die auf diese Weise gewonnen Proben wurden bezüglich der Abundanz der methanotrophen Mikroorganismen sowie ihrer genetischen Zugehörigkeit analysiert. Zusätzlich wurden die physikochemischen Eigenschaften des Wasserkörpers der Seep-Gebiete mit Fokus auf der Verteilung der Methankonzentration und jeweiligen Methanoxidationsrate charakterisiert.

Bei dem ersten Seep-Gebiet handelte es sich um das Coal-Oil-Point Seep-Gebiet vor der Küste Santa Barbaras (Kalifornien, USA), welches zur Parametrisierung des Gasblasen-getriebenen Transportprozesses ausgewählt wurde. Dieses ausgedehnte Seep-Gebiet besteht aus vielen kleineren Methan-Seeps mit unterschiedlichen Gasflüssen, die sich in Küstennähe über eine Fläche von 3–4 km erstrecken. An diesen Methan-Seeps konnte der Transfer benthischer, methanotropher Bakterien vom Sediment in die Wassersäule nachgewiesen werden, wobei die Transportrate mit zunehmender Gasaustrittsstärke sank. Der Gasblasen-getriebene Austausch der benthischen und pelagischen Bakteriengemeinschaft wurde zudem durch phylogenetische Analysen gestützt. Die transportierten methanotrophen Mikroorganismen konnten der Familie der *Methylomonaceae* zugeordnet werden. Zusätzlich konnte ein Teil der transportierten Bakteriengemeinschaft dem

Genus *Cycloclasticus* zugewiesen werden. Vertreter dieses Genus sind für den Abbau von Rohöl bekannt. In weiterführenden Inkubationsexperimenten über einen Zeitraum von drei Wochen zeigten die transportierten methanotrophen Bakterien eine fortwährende Methanoxidation und Zellwachstum. Auf Grundlage dieser Ergebnisse kann man davon ausgehen, dass die methanotrophen Mikroorganismen nicht nur vom Sediment in die Wassersäule transportiert werden, sondern dort auch weiterhin Methan abbauen.

Um diesen Effekt auf die pelagische Methansenke zu quantifizieren, wurde im zweiten Seep-Gebiet eine punktförmige Methanquelle näher untersucht. Bei dieser Methanquelle handelt es sich um die ehemalige Bohrung 22/4b in der Nordsee, auch bekannt als das sogenannte „Blowout“. Im Jahre 1990 wurden hier flache Gasanreicherungen auf der Suche nach Erdöl angebohrt, wodurch es zu einer spontanen, massiven Gasfreisetzung kam. In Folge des Unfalls entstand ein 20 m tiefer Krater, aus dem fortlaufend Methanblasen austreten. Die Analyse des ein- und ausströmenden Wasserkörpers im Bereich des Blowouts zeigt einen Anstieg der Methankonzentration, der Methanoxidationsrate und der Abundanz von methanotrophen Bakterien nach dem Passieren des Methan-Seeps. Diese Ergebnisse deuten darauf hin, dass die benthischen methanotrophen Bakterien mittels Resuspension und Gasblasen-getriebenem Transports in die Wassersäule gelangen. Der Ausstoß der methanotrophen Bakterien und des Methans wurde mit Hilfe eines lagrangeschen Partikel-Modells simuliert und zeigt, wie sich die Mikroorganismen und das Methan in der Wassersäule mit der Strömung verteilen. Auf diese Weise konnte berechnet werden, dass ein Ausstoß von $4.29 \pm 1.9 \times 10^{12}$ MOB Zellen s^{-1} bzw. 62 ± 40.9 L CH_4 s^{-1} am Meeresgrund erforderlich ist, um die stromabwärts ermittelten Abundanzen der methanotrophen Bakterien und Methankonzentrationen in der Wassersäule mit dem Modell zu simulieren. Das Einbringen der benthischen Methanotrophen in die Wassersäule, auch als Inokulation bezeichnet, erhöht dabei die Methanoxidationskapazität des unteren Wasserkörpers um das Fünffache. Folglich wird dadurch die Verweilzeit des Methans in diesem Wasserkörper um denselben Faktor reduziert.

Diese Doktorarbeit erweitert das allgemeine Verständnis des Gasblasen-getrieben Transportprozesses, da die kontrollierenden Parameter definiert und die transportierten methanotrophen Bakterien identifiziert werden konnten. Zudem zeigt sie die besondere Bedeutung der bentho-pelagischen Transportprozesse für den Methanhaushalt in Seep-Gebieten sowie deren positiven Einfluss für die pelagische Methansenke auf. Basierend auf diesen Ergebnissen kann eine ähnliche Bedeutung des bentho-pelagischen Transportes für andere biogeochemische Prozesse in Seep-Gebieten vermutet werden.

1 Introduction

1.1 Methane: properties, sources, sinks, and function as greenhouse gas in a warming world

Methane, first reported in the 18th century (Priestley 1776; Volta 1777) and named by August Wilhelm von Hofmann (1866), represents the most chemically reduced form of carbon (Fig. 1). It is the most stable and simple n-alkane (dissociation energy +439 kJ mol^{-1}; Thauer and Shima 2008) as well as the most abundant organic molecule on earth (Whiticar 2020).

Methane is a potent greenhouse gas, which accumulates in the atmosphere (Fig. 1) and has a relative global warming potential of ~28 times compared to CO_2 over a 100-year lifetime (Whiticar 2020). In general, methane is generated from water-rock serpentinization (abiotic) and derived from organic matter in various ways which are categorized in biotic (e.g., plantal, microbial) and abiotic (e.g., thermogenic and pyrogenic processes) processes (Fig. 2). Measurements of the stable isotope ratios of carbon ($^{13}C/^{12}C$) and hydrogen ($^{2}H/^{1}H$) – expressed in permille (‰) for $\delta^{13}C$ relative to the Vienna Pee Dee Belemnite (VPDB) and $\delta^{2}H$ relative to the Vienna Standard Mean Ocean Water (VSMW) are used to differentiate between biogenic ($\delta^{13}C$: −110 to −45‰; $\delta^{2}H$: −450‰ to −125‰), thermogenic ($\delta^{13}C$: −45 to −15‰; $\delta^{2}H$: −350‰ to −100‰) and pyrogenic ($\delta^{13}C$: −30 to −12.5‰; $\delta^{2}H$: −232‰ to −195‰) sources (Whiticar 1999; Bakkaloglu et al. 2022). This is possible as biochemical reactions discriminate against $\delta^{13}C$ based on the kinetic isotope effect (Whiticar 1999). Thus, methanogenesis, as the final step of the microbial organic matter degradation, produces methane that is enriched in ^{12}C, whereas thermogenic and pyrogenic processes produce isotopically heavier methane (Whiticar 2020). Anthropogenic emission, however, is based on biogenic processes (e.g., ruminants, landfills), pyrogenic processes (e.g., biomass burning) and thermogenic processes (e.g., fossil fuel industry, Schwietzke et al. 2016).

1.1.1 Atmospheric concentration: terrestrial and anthropogenic sources and sinks

Much of the current research on methane concerns its sources, sinks and impact on the climate, with a focus on its effect on the atmosphere (Saunois et al. 2020). Methane is the second most important anthropogenic greenhouse gas, after carbon dioxide, with a residence time of ~9–11 years and a radiative forcing of ~3.63×10^{-4} W m^{-2} ppb^{-1} (Myhre et al. 2014; Whiticar 2020). The monthly atmospheric mean concentration for methane stagnated between 1999 and 2006 (Nisbet et al. 2014) and reached 1909.2 ppb in March of 2022 (Fig. 2; Ed Dlugokencky, NOAA/GML; www.esrl.noaa.gov/gmd/ccgg/trends_ch4/; last accessed 02.08.2022), which is a ~262% increase over the pre-industrial levels (722 ppb in 1750; WMO

2017). Although several theories have been suggested, e.g., a shift in emissions with a decrease in natural emissions compensating for an increase in anthropogenic emissions (Saunois et al. 2017) or changes in the hydroxyl radical (•OH) concentrations (Schaefer et al. 2016), there is no consensus on the cause of the hiatus (e.g., Bousquet et al. 2006; Kai et al. 2011; Saunois et al. 2020).

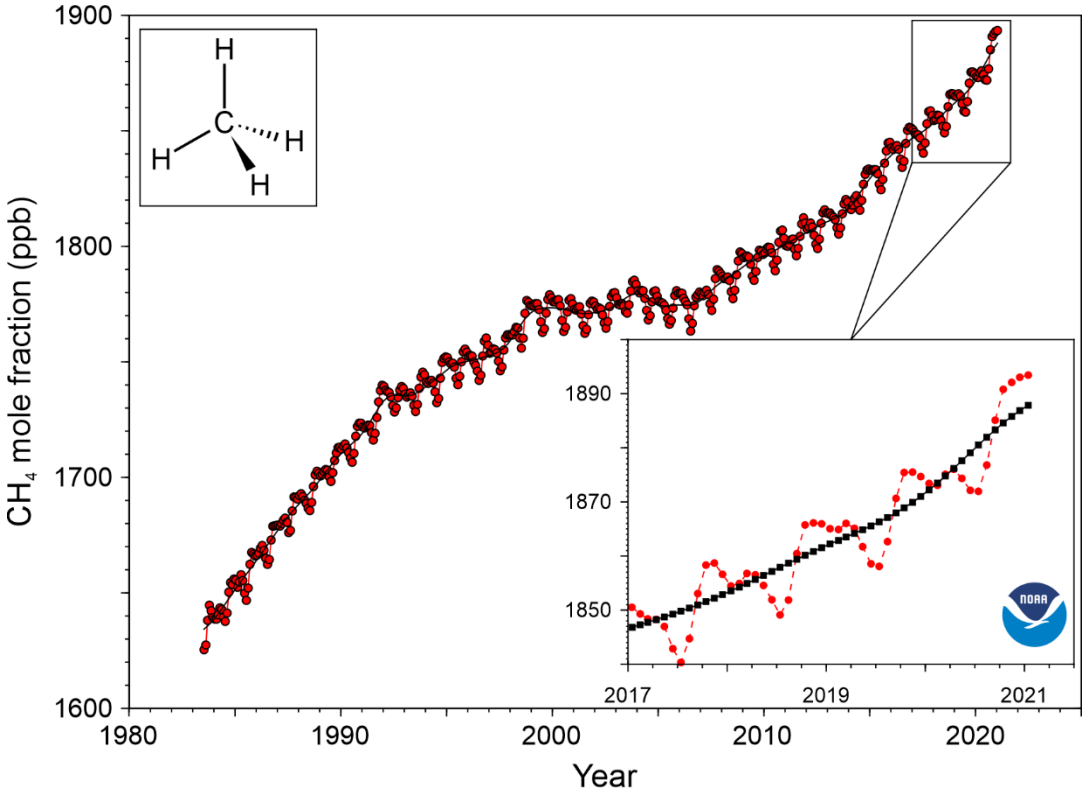

Fig. 1 | Time series of NOAA/ESRL atmospheric methane abundance. Monthly averaged mixing ratios (red circles) from marine surface sites reported as dry mole fraction. The global 12-month running mean (black squares) starting from 1983 up to present. The lower inlet shows the period from 2017-2021 in more detail to reveal the interannual course pattern. The upper inlet depicts the chemical structure of a methane molecule displayed in the Natta projection. Adapted from Dlugokencky, NOAA/GML (www.esrl.noaa.gov/gmd/ccgg/trends_ch4/; last accessed 02.08.2022).

Impactful anthropogenic sources are (1) agriculture (e.g., wetland rice cultivation, livestock), (2) decomposition of municipal solid wastes and the (3) production and distribution of fossil fuels (gas, coal, oil) due to leakage and incomplete combustion (EPA 2016). However, several anthropogenic sources lack sufficient observations (Saunois et al. 2016). A bottom-up approach estimated a yearly anthropogenic emission of ~369 Tg CH_4 or 50–65% of the global methane emission (~703 Tg CH_4 yr^{-1}) for the decade 2000–2009 (Fig. 2; Saunois et al. 2020). However, the estimates for natural and anthropogenic methane emissions and sinks (Fig. 2) have changed over the past decades in magnitude and temporal variation (annual to inter-

annual) and, despite ongoing research, are still characterized by large uncertainties (Saunois et al. 2020 and references therein). To be more specific, the decadal methane budget suggested relative uncertainties of 20–30% for inventories of anthropogenic emissions in specific sectors (e.g., agriculture, waste, fossil fuels), 50% for biomass burning and natural wetland emissions, and reaching 100% or more for other natural sources (e.g., inland waters, geological sources; Saunois et al. 2020). On the contrary, the sinks add up to a total of ~625 Tg CH_4 yr^{-1}, with the main sinks for methane in the atmosphere being its abiotic reaction with hydroxyl radicals (~90%; Ehhalt 1974), microbial oxidation in terrestrial soils (Dutaur and Verchot 2007) and photochemical reactions (Saunois et al. 2020).

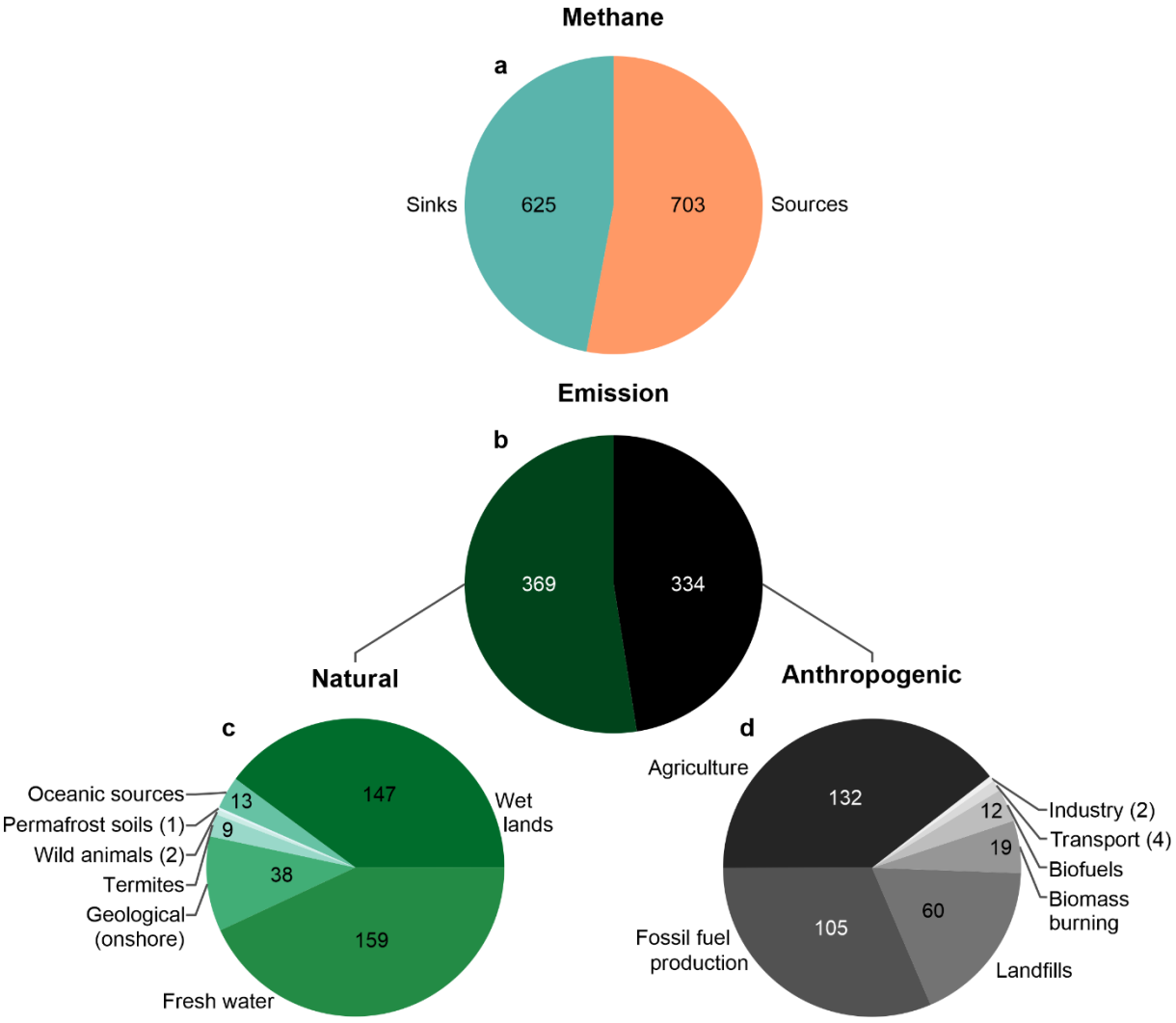

Fig. 2 | Proportional methane sources and sinks. a, The global methane sources and sinks imbalance, **b**, Methane emission, **c**, natural methane sources, and **d**, anthropogenic methane sources and the respective estimates in Tg CH_4 yr^{-1}. Data derived from Saunois et al. (2020) and references therein.

1.1.2 Marine methane sources

Methane is introduced into the water column by a variety of sources, with sediment being the most pronounced (Whiticar 2020). Other sources include methane production in the water column and, in case of an undersaturated mixed layer, the atmosphere (Reeburgh 2007). In the sediment, methane is generated by a variety of processes with the majority being microbially-mediated diagenesis of organic matter and abiotically through the serpentinization reaction, a water-rock reaction occurring in hydrothermal systems (Reeburgh 2007). Other sources include leaking petroleum deposits and decomposing methane clathrate hydrates (Reeburgh 2007).

Most biogenic methane is formed in anoxic sediments by anaerobic archaea (Fig. 3). The classical methanogens belong exclusively to the phylum Euryarchaeota (Kharitonov et al. 2021). However, recently genes that encode the methyl-reducing key enzyme of methanogenesis were found in the genomes of the candidate phyla "*Candidatus* Verstraetearchaeota" and "*Candidatus* Bathyarchaeota" (Kharitonov et al. 2021 and references therein). So far, four methanogenic pathways are known: acetoclastic, hydrogenotrophic, methyl-reducing, and methylotrophic methanogenesis (e.g., Nazaries et al. 2013; Kallistova et al. 2017).

The produced methane (thermogenic and biogenic) accumulates over time and can be stored in gas hydrates, gas reservoirs, and pore water. Gas hydrates are only stable over a range of low-temperature and intermediate pressure, which can be found in marine sediments at a water depth of more than 300 m (Ruppel and Kessler 2017). Recent studies estimated that in methane hydrates alone ~5–36 × 10^5 Tg CH_4 is stored (e.g., Wallmann et al. 2012; Whiticar 2020). To put this in perspective, natural gas reserves (recoverable) are known to store ~4.4 × 10^6 Tg CH_4 (~6.6× 10^{15} m^3; e.g., BP, https://www.bp.com/en/global/corporate/energy-economics/statistical-review-of-world-energy.html; last accessed: 02.08.2022). Gas from deep reservoirs (e.g., Leifer and Culling 2010) or shallow gas pockets (e.g., Silyakova et al. 2020) migrates upward along focused pathways, often created through faults (Judd 2003), fractures (Hunt 1995; Whelan et al. 2005; Leifer et al. 2010), and hydrocarbon wells (Vielstädte et al. 2017), and might form cold seeps when reaching the sediment surface.

The subsequent transportation of sedimentary methane to the sea surface takes place in two different ways: (i) advective and diffusive fluxes of dissolved methane that reach the surface water on relatively long time scales (Matveeva et al. 2015) and (ii) gas bubble ebullition that allows a more rapid and efficient methane transport (Leifer and Patro 2002). However, direct transport of methane into the atmosphere by gas bubbles is likely only in shallow seep regions, because after their liberation from the seafloor, the ascending bubbles release most of their methane (75%–100%) within the first 100 m (McGinnis et al. 2006). This dissolution of methane

into the surrounding water is thought to occur even faster in intense seeps (Leifer et al. 2015). The continuous transfer of methane from uprising bubbles into the surrounding water creates methane-laden water masses in the form of dissolved methane plumes, which are transported away from the methane source with the currents (Schmale et al. 2012b; Steinle et al. 2015). If the water column is highly stratified (McGinnis et al. 2006; Schmale et al. 2010; Nauw et al. 2015b), these methane plumes persist for an extended time and distance in deep water before the methane is microbially oxidized (Rehder et al. 1999; Ruppel and Kessler 2017), transported to the sea surface by mixing (Nauw et al. 2015a) or upwelling (Wäge et al. 2019; Jacobs et al. 2021), and the rest are finally vented into the atmosphere. In general, a mixed layer with a methane concentration higher than the atmospheric equilibrium (~2 nmol L^{-1}) indicates a flux of dissolved methane into the atmosphere. However, most of the formed methane (~26 Tg CH_4 yr^{-1}; Boetius and Wenzhöfer 2013) is oxidized (s. section 1.1.3) before the rest escapes into the hydrosphere, contributing to the ~43 Tg of CH_4 dissolved in the oceans (Reeburgh 2007; Valentine 2011). Marine emissions (6–12 Tg CH_4 yr^{-1}; Weber et al. 2019) contribute <1% to the total annual methane emission into the atmosphere (~576 Tg CH_4 yr^{-1}; Saunois et al. 2016), with shelf seas accounting for the largest share (Weber et al. 2019). These shallow near-shore environments dominate the global oceanic flux because the biological methane filters of the water column can be bypassed due to limited water depth and thorough mixing (Shakhova et al. 2014; Lohrberg et al. 2020).

Recent studies of methane dynamics in surface waters have concluded that anaerobically produced methane from benthic sources could not sustain the observed pelagic methane enrichments in surface waters (Lenhart et al. 2016). However, such oversaturation occurs frequently and regionally in parts of the ocean and is also known as the “methane paradox” (Grossart et al. 2011; Repeta et al. 2016; Schmale et al. 2018). Several processes are posited as producing methane in the aerobic water column and contribute to the shallow methane maximum. The metabolization of methionine by algae (Lenhart et al. 2016) as well as transfer of hydrogen from algae to attached methanogens (Grossart et al. 2011) have been shown in recent studies to produce methane. Other processes involve the microbial degradation of phosphonic acids (e.g., methylphosphonate; Repeta et al. 2016), dimethylsulfide (DMS), dimethylsulfoniopropionate (DMSP) and dimethylsulfoxide (DMSO; Damm et al. 2010; Zindler et al. 2013) as well as the archaeal methanogenesis in anoxic micro niches e.g., copepods’ guts and fecal pellets (Holmes et al. 2000; Wäge et al. 2019, 2020; Stawiarski et al. 2019). Photomethanification from colored dissolved organic matter (Zhang and Xie 2015) has recently been discussed as an abiotic process. Although the sources and sinks of methane on earth have been both well researched, there is still much to be understood and to better assess the methane budget in the marine environment and its connection to the atmosphere.

1.1.3 Marine methane sink: the benthic and pelagic methane filter

During its ascent through the sediment (Fig. 3), methane is anaerobically oxidized by a consortium of sulfate reducers and archaea (Knittel and Boetius 2009). The classic anaerobic oxidation of methane (AOM-SR, Eq. 1) mostly occurs in the sulfate-methane transition zone (SMTZ) of anoxic marine sediments and is estimated to oxidize the majority (~90%) of the formed methane (Knittel and Boetius 2009).

$$CH_4 + SO_4^{2-} \rightarrow HCO_3^- + HS^- + H_2O \quad (1)$$

The significant increase of inorganic carbon and alkalinity leads to the massive precipitation of calcium carbonate following the net equation (Eq. 2; Aloisi et al. 2002; Knittel and Boetius 2009).

$$CH_4 + SO_4^{2-} + Ca^{2+} \rightarrow CaCO_3 + H_2S + H_2O \quad (2)$$

The precipitated carbonates often serve as a basis for sessile fauna, e.g., algae and sponges, which are important parts of the ecosystems. The classical AOM-SR is a syntrophic process mediated by anaerobic methanotrophic archaea (ANME) and sulfate reducing bacteria (SRB; Boetius et al. 2000). However, recent studies indicate that anaerobic methane consumption is not uniquely coupled to sulfate reduction while other terminal electron acceptors or direct interspecies electron transfer are discussed (e.g., Regnier et al. 2011; Milucka et al. 2012; Treude et al. 2014; Lovley 2017; Wang et al. 2017). The methane that reaches the upper, oxic sediment layer is partially aerobically oxidized by methanotrophic bacteria (see section 1.2) before it escapes into the overlaying water column. The net reaction is depicted in Eq. 3.

$$CH_4 + 2O_2 \rightarrow CO_2 + 2H_2O \quad (3)$$

While the dissolved methane fraction is accessible for methanotrophs, the gaseous fraction can bypass the pelagic methane oxidation. Several factors are controlling the dissolved methane fraction, which in total are also known as the pelagic methane filter. Known important factors controlling the pelagic methane oxidation are methane concentration (Crespo-Medina et al. 2014), a change in water masses (Steinle et al. 2015), oxygen concentration (Steinle et al. 2017), trace metals (Semrau et al. 2018) and light (Dumestre et al. 1999; Oswald et al. 2015; Savvichev et al. 2019). Moreover, the impact of transported benthic methanotrophs onto the pelagic methane turnover was posited by Schmale et al. (2015) but remained unconstrained.

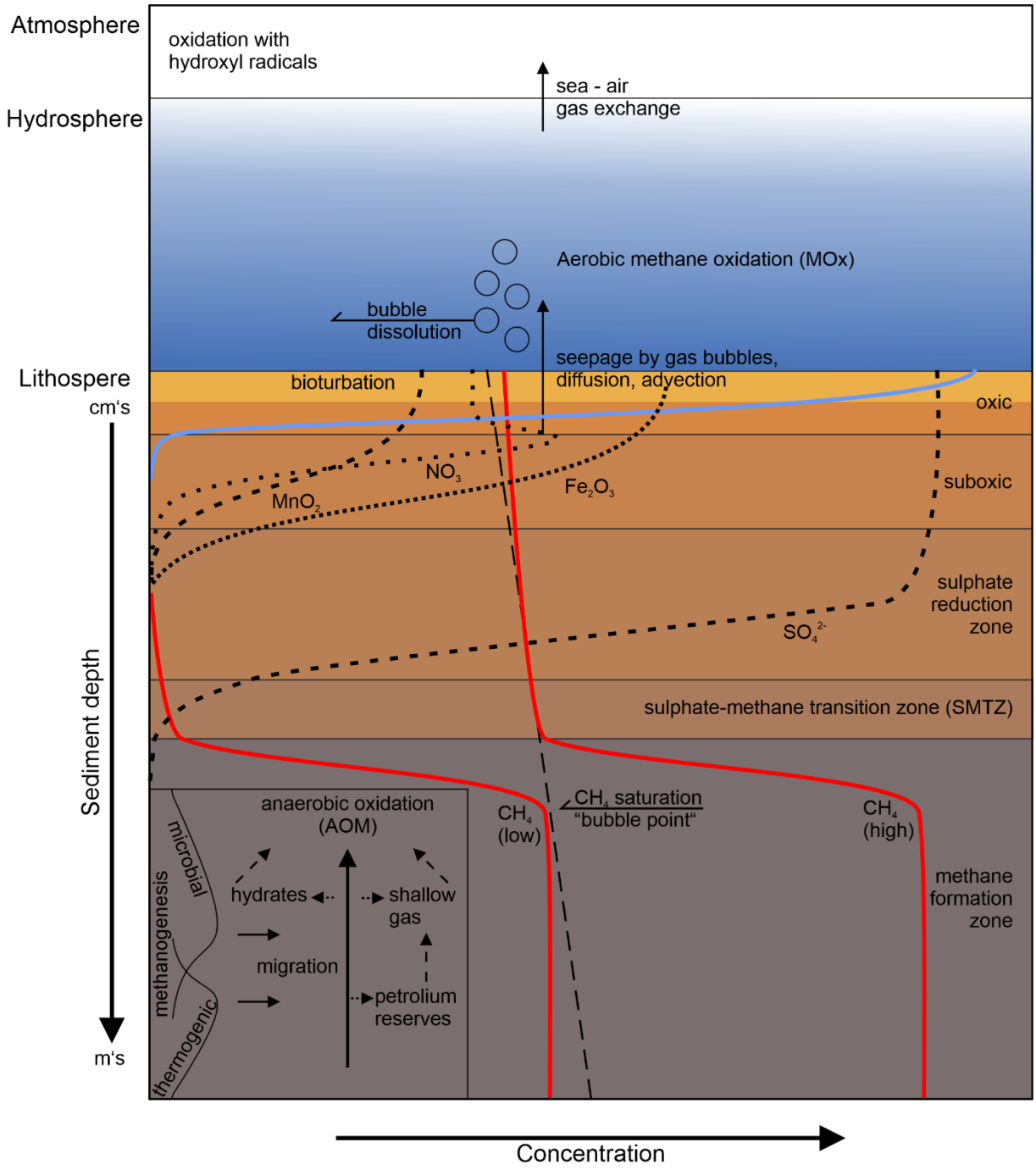

Fig. 3 | Sedimentary methane distribution. Schematic zonation in marine sediments with the focus on methane depth distribution. The inlet depicts schematically the sources, storage and transport of methane in marine sediments. Adapted from Whiticar (2020) and Judd (2004).

1.1.4 Submarine methane seep environments

Most deep-sea ecosystems are known to be energy limited. Local food webs depend on the supply of marine snow (Suess 1980), whereas energy sources like whale falls (Smith et al. 2015) and hydrocarbon seeps (Suess 2014) form oasis-like ecosystems. The latter are fueled by chemical energy transported by fluids and gas bubbles (Niemann et al. 2013). This energy

is harvested by chemoautotrophs and subsequently is made available for organisms of higher trophic levels (Niemann et al. 2013; Leifer 2017). Specifically, methane-rich hydrothermal fluids escape through hydrothermal vents, black smokers, and hydrothermal sediments (Teske et al. 2002). They are predominantly fueled by serpentinization (Kelley et al. 2005; Keir et al. 2006) or, in the case of hydrothermal sediments, by pyrolysis of complex organic matter (Teske et al. 2002). Diffusive systems, on the contrary, slowly transport the produced methane (mostly from methanogenesis) towards the sediment surface, so that most of the methane is consumed by AOM before it reaches the sediment surface (Treude et al. 2005).

However, if the methane concentration in the sediment exceeds methane solubility, gas bubbles (in the following called bubbles) are formed and rise towards the sea surface (Judd et al. 1997; Leifer and Patro 2002). These methane bubbles occur individually, as streams or flares, plumes, and intense mega seep bubble plumes with emissions ranging from a few liters to 10^6 liters per day (Leifer 2019). These seeps can manifest in different geologic settings as the gas originates from a variety of sources such as gassy sediments, shallow gas accumulations, deep gas reservoirs, or gas hydrates and submerged permafrost (Leifer et al. 2010; Schneider von Deimling et al. 2015; Ruppel and Kessler 2017; Shakhova et al. 2019; Lohrberg et al. 2020). As geological settings and sources differ, gas seepage occurs at all water depths ranging from the hadal zone (e.g., Japan Trench, 7,434 m; Watanabe et al. 2010) to shallow waters (Coal Oil Point seep field, ~15 m; Jordan et al. 2020 and Leifer 2019), and can even be found in the intertidal zone (Jessen et al. 2011). Bacterial mats are typically present at most sites and are an indication of seep activity (Niemann et al. 2013). The organisms, which to a major part form these mats (Treude et al. 2007 and references therein), perform anaerobic or aerobic oxidation of methane. In the case of anaerobic oxidation, huge carbonate structures can be formed. At persistent seep sites with sufficient methane flux, higher biota such as crabs, mussels, snails, and tubeworms, fed by symbiotic chemotrophs, as well as their predators, can be found (Fig. 4c, d, e). These symbiotic chemotrophs can be located endobiotically, e.g., in gills or special organelles (e.g., trophosome) in their host organisms (Dubilier et al. 2008; Petersen and Dubilier 2009) or epibiotically on the host (Goffredi et al. 2020).

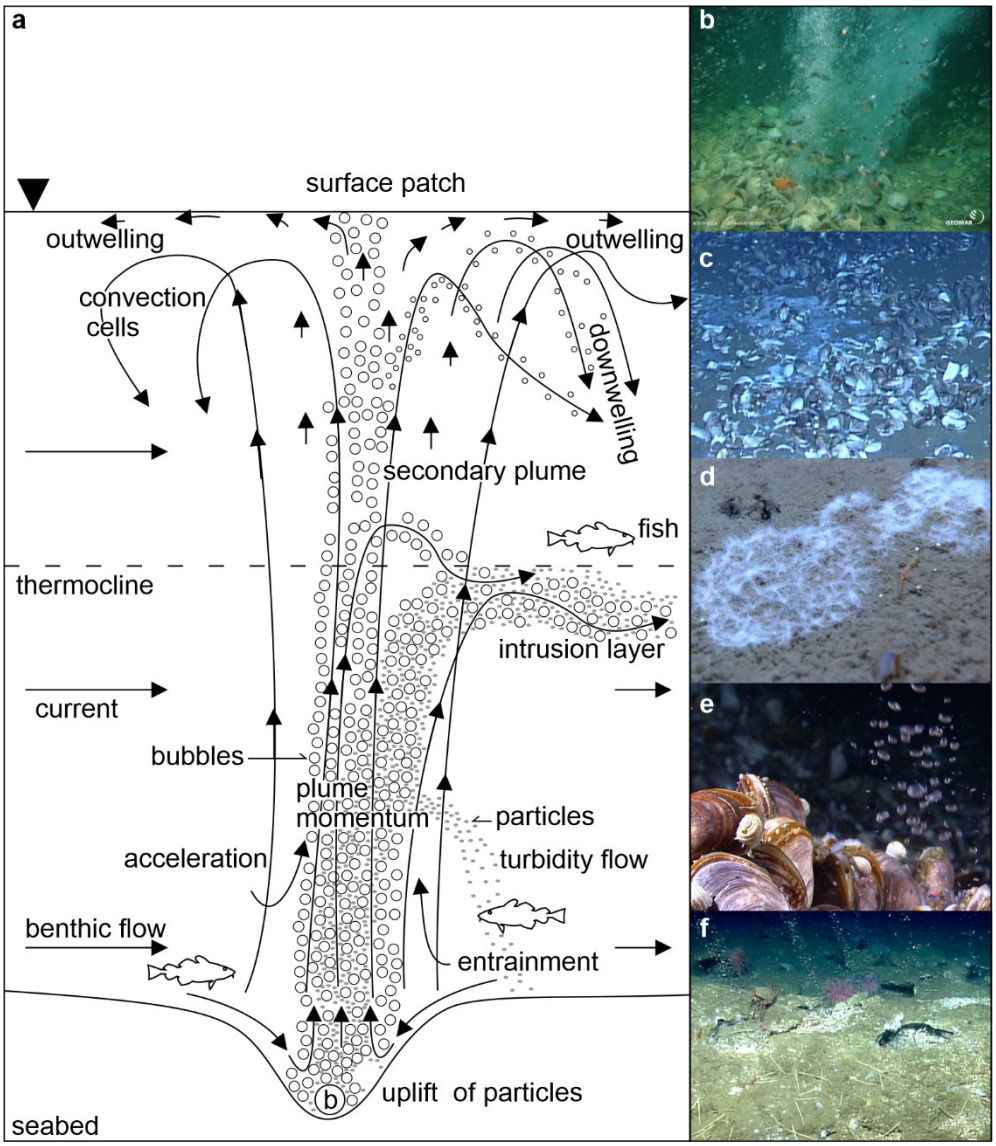

Fig. 4 | Schematic bubble plume mechanics and seep environment based on the North Sea Blowout. a, Arrows depict the water movements at a mega seep as well as the detrainment of parts of the plume, which form an intrusion layer, adapted from Schneider von Deimling et al. (2015) and Wilson et al. (2015). **b**, The image shows a major seep in the center of the Blowout. **c, e**, f, Depict communities of mussels or worms in the Gulf of Mexico which host chemosynthetic symbiotic bacteria for energy sustenance. **d**, Shows bacterial mats typical for cold seeps. Underwater picture (b) was taken by ROV PHOCA (Copyright: ROV PHOCA Team / GEOMAR, Kiel), images (c-f) are courtesy of the NOAA Ocean Exploration and Research Program.

1.1.5 Bubble formation, migration, and dissolution

For continuous seepage, gas accumulation in a reservoir is necessary, e.g., below a capping layer (Leifer 2019). Subsequently, the methane gas migrates from such reservoirs through fractures, faults, and porous layers towards the seafloor following the lowest resistance (Leifer et al. 2010). This flow resistance depends on several physical parameters in the sedimentary layers such as, grain size, porosity, and occurrence of fractures (Leifer and Boles 2005).

Additionally, seepage is controlled by the overlaying hydrostatic pressure and thus by tides (Leifer and Wilson 2007) and storms (Lohrberg et al. 2020). Leifer and Boles (2005) described the relationship between tides and seepage in a conceptual model using an electrical network as analogue (Fig. 5). The driving force is the reservoir pressure (voltage), which has to create an overpressure (driving voltage) across fractures (resistance) and hydrostatic pressure in order to lead to seepage (Leifer and Wilson 2007). The gas flow (electrical current) passes through the fractures, which are characterized by their specific resistance and volume (capacitance). Hence, the pathway from the reservoir to the seafloor can be described as a network of resistors and capacitors. Applying the model to a two-pathway system: different resistances for each pathway results in different seepage intensities. In unconsolidated sediment another pathway can form if the resistance becomes too high (Leifer and Wilson 2007). Thus, seep sites often consist of several vents, sometimes with several meters in-between, which are fueled by a single source (Leifer and Boles 2005).

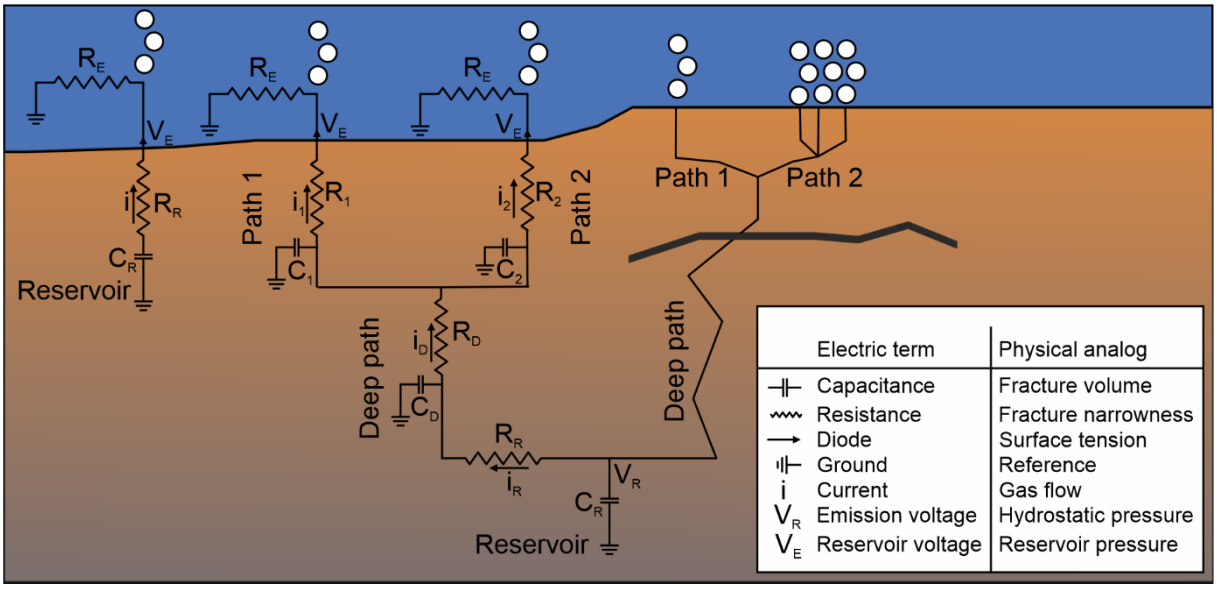

Fig. 5 | Electric model for bubble seepage in a simplified seep area. Adapted from Leifer and Wilson (2007)

The released bubble size is controlled by the nature of the seabed sediment, with the vent-orifice-diameter as primary control (Leifer and Boles 2005; Judd and Hovland 2007). Additional factors are horizontal water velocity, surfactant contamination, and gas flux (Leifer and Boles 2005). Upon release from a single vent the bubbles rise towards the sea surface as a bubble chain (Schneider von Deimling et al. 2010), whereas stronger seepage results in a bubble flare of a width of 10 m or more (Fig. 6). Such bubble flares can rise over 1300 m in the water column before the bubbles disappear through their dissolution (Greinert et al. 2006).

Once in the water column, the bubbles' gas composition starts to change as the gas-transfer with the surrounding water begins immediately following their concentration gradient in and out of the bubble (Leifer and Patro 2002). In addition gas outflow is controlled by surface area, internal gas circulation, rise velocity, surfactants (e.g., oil, particles, bacteria; Leifer and Patro 2002; McGinnis et al. 2006), and hydrate rim formation (Rehder et al. 2002). The latter only occurs below and within the hydrate stability zone (HSZ, ~400–800 m). Depending on the initial bubble size, modelled bubble behavior showed that significant methane transfer to the atmosphere is only likely from seep sites shallower than 100 m (McGinnis et al. 2006). Small bubbles (diameter 5.5 mm, 100% methane) released at 90 m water depth were depleted in methane after rising ~70 m, although they still reached the water surface with a diameter of ~1 mm (McGinnis et al. 2006). Typical seep bubbles on the seabed consist of methane (~90%), carbon dioxide and larger n-alkenes (e.g., Blowout, Schneider von Deimling et al. 2015) which diffuse out of the bubble. When such bubbles reach the sea surface they mainly consists of oxygen and nitrogen, which have been taken up from the surrounding water masses during the bubbles' ascent (Leifer and Patro 2002). This results in a dissolved methane plume, which is transported in the downcurrent direction from the seep area. In addition to the water depth (Leifer and Patro 2002; McGinnis et al. 2006) several other processes determine the amount of methane that reaches the sea surface, such as ocean currents and mixing (Steinle et al. 2015), water-column stratification (Schneider von Deimling et al. 2011; Schmale et al. 2012a; Nauw et al. 2015a; Steinle et al. 2016), and microbial methane oxidation (Reeburgh 2007; Valentine 2011).

Large or strong bubble seepage creates rising bubble plumes, influencing the surrounding water column with a variety of plume mechanics (Fig. 4a). Such bubble plumes transport methane-laden water masses, which reduce the methane outflow from the uprising bubbles (Leifer 2010). This large number of rising bubbles creates an upwelling flow of bottom water, which subsequently results in higher bubble rise velocities (Leifer and Patro 2002) and an uplift of sediment particles (Leifer et al. 2009; Schneider von Deimling et al. 2015). The upwelled water creates outwelling when it reaches the surface followed by a density-driven downwelling, which can still carry small bubbles. This then creates convection cells (Schneider von Deimling et al. 2015). If the vertical momentum no longer is sufficient to lift the denser water, the plume will detrain and form an intrusion layer in the downcurrent direction dragging smaller bubbles and particles along (Schneider von Deimling et al. 2015).

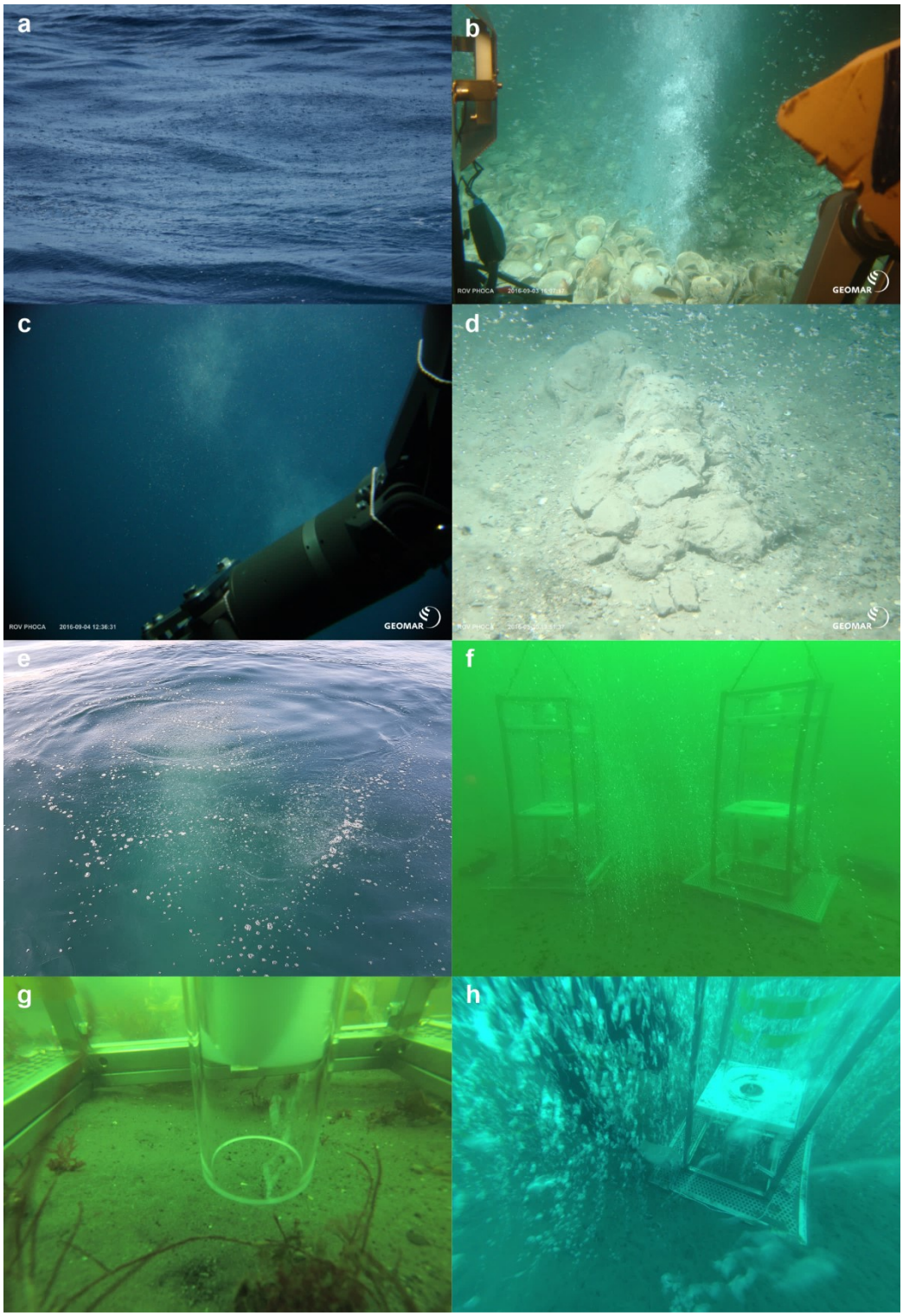

Fig. 6 | Photo documentation of the Blowout crater and Coal Oil Point seep field and surroundings. Pictures **a**-**d** were taken at the North Sea Blowout location: **a**, Bubble surface patch over the Blowout crater, **b**, mega vent in the center of the crater, **c**, distinct bubble plume in the water column with a diameter of 10 m or more, **d**, pile of most likely clay and minor vents in the crater. The Pictures **e**-**h** were taken at the Coal Oil Point seep field: **e**, surface patch of the IV Super Seep (IVSS), **f**, **h** Bubble Catcher experiments at the IVSS, **g**, close up during the bubble catching process. **a**, **e**, Surface patches were taken by Sebastian Jordan; **b**, **c**, **d** underwater pictures were taken by ROV PHOCA (Copyright: ROV PHOCA Team / GEOMAR, Kiel). Adapted from Jordan et al. (2021).

1.2 Methanotrophic bacteria

Methanotrophy was first reported at the beginning of the 20th century (Kaserer 1905; Söhngen 1906). The oxic methanotrophy is executed by methane-oxidizing bacteria (MOB). They are typically present at oxic/anoxic interfaces as well as in high methane environments, where both oxygen and methane are available, e.g., the oxic parts of the sediment and water column above methane seeps. Over the years industrial interests in methanotrophs grew as the methanotrophic enzyme can be used to produce biofuels and chemicals such as polyhydroxybutyrate (PHB), which can be used as a bio-degradable plastic (Strong et al. 2016). The identification and classification of methanotrophic organisms has rapidly increased in the last two decades with the advancement of molecular methods and broad accessibility of sequencing techniques (Knief 2015). However, the taxonomic status of some genera (e.g., *Candidatus* Crenothrix polyspora, Stoecker et al. 2006) and organisms is unclear as only ~1% of all microorganisms is cultivable so far (Vartoukian et al. 2010). Currently, three MOB subtypes are known and are differentiated by their genetic clustering and key enzymes for methane oxidation (Table 1): (1) *Gammaproteobacteria* (type I), (2) *Alphaproteobacteria* (type II), and (3) *Verrucomicrobia* (type III).

Table 1 | Phylogeny and type of aerobic methanotrophic families.

Phylum and class	Family	Type
Gammaproteobacteria	Methylococcaceae	Ia/Ib
	Methylothermaceae	Ic
Alphaproteobacteria	Methylocystaceae	IIa
	Bijerinckiaceae	IIb
Verrucomicrobia	Methylacidiphilaceae	III

Phylogenetically, the methanotrophic *Gammaproteobacteria* belong to the families *Methylococcaceae* and *Methylothermonaceae* (Hirayama et al. 2014), which do not contain any non-methanotrophic bacteria (Knief 2015). On the contrary, the two families *Methylocystaceae* and *Beijerinckiaceae*, which include additional non-methanotrophic genera, constitute the methanotrophs belonging to the *Alphaproteobacteria*, (Knief 2015). The recently described phylum *Verrucomicrobia* includes only a few methanotrophic species so far, which are mostly thermo- and acidophilic (e.g., Dunfield et al. 2007; van Teeseling et al. 2014). In general, methanotrophs cover a broad range of ecological niches, while habitat adaptation and specialization seem to occur at different taxonomic levels (Knief 2015). For a long time the features used to distinguish between type I and II methanotrophs were: the carbon fixation

mechanism (type I: ribulose monophosphate pathway; type II: serine cycle), position of internal membranes (type I: vesicular discs; type II: paired membranes aligned to the cell periphery; Fig. 7), predominance of specific fatty acids (type I: C_{16}; type II: C_{18}), capability of nitrogen fixation, and formation of resting stages (Knief 2015). However, in recent years only the major carbon fixation pathway has remained as a distinctive trait, most other characteristics are no longer considered exclusive to one type (Knief 2015, and references therein). In 2009 it was proposed to abandon the categorization (Op den Camp et al. 2009). However, the terms are still broadly used and were adapted towards synonyms for the phylogenetic groups (Knief 2015) as described above.

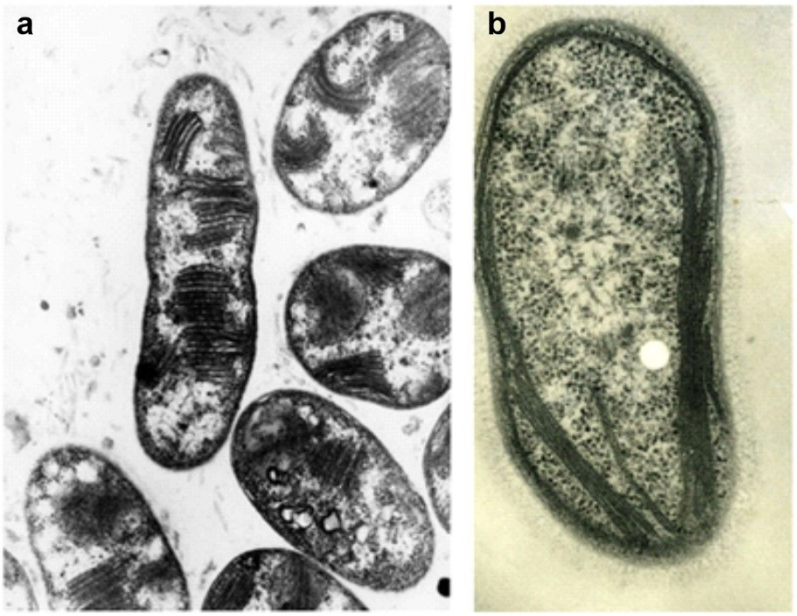

Fig. 7 | Microscopic images of type I and II methanotrophic bacteria. Electron micrograph of a cross-section of **a**, typical Type I methanotroph *Methylomonas methanica* and **b**, Type II methanotroph *Methylosinus trichosporium*. Cells were magnified 65,000 (a) and 75,000 (b) times. Adapted from Kalyuzhnaya et al. (2019), reproduced with permission from Springer Nature, photograph courtesy of H. Dalton.

Cultivation-independent detection of methylotrophs was first established in 1990 (Tsien et al. 1990) followed by the detection of marine methanotrophs in 1995 (Holmes et al. 1995b) with the use of gene probes. Nowadays, MOB are usually quantified using fluorescent probes and polymerase chain reaction techniques (e.g., RT-PCR) and identified using next generation sequencing (NGS). In general, the most frequently used gene for identification of bacteria is the 16S rRNA gene, and there are several specific primers available for different methanotrophic groups (McDonald et al. 2008) that provide information about the phylogenetic placement of MOB in environmental samples. However, this gene is only suited for well-known families whereas functional genes can be used for to detect unknown methanotrophs. In the

case of aerobic methanotrophs, the gene encoding for the key enzyme methane monooxygenase (MMO) is a suitable candidate for phylogenetic analysis, as all known methanotrophic bacteria contain the enzyme (Kalyuzhnaya et al. 2019). It is widely used and the generated phylogenies (Tavormina et al. 2008; Steinle et al. 2015) are largely congruent with those of the 16S rRNA gene (e.g., Auman and Lidstrom 2002; Heyer et al. 2002). Two forms of this enzyme are known: the copper-dependent, membrane-associated particulate methane monooxygenase (pMMO) and the soluble methane monooxygenase (sMMO). Both oxidize methane to methanol, which is then further oxidized. The general pathway of methane oxidation is shown in Fig. 8. In particular, the gene encoding for the α-subunit (pmo*A*) of the pMMO is most frequently used as marker, since it is present in most MOB. An exception are some species of the *Beijerinckiaceae* family, which can be included using the *mmoX* gene encoding the α-subunit of the sMMO hydroxylase component (Deng et al. 2013) in addition to *pmoA* (Knief 2015). However, *mmoX* is not uniformly present or absent in genera and even at species level resulting in incomplete detection of this family (Heyer et al. 2002). In recent years, updated phylogenetic trees, paralogous gene copies and the detection of related monooxygenases in non-methanotrophic bacteria indicate that conclusions about the taxonomic identity of bacteria based on the *pmoA* sequences should be taken cautiously if the sequences cluster far from established MOB (Knief 2015).

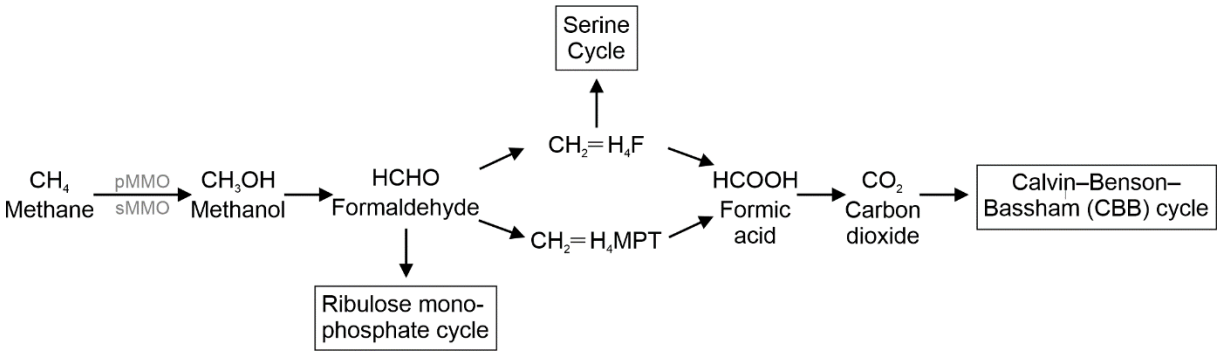

Fig. 8 | Generalized pathway of aerobic methane oxidation by methane-oxidizing bacteria. 5,10-Methylenetetrahydrofolate (CH_2=H_4F) and 5,10-Methylenetetrahydromethanopterin (CH_2=H_4MPT) are shortened as commonly used in the literature. Adapted from Semrau et al. (2018), who provide an in-depth look into the enzymes involved in the aerobic methane oxidation.

1.3 Bentho-pelagic transport processes

The exchange of nutrients and organic matter between benthic and pelagic compartments affects the composition of the respective microbial communities and thus their functional capabilities in shelf seas. Microorganisms transport to and from the sediment and water column has also been described and occurs by a variety of exchange processes (Fig. 9). For example, the suspension of benthic bacteria from beach material within the splash zone can facilitate cell transport into coastal water (over-beach transport; Shibata et al. 2004; Yamahara et al. 2007). In addition, bacteria located at shallow sediment depths can be mobilized by infiltrating seawater and then carried to deeper sediment strata, from where they can be injected into the water column by submarine groundwater discharge (through-beach transport; Russell et al. 2012). Another bentho-pelagic transport mechanism in shallow waters is sediment resuspension triggered by wind-induced mixing, breaking waves, tides, bioturbation, and gas bubble transport (Orvain et al. 2003; Ferguson et al. 2005). Microorganisms in the sediments usually are associated with fine particles (<60 µm; Jamieson et al. 2005) at concentrations that exceeds those in the water column by up to four orders of magnitude (Schmale et al. 2015). Resuspension by tidal currents can increase bacteria concentrations especially within the benthic boundary layer, that is thought to be characterized by a distinct microbial community with high activity (Stevens et al. 2005; Ziervogel and Arnosti 2009; Bertagnolli et al. 2011). Together, these exchanges and transport mechanisms may influence the coastal planktonic microbial food web (Shimeta et al. 2002; Garstecki et al. 2002; Guizien et al. 2014) and alter biogeochemical cycles (Shimeta et al. 2002; Forehead et al. 2013). However, for a comprehensive understanding of the extent of these transport mechanisms, controls, and impact on the pelagic biogeochemical processes further investigation is needed.

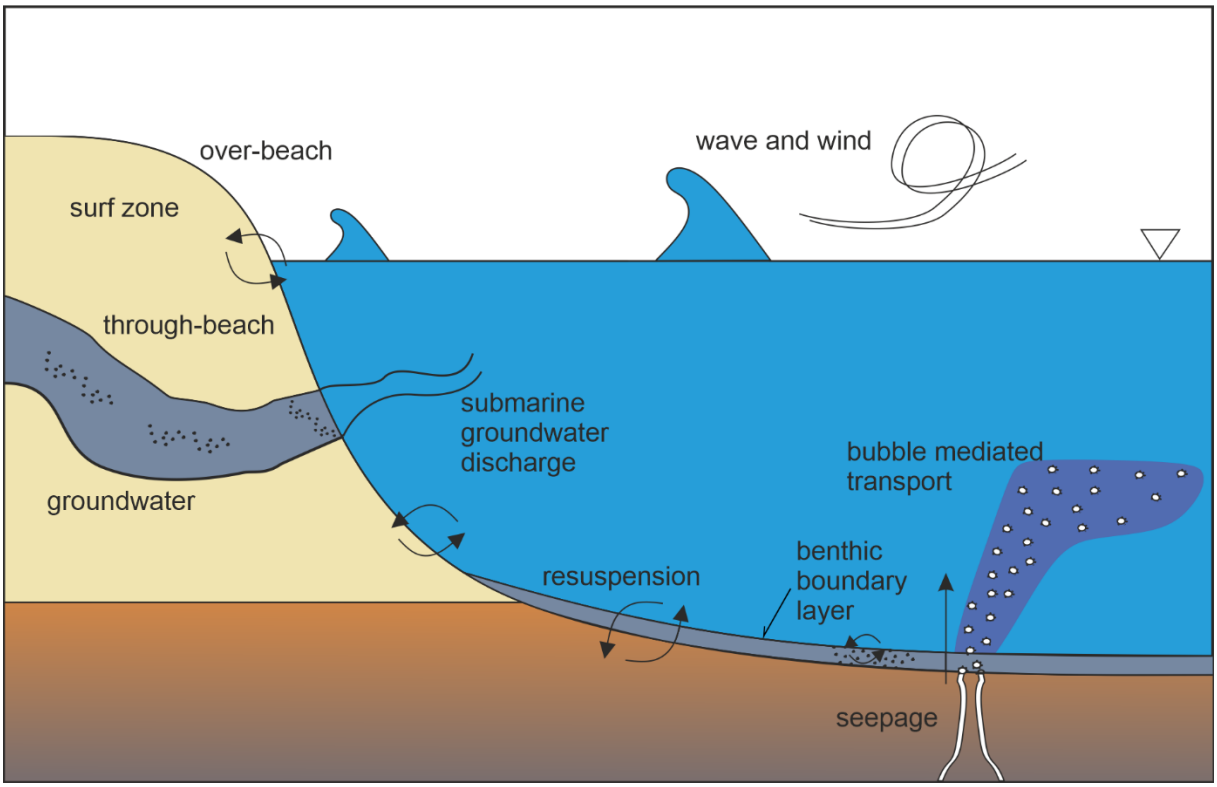

Fig. 9 | Schematic of bentho-pelagic transport processes.

1.3.1 Bubble-mediated transport mechanism

Methane-oxidizing bacteria are frequently found in the water column above methane seep sites (Durisch-Kaiser et al. 2005; Schubert et al. 2006b; Redmond et al. 2010; Steinle et al. 2017), but how these slow-growing microorganisms (Kessler et al. 2011) achieve a significant population density in waters that are renewed continuously by local currents is unclear (de Angelis et al. 1993; Schmale et al. 2015). The findings of previous studies conducted in areas surrounding seep sites (Schubert et al. 2006a; Law et al. 2010; Schmale et al. 2015; Steinle et al. 2016) and mud volcanos (Schubert et al. 2006b) suggested that anaerobic methanotrophic archaea and MOB are transported by methane seep bubbles into the water column (Durisch-Kaiser et al. 2005; Schubert et al. 2006b). This hypothesis was based on the higher abundance of MOB in the vicinity of gas bubble flares than in nearby sites not affected by gas bubble emissions from the sediment.

In addition, it was previously modelled (Sadhal and Johnson 1983) and shown in both laboratory (Zhou et al. 1998; Powelson and Mills 1998) and field studies (Leifer and Clark 2002) that during this bubble formation process surfactants, microorganisms, and fine particles are sorbed onto the gas water interfaces (Wan et al. 1994; Wan and Wilson 1994a; Schäfer et al. 1998). After transportation into the water column it is expected that the shrinking of the bubbles during ascending (McGinnis et al. 2006) and an increased shear (Clift et al. 1978;

Leifer and Patro 2002) enables the release of attached microbial cells into the surrounding water (Jordan et al. 2020). The bubble-mediated transport was first described for wind-driven and wave-induced bubbles at the sea surface, which sparge particles and surfactants from the upper water column and transports them to the sea surface (Bezdek and Carlucci 1972; Wallace and Duce 1978; Cunliffe et al. 2013). In a pilot study at one gas bubble releasing vent site at a shallow nearshore seep field in California, Schmale et al. (2015) found the first indications of a direct bentho-pelagic transport of MOB, by sampling escaping bubbles directly at the gas-releasing vent hole. A comparison showed that the natural bubbles released from the sediment transported more MOB cells than the bubbles that were released from an engineered gas outlet above the sediment surface. Schmale et al. (2015) hypothesized that transported MOB can inoculate overlaying waters, thereby enhancing the efficiency of the pelagic methane sink, although the factors controlling bubble-mediated transport and the effect on the pelagic methane sink were unknown.

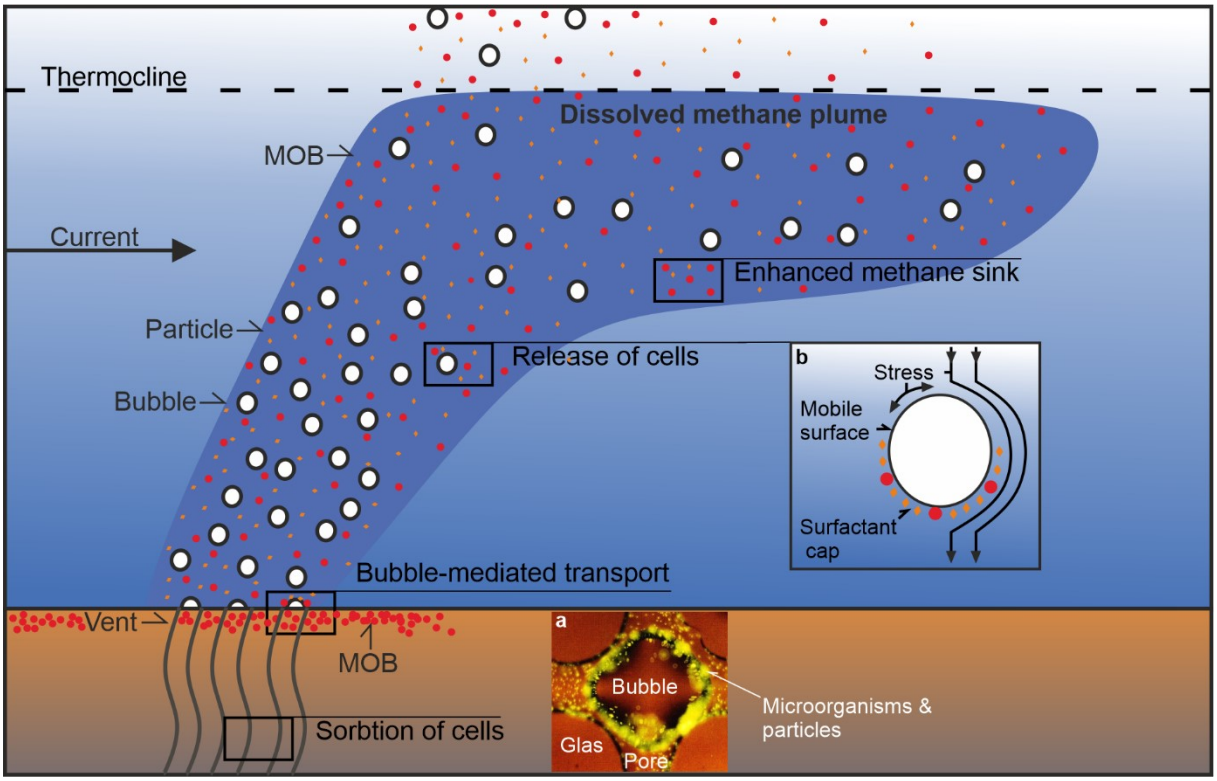

Fig. 10 | Bubble-mediated transport process of benthic microorganisms. Schematic of the transport process. The inlet **a**, depicts the sorption of microorganisms onto a bubble, **b**, shows the surfactant cap model for a bubble and the applied stress. Adapted from Wan and Wilson (1994) and Leifer and Patro (2002), respectively.

2 Motivation and objective

Marine methane is mostly produced in the sediment and substantially oxidized on its way through sediment and water column before reaching the atmosphere. Once released as methane gas bubbles, the methane dissolves in the surrounding water column and is further oxidized before being emitted into the atmosphere. This pelagic methane sink is dominated by aerobic methanotrophic bacteria, which are generally known to have a rather slow doubling time in the range of days. However, in previous studies these bacteria were already found to be present above seep sites. Thus, growth is unlikely to explain the methanotrophs' abundances as continuous currents transport methane and methanotrophs away from the methane sources. First indications of a bubble-mediated transport process that constantly supplies the waterbody with benthic methanotrophs were shown in a pilot study (Schmale et al. 2015). To understand the bentho-pelagic transport of methanotrophs better the aims of my thesis were to:

(1) Determine parameters impacting the bubble-mediated transport process and their influence on the efficiency of the process.

(2) Identify the transported benthic methanotrophs with the help of bubble-catching experiments and compare them to the benthic and pelagic communities, as well as to determine their continuous activity after transportation into the water column.

(3) Evaluate the impact of transported methanotrophs on the pelagic methanotrophic community, the pelagic methane sink, and their influence on the methane turnover within the dispersing methane plume.

In this detailed mechanistic study, I conducted a series of bubble-catcher experiments in the summer of 2017 at two shallow seep sites located at the Coal Oil Point seep field (California, USA). These experiments were conducted across a period of several daytrips to assess the influence of seep intensity, bubble size distribution, and vent density on the efficiency of the bubble-mediated transport of benthic microorganism into the water column. In addition, subsamples from these experiments were incubated to assess the activity of the benthic methanotrophs after transportation. DNA extracts from sediment, Bubble Catcher, and water column were compared to identify transported benthic methanotrophs.

The abandoned well site 22/4b (hereafter 'Blowout', water depth ~100 m) in the North Sea was the center of the second part of my thesis as it is an isolated seep site and thus the related plume waters are not affected by adjacent seep locations. This is very important to quantify the ejection of benthic MOB from a seep into the water column and quantify their impact on the pelagic methane turnover. During the RV Poseidon expedition (Fig. 15) in summer 2016 (POS 504) I collected data on methane related biogeochemical parameters from two transects.

These transects characterize the incoming and outgoing water masses in the vicinity of the Blowout. This way I was able to characterize plume-affected and plume-unaffected waters and thus obtain a robust estimate of the bentho-pelagic MOB transport from the Blowout site and their contribution to the pelagic methane sink. A Lagrangian particle-tracking model was used to investigate the dispersion of the MOB after their ejection from the Blowout into the water column and visualize the plume movement.

3 Methods

3.1 Study sites

3.1.1 The Coal Oil Point seep field

The Coal Oil Point (COP) seep in southern California, USA, extends from the coastline to 3–4 km offshore, with seepage from water depths of a few meters up to 80 m (Fig. 11; Fischer 1978; Leifer et al. 2010; Leifer 2019). COP seeps are primarily or entirely supplied by gas, mostly methane (>90%), from the underlying Monterey Formation through faults and fractures in the overlying Sisquoc Formation (Leifer et al. 2010). Methane originates from thermogenic sources underlying the Santa Barbara Channel, at sub-seafloor depths of 3–4 km (Olson 1982). In a 1995 estimate, seabed emissions of ~1.0–1.5 × 10^5 m^3 d^{-1} gas (88% methane) were reported (Hornafius et al. 1999). Approximately half of this methane dissolves in the water, the other half reaches the atmosphere (Leifer et al. 2000). A dissolved, submerged methane plume then is transported downcurrent remaining detectable for 50 km (Mau et al. 2007).

The COP field allows perfect access for divers and equipment to a variety of gas vents that was a prerequisite for the investigations. Field experiments were conducted between 1 August and 15 September 2017 at two scuba-diver-accessible seep sites in the COP seep field (Fig. **11**, 17), chosen to span a range of seep intensities. The Rostocker Seep is located in 10-m-deep water. Its seeps have a relatively low volumetric gas flow (Schmale et al. 2015), a high methane content (>91%; Kinnaman et al. 2010; Mau et al. 2010), and no oil emissions. The Isla Vista Super Seep, located at 16-m-deep water, has an intense, focused seep area surrounded by extensive dispersed small seep vents, and emits gas bubbles with >95% methane (Mau et al. 2010; Leifer et al. 2010). Previous studies in the COP seep field demonstrated methane oxidation in sediment (Treude and Ziebis 2010) and water column (Kinnaman et al. 2010; Mau et al. 2012).

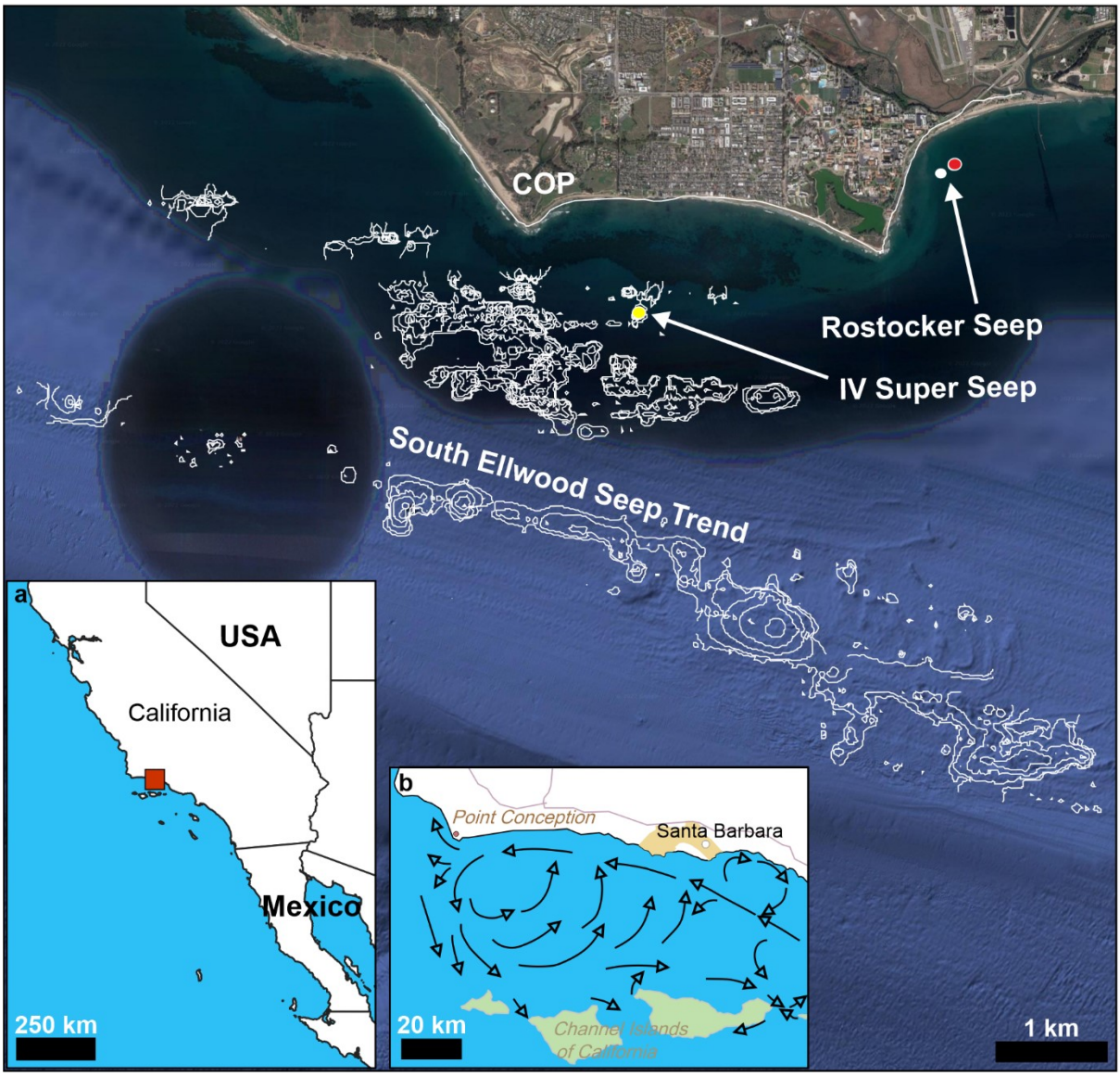

Fig. 11 | Study area one: Coal Oil Point seep field. Satellite image of the Coal Oil Point seep field with an overlay of the active seepage area. The studied seep sites are indicated on the map: Rostocker Seep (red) and IV Super Seep (yellow). Inlet **a**, shows an overview map of California with the Coal Oil Point seep field located as a red square, **b**, depicts the water currents in the Santa Barbara Channel. The map was created using QGIS (v.3.22) and Google Earth satellite images from 2015. The current data is from Leifer (2019) and references therein.

3.1.2 The North Sea blowout well 22/4b

Drilling operations in the Central North Sea in November 1990 (Fig. 12) accidentally hit a shallow sedimentary gas pocket (well 22/4b, 57°55.41'N; 1°37.95'E; Rehder et al. 1998) and caused a massive gas release into the water column. The resulting crater has a diameter of ~60 m and a total depth of ~20 m (e.g., Schneider von Deimling et al. 2015; Steinle et al. 2016). The initial gas release was vigorous but rapidly declined (Leifer and Judd 2015) until it reached a relatively stable *in situ* flux of ~90 L s^{-1} (methane 88–90% vol.; $\delta^{13}C$ ~ −74‰ VPDB; Leifer

2015; Schneider von Deimling et al. 2015). The methane emitted during the blowout was probably released from shallow gas pockets in Quaternary sediments, whose origin presumably lies at greater depths, in Kimmeridge Clay (Upper Jurassic; Leifer and Judd 2015). The large-scale current regime around the Blowout site is controlled by currents driven by density gradients, tides, and wind (Nauw et al. 2015a). The North Atlantic Ocean and its currents (e.g., the Fair Isle current) also influence the water masses and together with the topography, lead to a prevailing north-eastern current direction at the Blowout site (Nauw et al. 2015a). As the waters in the Blowout area are seasonally stratified from April/May until October/November (Nauw et al. 2015a), deep-water masses are largely decoupled from the mixed layer during this period. During thermal stratification, most of the released methane (>95%) is trapped below the thermocline and transported away from the Blowout, together with the sub-thermocline water masses (Leifer et al. 2015; Schneider von Deimling et al. 2015; Sommer et al. 2015).

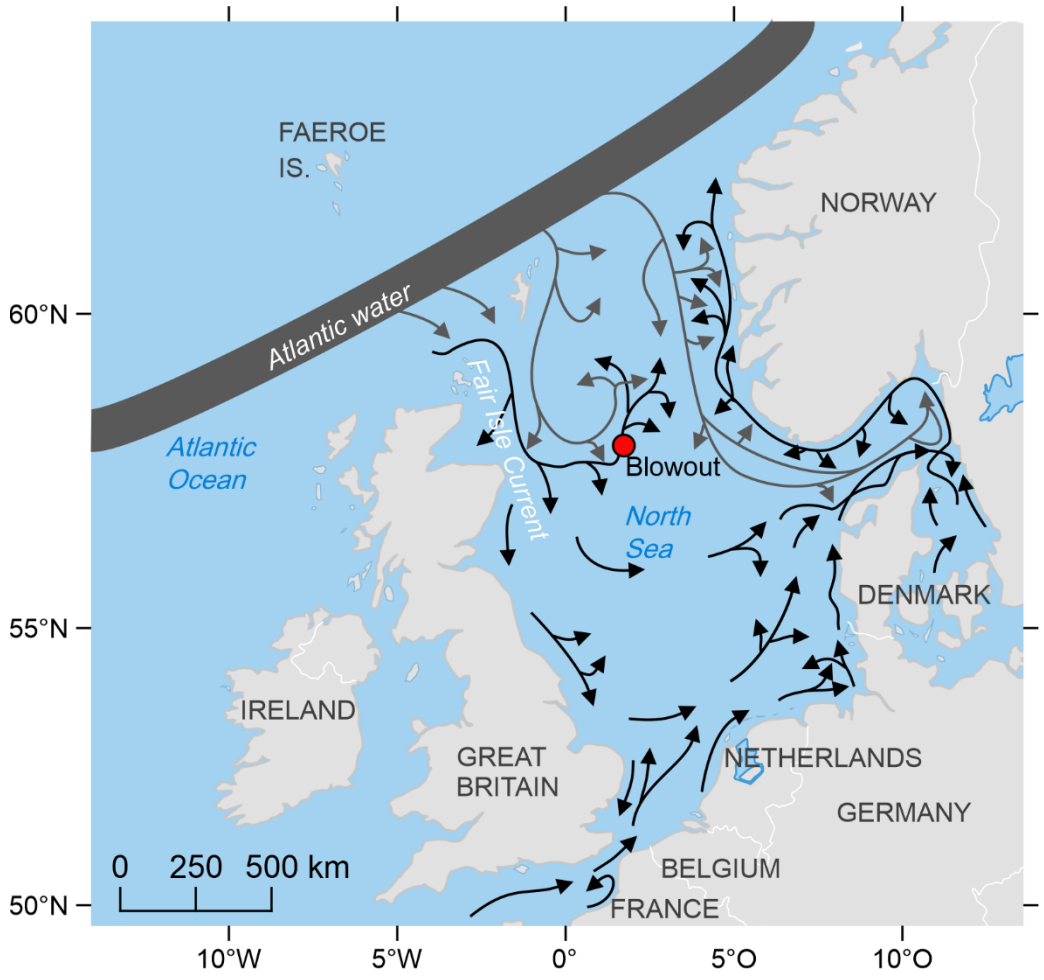

Fig. 12 | Study area two: Blowout location. Overview map of the North Sea with the Blowout marked (red circle) at 57°55.41'N; 1°37.95'E. Water current data adapted from Turrell et al. 1992 and Nauw et al. 2015a and are shown as arrows.

3.2 Sampling procedures

3.2.1 The Coal Oil Point seep field

At the Coal Oil Point seep field, a bubble catching device (see section 3.2.1.1) was used to parameterize the bubble-mediated transport process of benthic methanotrophs into the water column as described in Jordan et al. (2020). Therefore, the sediment as the habitat of the transported methanotrophs, the water column as the destination of this process, and the bubbles as the carrier medium were characterized. An overview of the sampling procedure is displayed in Fig. 13.

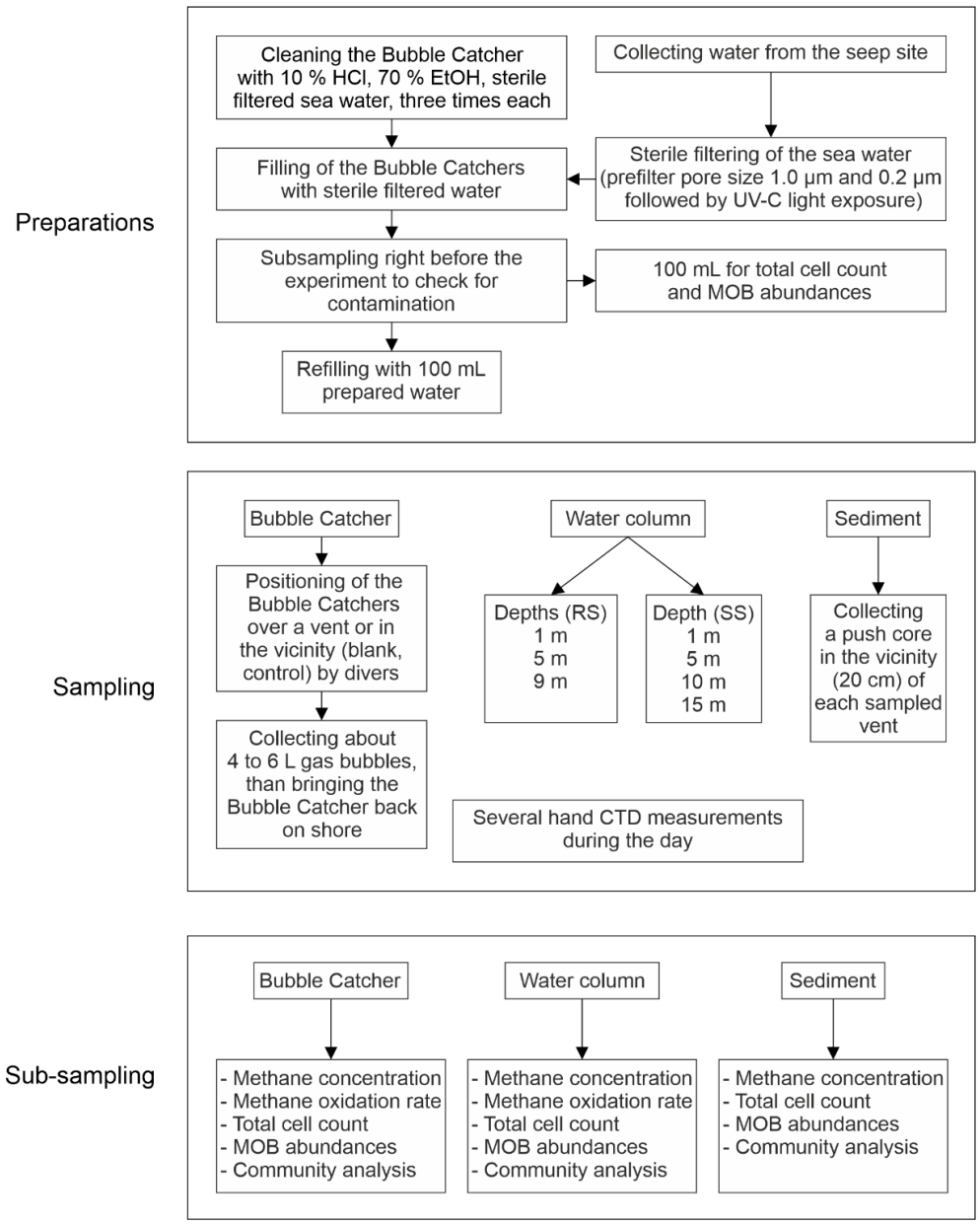

Fig. 13 | Sampling procedure at the Coal Oil Point seep field. Scheme showing the detailed steps to prepare the Bubble Catchers, sampling campaign, and subsampling.

3.2.1.1 The Bubble Catcher

As described in Jordan et al. (2020), a bubble catching device (Fig. 14) with a sampling cylinder made of borosilicate glass and a volume of 12.7 L was used to sample seep bubbles directly after the release from the sediment. The sampling device and method were adapted from Schmale et al. (2015). To prevent overpressure during surfacing, the sampling cylinder is equipped with a pressure relief valve on top. A funnel was used to guide the bubbles from the seafloor into the cylinder and a stopcock to control the gas inlet (Fig. 14). A metal frame (outer dimensions: 35 cm x 35 cm x 90 cm) served as damage prevention for the sampling cylinder, better handling, and more precise positioning by the divers.

The Bubble Catcher (BC) was cleaned with HCl (10%), rinsed with ethanol and sterile-filtered seawater three times each before the next experiment to minimize cross-sample contamination. Subsequently, the cylinder was filled with sterile-filtered seawater to reduce the initial bacteria load as much as possible. Therefore, seawater was taken from the University of Santa Barbara's seawater pump house (before further processing), which is supplied by two pipes extending ~500 m into the ocean at a water depth of ~15 m. Sterile-filtration was conducted by using a pumped filter system with a 1.0 µm prefilter (Polycap SPF 36 capsule filter, 1.0 µm, Whatman, USA) and a 0.2 µm main filter cartridge (Polycap AS 36 capsule filter, 0.2 µm, Whatman, USA) before the water passed a UV-C light (reeflexUV 350, Eheim, Germany). The filters were exchanged before each sample day and two filter systems, with one peristaltic pump each (Cole Parmer Masterflex, console drive, USA) were run in parallel, one for each Bubble Catcher. The Bubble Catchers were filled the night before sampling, as the procedure took several hours. Thus, a 100 mL subsample was taken per Bubble Catcher right before transfer onto the boat to check for any contaminations. These subsamples were stored at 4 °C and processed with the other CARD-FISH samples at the end of each sampling day.

During the experiment, the captured bubbles (total gas volume 4-6 L) displaced Bubble Catcher water. Particles and microorganisms associated with the seep bubbles were released into the sterile-filtered water in the sampling cylinder after the bubbles had burst. Experiment durations and collected gas volumes were used to calculate the volumetric gas flow (mL s^{-1}). After gas collection, the vent was marked and the Bubble Catcher was returned to the boat and the Bubble Measuring System (BMS) was deployed from a second vessel and positioned at the exact same vents. Push cores were taken last as they disrupt the sediment. Water column sampling was conducted during the runtime of the Bubble Catcher experiments. Bubble Catcher subsampling occurred within 1 h after return to shore.

To parameterize the bubble-mediated transport process, gas bubbles were sampled from different gas vents of the Rostocker Seep and IV Super Seep sites. The sampling process is shown schematically in Fig. 14. Three experiment types were conducted; details and an

overview of the experiments duration and sampled gas volumes are provided in Table 2. For the “BC vent” experiments, divers placed the Bubble Catcher above an active natural gas vent. In the “BC engineered” experiments (“BC blank” in Schmale et al. 2015), the Bubble Catcher was placed above an engineered gas bubble source, created by air released from a pressure tank, positioned at least ~1 m from any gas vent. The bubble stream was adjusted to resemble volumetric flow and bubble size of natural vents in the vicinity. In “BC control” experiments, no bubbles were introduced into the Bubble Catcher, which was positioned as described for the “BC engineered” experiments. During subsampling, residual water in the Bubble Catcher was homogenized using a sterilized mixing rod, inserted through a small opening at the top of the Bubble Catcher, and filled into prepared sampling containers. The water sample was transferred via a sterilized glass funnel that was placed on the bottom of the respective container. Samples for methane oxidation rates determination and methane concentration measurement were subsampled bubble free without sample overflow, due to sample volume limitation. Total sample volume was determined by incremental filling. Methane concentration, MOB abundances, MOB community, and methane oxidation rates (only determined in the water column and Bubble Catcher) were analyzed from: (i) residual Bubble Catcher water, (ii) the sediment, and (iii) the water column.

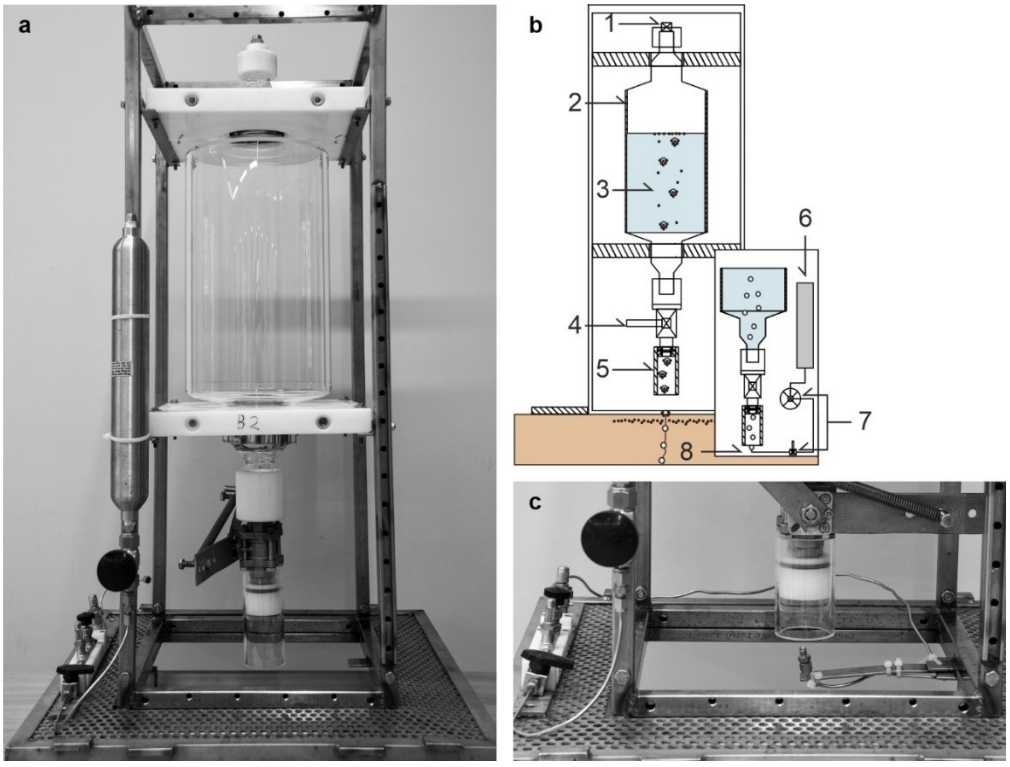

Fig. 14 | The Bubble Catcher. Bubble sampling device **a**, Bubble Catcher frontal view, **b**, schematic view **c**, Bubble Catcher blank setting with an engineered bubble source beneath the funnel. The Bubble Catcher setup consists of: 1) Overpressure valve, 2) sampling glass cylinder, 3) sterile filtered seawater, 4) stop-cock, 5) funnel, 6) pressure tank, 7) valves for flow regulation, 8) 1/8” gas outlet.

Table 2 | Overview of the conducted bubble catching experiments. Bubble catching experiments as shown in Jordan et al. (2020) listing the dates, sampled gas volumes, experiment durations, volumetric gas flows, transported bubble surface, and ration of bubble surface to volume (*A/Q*) for selected experiments.

Experiment	Date	Gas volume [L]	Duration [min]	*Q* [mL s^{-1}]	*A* [cm^2 s^{-1}]	*A/Q* [cm^{-1}]
RSV1	01.08.17	0.7	160	0.07	0.8	10.5
RSV2		2.85	160	0.3	5.1	17.1
RSV3	02.08.17	4.85	111	0.73		
RSE1		4.66	67	1.16		
RSB2	15.08.17	4.7	84	0.93		
SSV1	07.08.17	5.13	50	1.71	30.9	18.1
SSV2		5.42	41	2.2	39.6	18
SSV3	08.08.17	4.7	197	0.4		
SSE1	14.08.17	5.59	9	10.35		
SSC1	15.09.17	0	67	0		
SSC1		0	69	0		

3.2.1.2 Sediment and water column

Sediment samples were collected as push cores (length 30 cm, inner diameter 5 cm) to determine sediment methane depth profiles and confirm the presence of MOB that could be transported into the water column.

Consistent with the high vent density at IV Super Seep the cores SSV1 and SSV2 were taken from sites of active venting. Other cores were taken at a distance of ~15 cm from any active vents. Cores for methane determination were processed on land directly by subsampling sediment plugs horizontally through openings pre-drilled in the core-liner at 1.5 cm depth increments to a maximum depth of 10.5 cm, using 3 mL cut-off plastic syringes. Cores for MOB abundance analyses were cooled (4 °C) during transport to the laboratory and kept refrigerated (4 °C, 18-42 h) until subsampled in 1.5 cm increments.

The physical, chemical, and biological parameters of the water column were monitored to characterize seawater in proximity to Rostocker Seep and IV Super Seep. Salinity, temperature, and depth were monitored periodically over the course of a fieldwork day using a handheld sensor (CTD48M, Sea & Sun Technology GmbH, Germany). Water samples were collected with a 2 L handheld water sampler (LIMNOS, Finland) at depths of 1, 5, and 9 m at Rostocker Seep site and 1, 5, 10, and 15 m at IV Super Seep site.

3.2.2 The North Sea blowout well 22/4b

The interest in this thesis was to characterize the impact of the ejection of benthic MOB from a mega seep into the water column and to determine the effect on pelagic methane dynamics. This required the selection of an isolated seep site and a carefully planned sampling strategy that considered the dynamics of the prevailing current system (including tidally triggered current changes), that determine the dispersion and thus the fate of the methane transported within the plume. In the summer of 2016, during an expedition of the RV Poseidon (POS 504) to the abandoned well site 22/4b, gas release activity in the Blowout region was verified using hydroacoustic methods (see section 3.3.7). On August 30, 2016, an acoustic Doppler current profiler (ADCP) was deployed during the first remotely operated vehicle PHOCA 3000 (ROV) dive. The ADCP was positioned ~800 m northeast of the Blowout, at a depth of 90 m, and data on the actual current regime was gathered for 92 h (Fig. 15, see section 3.2.2 for details). The ADCP was retrieved ~4 days later, and its data was extracted and processed (see section 3.3.7.2) to plan subsequent sampling. Two water-column transects positioned orthogonal to the residual background current were defined: one upstream of the Blowout (IN transect) and the other downstream (OUT transect). The aim was to obtain undisturbed measurements at the IN transect and capture the Blowout plume in the OUT transect, which together would allow for a robust estimate of the fluxes across the Blowout site (Fig. 20). To avoid biased estimates due to tidal currents, both transects were sampled ~24 h apart during the same tidal phase (low tide), since tides can shift the currents on an hourly basis. Sampling took place on September 4, 2016, 22:12–00:19 (OUT) and September 5, 2016, 22:08–23:30 (IN). The IN transect was positioned to include three stations (west to east I1–I3, total distance ~1.65 km) located ~1.6 km upstream of the Blowout. The OUT transect, with five stations (west to east O1–O5, total distance ~1.74 km) was sampled ~1.6 km downstream. Methane biogeochemical parameters (described in section 0) were measured at all stations at seven depths (10 m, 20 m, 35 m, 50 m, 65 m, 80 m, ~90 m). The experimental setup was designed to capture the center of the plume. Thus, there was a trade-off between a longer transect length and better plume coverage versus a sampling duration short enough to provide an instantaneous snapshot of the methane dynamics. In addition to the stations along the two transects, water samples were collected above the Blowout and at a background site (BG) ~5 km northwest of the Blowout (Fig. 20).

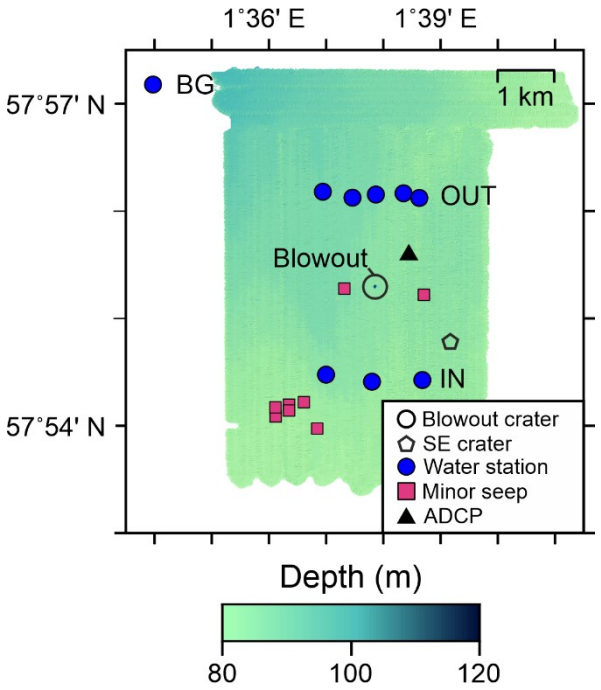

Fig. 15 | Mercator map showing the bathymetry and sample stations around the Blowout crater. Bathymetry is shown as a green-blue background. The station map shows the positions sampled (blue circles) for the IN and OUT transects, the background station (BG), and the station directly above the Blowout crater (encircled). Natural seeps (red squares) and a smaller south-eastern crater (pentagon) are also shown. The acoustic Doppler current profiler (ADCP, black triangle) is northwest of the Blowout. Positions and sampling dates are listed in Table 3. Adapted from Jordan et al. (2021)

3.2.2.1 Water column

The water column was sampled to characterize the water masses and determine the biogeochemical and microbiological parameters of those in the vicinity of the Blowout. Sampling was conducted using the SBE 32 Carousel water sampler, which was mounted with 12 × 5 L free-flow sampling bottles (Hydrobios, Germany) and a pumped CTD system (SBE 911plus, Seabird Electronics, USA) that logged salinity, temperature, and depth. Water samples were collected from within the surface mixed layer (10 m, 20 m), below the thermocline (35 m), and in deep waters (50 m, 65 m, 80 m, ~90 m). At each depth, the subsamples were analyzed for their methane concentration, methane oxidation rates, and the abundance of MOB. Vertical and cross-sectional inventories were calculated using the trapezoid method (Schmale et al. 2012b).

Table 3 | Station coordinates and sampling time.

Station	Date	Time (UTC)	Location	Lat (N)	Long (E)
BC	31.08.16	07:35:00	Blowout	57.92179	1.63154
O1	04.09.16	22:12:00	OUT Transect	57.93633	1.61573
O2	04.09.16	22:42:00	OUT Transect	57.93542	1.62431
O3	04.09.16	23:12:00	OUT Transect	57.93591	1.63116
O4	04.09.16	23:56:00	OUT Transect	57.9361	1.63921
O5	05.09.16	00:19:00	OUT Transect	57.93537	1.64381
I1	05.09.16	22:08:00	IN Transect	57.90794	1.61662
I2	05.09.16	22:57:00	IN Transect	57.90684	1.63004
I3	05.09.16	23:30:00	IN Transect	57.9071	1.64471
BG	06.09.16	00:34:00	Background	57.95298	1.56624

3.3 Sample processing and analysis

3.3.1 Methane concentration

Methane concentration were analyzed in both sampling campaigns to describe the seeps' impact on the methane concentration in the water column. In the case of the COP, 125 mL sample water from the Bubble Catcher and water column were filled into crimp vials, whereas 250 mL sample volume was taken during the Poseidon expedition (POS504). To avoid trapped gas bubbles and air contamination, the vials were flushed with up to twice the volume of sample water. All samples were cooled (~3 h, 4 °C) until poisoned, or directly poisoned with a saturated $HgCl_2$ solution (1 µL per mL sample), and sealed with silicon (Wilson et al. 2018). Samples were stored in an inverted state until analysis in the laboratory.

For sediment samples from COP, two cm^3 per depth were transferred into crimp vials (10 mL) filled with 5 mL NaOH (2.5%). Vials were closed immediately and shaken to mix the NaOH and sediment thoroughly in order to stop any biologic activity. Subsequently, the rubber stoppers were sealed with silicon and samples were stored upside down in the fridge (4 °C) until headspace analysis.

3.3.1.1 Headspace analysis

Water column samples from the COP were analyzed applying the headspace method described by Jordan et al. (2020) adapted from Magen et al. (2014). In general a 10 mL nitrogen headspace was applied to the stored samples using a syringe. The syringe was flushed three times with nitrogen to prevent air contamination. Excess water was collected

using a second syringe. The sample bottles were weighed before and after applying the headspace to calculate the headspace's volume. Following this, the bottles were shaken vigorously for 1 minute and stored upside down for 48 h to equilibrate.

The samples were analyzed for methane by manually injecting 30 µL of headspace gas with a gas tight syringe (Hamilton 100 µL) into a gas chromatograph (Agilent GC 7890 B, temp. program 45 °C). Each sample was analyzed twice. If the mean deviation between the measurements was >1%, a third measurement was conducted. For calibration, two standard gases were used with (1) 97.7 ppm CH_4, injection volume 50 µL, and (2) 3950 ppm CH_4, injection volume 20 µL, in syn. air (Linde) with an uncertainty of ± 2% by manufacturer. The standards were measured five times with a mean deviation of <1% at the beginning and end of each day.

3.3.1.2 Purge-and-trap analysis

Samples for methane concentrations from the Poseidon expedition (POS504) were analyzed as described in Jordan et al. (2021) adapted from (Jakobs et al. 2014) using a purge-and-trap system. Subsamples of 20 mL were purged for 15 min with helium, and volatiles were focused on a cold-trap at −120 °C before being desorbed at 95 °C and analyzed using gas chromatography (Shimadzu GC-2014, HayeSep Q, mesh 80/100, 2 m × 1/8" × 2 mm, stainless steel, oven temperature 45 °C). The calibration standards consisted of methane in synthetic air (Linde Group, Ireland) at two concentrations (18.47 ppm and 36.94; ppm with an uncertainty of ± 2% according to the manufacturer).

3.3.2 Methane oxidation rates

Methane oxidation rates were determined to assess the transported methanotrophs' impact on the pelagic methane sink in the North Sea and to study the survival of the transported MOBs. Water samples (100 mL, crimp vials) were taken bubble-free as described in section 3.3.1 and sealed with non-toxic PTFE-coated chlorobutyl rubber stoppers (Wheaton, USA; Niemann et al. 2015). All samples were cooled (4 °C) until further handling in the lab. The measurement procedure was published in Jordan et al. (2020) and adapted after Bussmann et al. (2015). In general, 20 µL, about 50 kBq, of gaseous tracer (^3H-CH_4; American Radiolabeled Chemicals, USA) diluted with nitrogen (1:3) and a specific activity of 0.37–0.74 TBq $mmol^{-1}$ was added to every sample from the COP while 10 µL of diluted radioactive tracer ^3H-CH_4 (1:4 with N_2, ~30 kBq, specific activity 0.37–0.74 TBq $mmol^{-1}$) was added to water samples from the North Sea. The tracer was injected through the chlorobutyl stoppers and crimp vials were incubated at *in situ* temperature in the dark for ~3 days. After incubation, the vials were opened and two

2-mL subsamples were taken and filled into 7 mL glass scintillation vials (Pico Glass Vial, 7 mL, with 15 mm foil-lined, white urea screw caps, PerkinElmer). One sample was degassed for 5 min to remove ^{3}H-CH_4 and then used to determine the amount of formed ^{3}H-H_2O. The other sample remained untreated to measure the combined content of ^{3}H-CH_4 and ^{3}H-H_2O. Both samples were mixed with 5 mL of Ultima Gold LLT (PerkinElmer, USA) and analyzed by liquid scintillation counting (COP: TRI-CARB 4910TR, PerkinElmer; North Sea: Triathler Multilabel Tester, Hidex). Based on the results, the first-order rate constant k' was calculated according to Eq. 4:

$$k' = (^3\text{H-}H_2O/(^3\text{H-}CH_4 + {}^3\text{H-}H_2O))/t \quad (4)$$

where ^{3}H-H_2O is the radioactivity (counts per minute = cpm) of the product of methane oxidation, (^{3}H-CH_4 + ^{3}H-H_2O) is the radioactivity (cpm) of the initially injected ^{3}H-CH_4 radiotracer, and *t* is the incubation time. A final multiplication of k' by the respective methane concentration [CH_4] resulted in the methane oxidation rate (MOx), as shown in Eq. 5.

$$MOx = k' * [CH_4] \quad (5)$$

The turnover time τ for methane is defined as the reciprocal value of k' (Eq. 6):

$$\tau = 1/k' \quad (6)$$

3.3.3 Quantification of MOB

3.3.3.1 Catalyzed reporter deposition fluorescence in situ hybridization

MOB and total cell counts were determined to calculate the MOB abundances and to parametrize the transport of benthic methanotrophs and their impact on the water column. Samples from the sediment, water column, and Bubble Catcher samples taken at the COP as well as water column samples from the North Sea were analyzed using catalyzed reporter deposition fluorescence *in situ* hybridization (CARD-FISH). CARD-FISH is a gene hybridization method (Pernthaler et al. 2002) that, in this case, targeted methanotrophs' type I and II specific 16S-rRNA gene sequences. The protocol used was described in Jordan et al. (2020), which was adapted after Pernthaler et al. (2002). In general, the cells were fixed in water samples (COP: 20 mL, North Sea 100 mL) using formaldehyde with a final concentration of 4% during an incubation at 4 °C for 2–4 h in the dark. Subsequently, the water samples were filtered on 0.2 µm isopore filters (GTTP, Merck Millipore, USA), rinsed, and stored at -20 °C. For sediment samples 0.5 cm^3 of each depth were fixed with formaldehyde as described in Treude and Ziebis (2010). In the laboratory, fixed sediment samples were diluted (1:3000) with phosphate-buffered saline and treated with ultrasound (Bandelin HD70, Sonopuls, Germany) for 25 s at an amplitude of 40 W and cycle at 15% (Schmale et al. 2015) to detach cells from sediment grains. A subsample (3 mL) was filtered on 0.2 µm isopore filters (GTTP, Merck Millipore, USA)

and stored at -20 °C. For analysis, filters were further processed following the protocol of Pernthaler et al. (2002). After an initial embedding with low gelling point agarose (0.1%), cells were permeabilised with lysozyme at 37 °C (1 h) and endogenous peroxidases were inactivated with methanol and H_2O_2 (0.15%). Hybridization took place with a mixture (1:1:1) of three probes (type I: M(γ)84 and M(γ)705; type II: M(α)450; Eller et al. 2001) for methanotrophs with a formamide concentration of 20% at 46 °C for 3 h. The probes were coupled with horseradish peroxidases, which activated fluorescein labelled tyramides and thus specifically stained (46 °C, 30 min, in the dark) MOB cells. Filters were counterstained with the general DNA fluorescence dye 4′,6-diamidino-2-phenylindole (DAPI) to determine total cell counts. For a general bacteria stain (positive control) and a negative control with each analysis batch, one random sample filter each was hybridized with EUB338I-III (35% formamide, 46° C; Amann et al. 1990; Daims et al. 1999) and non-EUB (35% formamide, 46° C; Wallner et al. 1993) probes, respectively. Filters made from *Methylococcus capsulatus* (methanotroph type I) and *Methylosinus trichsporium* (methanotroph type II) cultures were used for the control of methanotroph-specific probes with each analysis batch.

The cell counts for the Bubble Catcher experiments were corrected and calculated as stated in Jordan et al. (2020). Each Bubble Catcher experiment was corrected for the number of cells inside the Bubble Catcher prior to its deployment. Determined cell numbers in the “BC vent” and “BC engineered” experiments were also corrected for the cell numbers in the “BC control” experiments. The number of cells mL^{-1} was multiplied by the water volume of the residual sample to determine the number of transported cells per Bubble Catcher and then divided by the volume of captured gas to calculate the transported cells mL_{gas}^{-1} (Fig. 22). These rates were multiplied by the volumetric flow to obtain the number of transported cells s^{-1} (Fig. 22a). The number of transported cells per bubble surface area (cells cm^{-2}) was determined from bubble size distributions measured by the BMS (Fig. 22c). The number of transported cells m^{-2} d^{-1} (Fig. 22d) was calculated by multiplying the number of transported cells s^{-1} by the vent density.

3.3.3.2 Droplet digital PCR

An additional way to quantify MOB is by determination of the *pmoA* gene abundances. Therefore, the QX200™ Droplet Digital PCR System (Bio-Rad, München, Germany), in short ddPCR, was chosen to establish a rapid and state of the art method to quantify MOB in the environment with a low detection method. This PCR method allows quantification of template DNA down to 0.1 pg (Wäge et al. 2020). Thereby, the sample procedure is the same as for DNA sequencing-based community analysis.

The ddPCR system was used with the primer set introduced in Jordan et al. (2020), A189fmod and mb661rmod (forward: GGNGACYGGGAYTTCTGG, reverse: CMGGMGCAACGTCYT TACC), a combination of two established sets (Costello and Lidstrom 1999; Tavormina et al. 2008). The general ddPCR technology utilizes a water-oil emulsion using a combination of microfluidics and proprietary surfactant chemistries to create ~20000 nano-sized droplets containing all PCR reagents including template DNA (Hindson et al. 2011). Thus, each droplet creates an isolated space for an independent PCR reaction. Following the droplet generation, the reaction tubes containing these droplets are put into a thermal cycler running the temperature program. During the PCR reaction, a fluorescent dye binds to double-stranded DNA enabling detection of amplicons. The droplets are then extracted from the reaction tube and single droplets are detected by a laser system. Thereby, droplets with an amplification of the target DNA fluoresce, whereas droplets without amplification do not. For this procedure, it is important to sufficiently dilute the template DNA (several thousand negative droplets are needed), as the data analysis software uses Poisson's law to calculate the amount of template DNA present in the positive droplets.

The ddPCR reaction was conducted in accordance with the instructions from (Wäge et al. 2020) with some adaptations. In general, to 11 µL supermix (QX200™ ddPCR™ EvaGreen® Supermix), forward/reverse primer with a final concentration of 100 nmol L^{-1} and template DNA were added and filled to 22 µL with DEPC H_2O. Following a thorough mixing, 20 µL of each PCR reaction was transferred to the respective slot on the Droplet Generator DG8™ Cartridge (Bio-Rad) and supplemented with QX200™ Droplet Generation Oil for EvaGreen (70 µL; Bio-Rad). Droplets were generated using the QX200™ Droplet Generator (Bio-Rad). The droplet-emulsions were pipetted into a 96-well PCR-plate, which was heat sealed with a pierceable foil using the PX1™ PCR Plate Sealer (Bio-Rad). The sealed plate was loaded into the C1000 Touch™ Thermo Cycler (Bio-Rad) and the temperature program was run.

The temperature gradients for both systems are shown in Fig. 16a, b with optimal annealing temperatures of 60 °C and 55 °C for A189/mb661 and A189mod/mb661mod, respectively. Optimization of the number of cycles, an increase from 40 cycles to 50 and 60 cycles, only increased the amount of rain, which refers to droplets with an Ch1 amplitude between the positive band (~20000) and the negative band (~4000–5000). Amplification was hampered in extracts from formaldehyde fixed samples (see section 3.3.3.1) in comparison to extracts from DNA filters (see section 3.3.4.1, Fig. 16c, d).

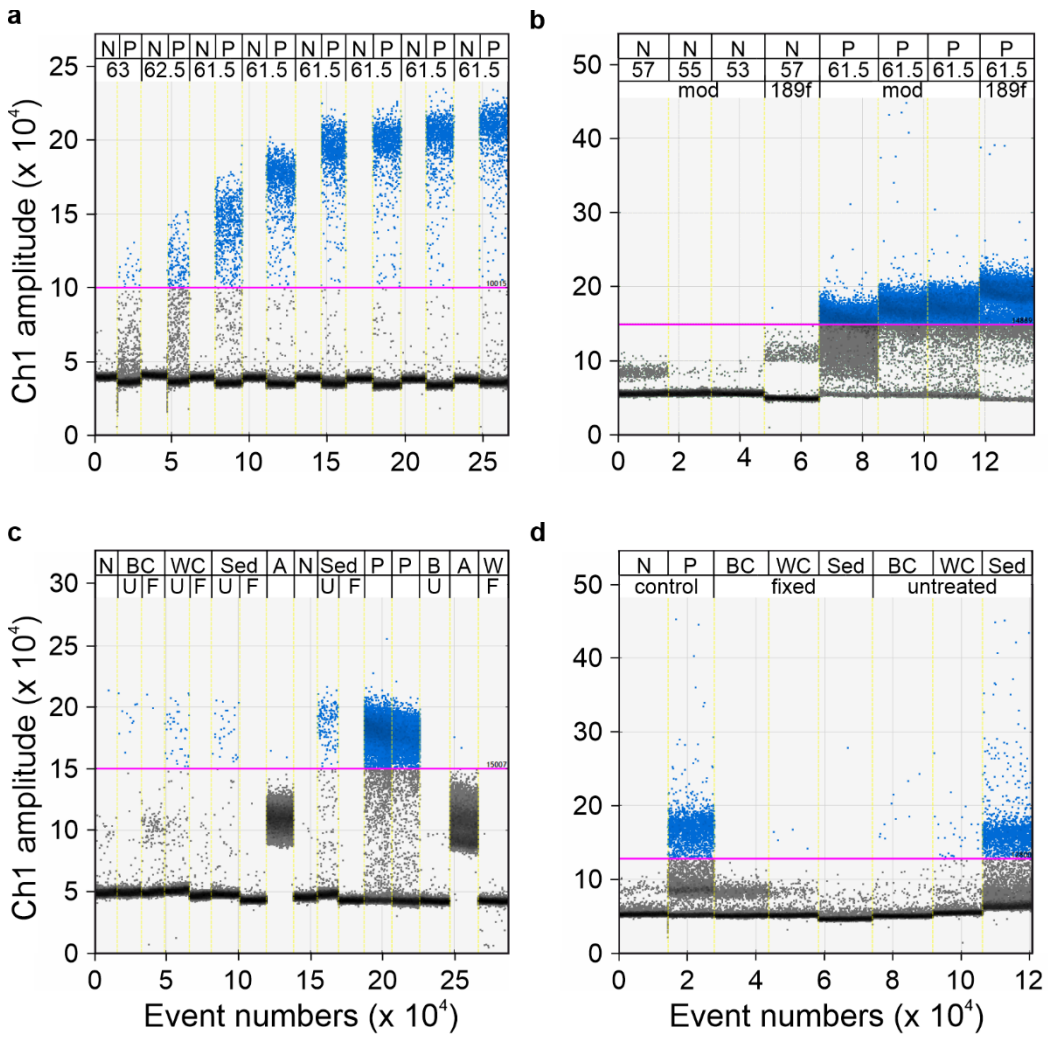

Fig. 16 | ddPCR analysis regarding MOB abundance. Temperature gradients for primer systems **a**, A189/mb661 (189f) and **b**, A189mod/mb661mod (mod), with negative (N) and positive (P) controls. Temperature in the figure is displayed in degree Celsius. DNA extraction from untreated samples (U) and samples fixed (F) with formaldehyde (4%) from Bubble Catcher experiments (BC, B), water column (WC, W) and sediment (Sed) are displayed in **c** and **d**. Amplification of a *pmoA* amplicon (A) did not yield any negative droplets because too much template was present.

The optimized program is listed in Table 4. Each PCR reaction was accompanied with a positive and negative control, whereas the latter included all reagents except for the DNA template, which was replaced with diethylpyrocarbonate treated water. Extracted DNA from a *M. capsulatus* culture was used as a template in the positive controls. For experiments with samples extracted from formaldehyde fixed filters, DNA from fixed *M. capsulatus* cells was used as positive controls.

Table 4 | ddPCR temperature profile. The 3-step PCR protocol was run with a ramp rate of 2°C s^{-1}.

Step	Temperature (°C)	time (min)	
Initial denaturation	94	4	
Denaturation	94	1	× 40 cycles
Primer annealing	55	1	
Elongation	72	1	
Final elongation	72	5	
Preservation	4	∞	

The first amplifications with environmental samples using the ddPCR method described above were promising (Fig. 16c, d). The highest droplet count was measured in sediment surface samples (DNA) with indications of better performance with the A189mod/mb661mod system. However, both systems tested were able to amplify template DNA from the Bubble Catcher and water column samples. In contrast, DNA extractions from formaldehyde-fixed filters yielded hardly any amplification from water column and sediment samples and none from Bubble Catcher samples. Thus, untreated filters stored at -80 °C is the preferred starting material for this method.

A proof of principle was achieved with these experiments, however as the method was not used to analyze project-related samples, it is only discussed in this section. In future, the detection limit for the primer sets has to be determined using a serial dilution down to 0.1 pg template DNA. Afterwards samples can be analyzed by normalizing the copy number to e.g., copies/10 ng to account for differences in template DNA as described by Wäge et al. (2020). In addition, it has to be borne in mind that gene and operon counts can differ on species and up to kingdom level. For example bacterial genomes display up to 15 16S rRNA gene operons with the majority on one and two operons, whereas archaea can have up to five, but typically only have a single operon (Acinas et al. 2004).

Altogether, formaldehyde fixed DNA samples were unsuitable for this detection method as amplification appeared to be restricted. However, the use of freshly extracted DNA resulted in usable amplification and should be further refined and validated as it increases the detection limit and sample throughput and can reduce sample preparation time as the same extracted DNA can be used for ddPCR and sequencing.

3.3.4 Genetic analysis

3.3.4.1 DNA extraction

For DNA analysis, Bubble Catcher and water column samples, both taken at COP, were filtered on hydrophilic polycarbonate membrane filters (0.22 µm, 47 mm, Merck Millipore, Darmstadt, Germany), which were stored at –80 °C until analysis. To ensure sufficient biomass, 0.5–1 L (water column) and 1–2 L (Bubble Catcher) sample water were filtered. For sediment samples, the sediment's upper 1.5 cm of the core was homogenized and a subsample was transferred to a cryogenic vial that was stored at −80 °C until extraction. DNA was extracted from one-quarter of the membrane filter (for water column samples) or 0.25 mg of wet sediment with the DNeasy PowerSoil Pro kit (Qiagen, Hilden, Germany).

3.3.4.2 16S rRNA gene and pmoA analysis

To identify the transported bacteria the V3-V4 region of the 16S rRNA gene was targeted using the primer set 451f-805r (forward: CCTACGGGNGGCWGCAG, reverse: GACTACHVGGG-TATCTAATCC; Herlemann et al. 2011). Since the establishment of the first *pmoA* primer set (A189/A682; Holmes et al. 1995a) several other primer sets were established (e.g., Bourne et al. 2001; Horz et al. 2001; Shrestha et al. 2012) with some being more specific for individual groups (Luesken et al. 2011). Nevertheless, the most frequently used set is still the one that was first established. To exclude the amplification of the *amoA* gene of ammonia-oxidizing bacteria an alternative system was published (A189/mb661; Costello and Lidstrom 1999). However, these primer systems were designed with sequences of terrestrial and freshwater methanotrophs, and a study by Tavormina et al. (2008) indicated that they contain up to two mismatches per primer for vent-associated methanotrophs. Thus, a combination of the Costello and Lidstrom (1999) and Tavormina et al. 2008 primer sets were used in this thesis, the primer set A189fmod and mb661rmod (forward: GGNGACYGGGAYTTCTGG, reverse: CMGGMGCAACGTCYTTACC). LGC Genomics GmbH (Berlin, Germany) performed library preparation and sequencing on an Illumina MiSeq V3 (600 cycle, 2×300 bp, 5 million reads. Sequences were deposited in the European Nucleotide Archive (ENA) under accession number PRJEB34318 (16S rRNA gene) and PRJEB34319 (*pmoA*). 16S rRNA gene amplicon sequences were grouped into operational taxonomic units (OTUs) based on a similarity >97% and classified to the genus level.

16S rRNA gene amplicon read processing and annotation were conducted using Mothur v. 1.39.5 (Kozich et al. 2013; MiSeq SOP: accessed on 02.04.2019). Taxonomic annotation was accomplished using the Silva database (release 132), including the taxonomic changes proposed by Parks et al.(Parks et al. 2018). For *pmoA* sequences, the raw sequences were processed with DADA2 v. 1.12.1 (Callahan et al. 2016), which uses amplicon sequence

variants (ASVs) instead of OTUs, and taxonomically annotated according to the reference database (Yang et al. 2016). The phylogenetic analysis was performed with R v. 3.5.1 (R Core Team, 2018) and phyloseq v. 1.26.0 (McMurdie and Holmes 2013).

OTUs (for 16S analysis) were selected based on their taxonomic relationship to described MOB. ASVs present in at least two sample groups were selected. OTUs and ASVs present in control samples were removed from the analysis. Samples were grouped according to their sample origin (sediment, “BC vent”, water column, “BC engineered”). The mean relative abundance per group and per OTU/ASV was calculated and visualized with ggplot2 (Wickham 2009).

3.3.5 Bubble size distribution

The bubble size distribution was determined to characterize the vents sampled. The therefore utilized bubble measurement system and the underlying analysis algorithms were described in previous studies (Leifer et al. 2003, 2009; Leifer and Boles 2005; Leifer and Tang 2007; Leifer 2010). The bubble size distribution measurement was described in Jordan et al. (2020) and conducted as follows. The Video was digitized at 60 fps. All bubbles in a sequence were identified and tracked manually due to high particle and detritus concentrations in the samples. Tracking assistance was provided by the algorithms in ImageJ (Schneider et al. 2012). Once a bubble was selected in two sequential frames, the algorithm predictively attempts to select the same bubble in the next frame based on the expected vertical displacement. If the predictive attempt failed, then the bubble was selected manually. The bubble equivalent spherical radius, r, was determined from a best-fit ellipse of the bubble outline, both with and without a convex hull. Further analysis was conducted using custom routines in MATLAB (Mathworks, MA). The velocity of tracked bubbles was derived and a polynomial was fit to the vertical velocity (accounting for camera tilt) as a function of r, $V_X(r)$. $V_X(r)$ then allowed determination of the observation frequency of bubbles of each size class in the field of view to derive a multiple count correction for the flux (number of bubbles μm^{-1} radius s^{-1}), which was calculated as time-resolved. Where $V_x(r)$ varied significantly with time, an error is introduced since the algorithm uses a single $V_x(r)$, which is calculated from all bubbles measured. This error was estimated at 30% for pulsing plumes, which showed the largest variation in $V_x(r, t)$.

Bubble plumes can be characterized as major or minor, where major plumes are described by a power law and are formed by bubble fragmentation, and minor plumes are described by a Gaussian function (Leifer and Boles 2005). The bubble emission size distribution (Φ) is described by the radius (r), peak radius (R_p), and width (W^2) in Eq. 7 and in case of a major plume, Φ s expressed by a power law of r and with exponent (A) in Eq. 8.

$$\Phi \sim (r - R_P)^2 / W^2 \quad (1)$$

$$\Phi \sim r^A \quad (2)$$

For minor plumes, the radius of the peak of the Gaussian function, termed the mode, is determined solely by sediment grain size if the emission flux (*Q*) is below a critical value (Leifer and Culling 2010). For *Q* above the critical value, the mode also depends on *Q*.

The characteristic mode radius was determined from a least squares linear regression fit of a Gaussian function (or functions if multiple modes) using the MATLAB curve fitting tool. Integration of the emission size distribution over *r* at each time provides the time trend in total bubble volume and surface area as well as the rates of emissions of plume bubbles *Q* (mL s^{-1}) and surface area (*A*, cm^2 s^{-1}).

3.3.6 Methane incubation experiments

Incubation experiments were performed to study the survival of benthic methanotrophs after transportation into the water column. Before the experiments, 1 L serum flasks were cleaned with HCl (10%), rinsed with ultra-pure water, and autoclaved. Subsequently, they were equipped with planar oxygen-sensitive spot for optical oxygen meters (PreSens, Germany), which enables non-invasive oxygen measurements in samples. After installation of the sensor spots, the flasks were rinsed with ethanol and sterile ultra-pure water three times each, and closed with a specifically designed lid (Fig. 17). These lids had two ports each, which were closed gas tight with a septum and a stirring mechanism that was mounted onto the lid. After the Bubble Catchers were subsampled as described in section 3.2.1 (Fig. 13), 3× 500 mL of Bubble Catcher sampling water was added to the prepared 1 L laboratory flasks. For the incubations "Inc1" (RSV3) and "Inc2" (RSV4) “BC vent” sample water was used and for the control incubation "IncE" (RSE1) “BC engineered” sample water was used. Gas volume and bubbling time is noted in Table 2. The Bubble Catcher experiment RSV4 was solely conducted for the incubation experiments at a later date with 4.7 L gas being collected in 49 min. The incubation flasks were closed immediately and cooled until further processing in the laboratory.

In the laboratory, one incubation of each Bubble Catcher water sample was heated to 80 °C for one hour to inactivate any microorganisms. These samples were used as control. After cooling to room temperature, the two ports were used to flush the headspace of all samples with sterile air for 5 minutes while mixed at 210 rpm. Subsequently, 0.7 mL methane gas was applied to the incubations with a long needle inserted through the ports. In this way the

methane concentration in the incubation water was adjusted to a ~2 µmol L^{-1}. One incubation per Bubble catcher experiment (RSV1, RSE1) was performed for 7 days, while another sample and the control samples were incubated for 21 days. The incubation experiments from the Bubble Catcher experiment RSV4 were performed for 6 and 20 days, respectively. During the incubation oxygen levels were determined using the optical sensor spots. After the incubations were stopped, subsamples for MOB abundances (3.3.3.1) and methane oxidation (3.3.2) were taken and analyzed.

Fig. 17 | Methane incubation experiments. 1 L laboratory flasks with a specifically designed lid with two gas tight ports and a gentle stirring mechanism. Incubated at *in situ* temperature and 210 rpm.

3.3.7 Hydroacoustics

3.3.7.1 Seafloor mapping and gas flare detection

At the Blowout location, gas bubbles were detected (i) by water-column imaging using a fixed-installation, 50-kHz multibeam SB3050 with a 1.5° × 2° TX/RX aperture (L-3 ELAC Nautik GmbH, Kiel, Germany) and (ii) by the ROV, using a Kongsberg MS1000 sector scanning sonar. A detailed description of the latter method is provided in Schneider von Deimling (2017). CTD measurements were obtained for sound ray-tracing to calculate bathymetry, performed using MBSystems 5.4. The F180 attitude system was fully patch-tested and operated well within its specifications in recording data for roll, pitch, and heave. The data were tidally reduced with the built-in ocean tidal prediction model to obtain the final bathymetry. In addition to bathymetry sampling, the surveyed followed dedicated lines for water column imaging using the multibeam

echosounder. The entire mapping area was surveyed with increased receive gain to optimize the sensitivity for scatterers such as gas bubbles in the water column.

3.3.7.2 Current measurements

A 300-kHz RDI Workhorse ADCP (Teledyne Technologies, USA) was used to analyze water movement and determine the residual background current in the vicinity of the Blowout direction before water sampling. Water current direction and magnitude were tracked over 92 h from August 30 until September 3, 2016, based on a measurement ensemble consisting of 100 sub-pings every 10 min. There were 43 2-m-thick depth bins in the vertical, with midpoints ranging from 85.8 m depth to 1.8 m below the sea surface. Within each bin, the four beams of the ADCP tracked the water movement in the east-west, north-south, and vertical directions using the Doppler shift of pings backscattered off passive particles in the water column. The resulting velocities were analyzed using the T-TIDE package (Pawlowicz et al. 2002) in MATLAB. The current magnitude and direction was split into a tidal signal and a residual current for two depth ranges: near-surface water (1.8–20 m) and middle to bottom waters (35–85 m).

3.3.8 Gas flux measurements

The ROV's video system was used to quantify gas release at four different vent sites of the Blowout. Data from these measurements were then compared with data from a previous study, which had identified minor (~0.008–0.043 L s^{-1}), medium (~0.05–0.1 L s^{-1}), and major (>0.5 L s^{-1}) vents (Leifer 2015), to evaluate the changes in gas flow over time. During a gas capture experiment at a vent site, the bubbles were funneled into a gauged (2-L-increment scaling) acrylic glass cylinder (8 L volume) and gas fluxes were obtained by averaging over two increments. The average gas flux determined in these experiments represented a seafloor area of 30 × 30 cm (footprint of the sampling funnel) over a major vent.

3.3.9 Particle-tracking model

The MOB dispersion was investigated after their ejection from the Blowout into the water column by employing a Lagrangian particle-tracking model (Bauer et al. 2013, 2014) forced by the output of a numerical ocean model (GETM; Klingbeil and Burchard 2013). The ocean model has a horizontal resolution of 1 nautical mile (~1.85 km) and 42 adaptive, terrain-following vertical levels. A detailed description of the model and its validation is given in Gräwe et al. (2015). Hourly snapshots of the modelled velocity fields were stored to force the particle-

tracking model. In the particle-tracking model's application, bubble mechanics such as upwelling and enhanced bubble dissolution were neglected as >90% of the released methane, and most of the resuspended particles are trapped below the thermocline (Fig. 28; Leifer 2015; Schneider von Deimling et al. 2015). Besides, the data showed that in comparison with the background station the water body along the transects below the lower thermocline was influenced stronger by the transported MOB than the mixed layer (Fig. 29). Therefore, only a bulk-estimate of the MOB distribution in the depth region 35–90 m as a depth-integrated quantity was computed.

50,000 particles were released every 20 min between August 26 and September 8, 2016 (nearly 50 million particles in total). Their paths were tracked, and the particle locations converted into concentration fields by bin-counting. Each discrete particle represented a certain number of MOBs, based on a linear scaling factor to match the measured vertical MOB inventory below 35 m minus the background stations' inventory. To estimate the uncertainty (95% confidence intervals), a Bootstrapping method was applied. Instead of using all 8 sampling stations, only 7 samples were drawn and used to compute the scaling factor. By iterating over all possible permutations, the estimates were confined.

Various horizontal diffusivities mimicking the Brownian motion of individual MOB cells were tested, with the best agreement between the observed behavior of the MOB and the particle model achieved using a horizontal diffusivity of 8 $m^2 s^{-1}$.

4 Results

4.1 Parametrization of the bubble-mediated transport at the Coal Oil Point seep field

4.1.1 Distribution of vent sites in the study areas

The vent densities of Rostocker Seep (RS) ranged from 5 to 20 vents m^{-2}, and at IV Super Seep (SS) from 10 to about 700 vents m^{-2} (Fig. 18). The highest vent density, covering an area of ~16 m^2, was at IV Super Seep. Gas bubble emissions generally were more vigorous at IV Super Seep than at Rostocker Seep.

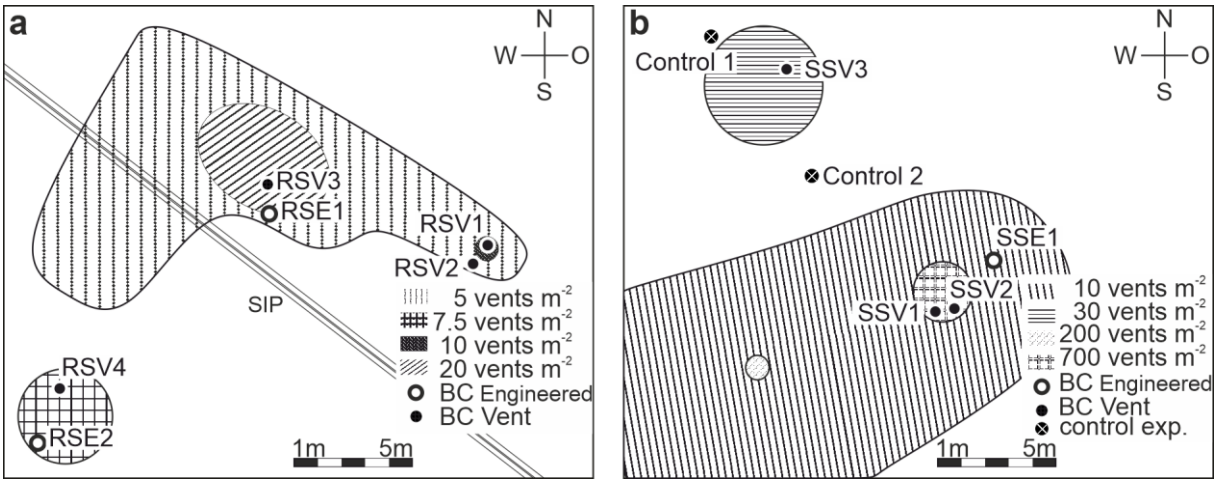

Fig. 18 | Rostocker and Isla Vista Super Seep areas. Schematic map of vent distribution and density at **a,** Rostocker Seep (RS) and **b,** the Isla Vista Super Seep (SS). Locations of the Bubble Catcher (BC) vent, engineered, and control experiments are marked. The double line illustrated in **a,** represents the two seawater intake pipes (SIP) that transport seawater from further offshore to the University of California, Santa Barbara campus.

4.1.2 Characterization of sediment and water column

The surface sediments at Rostocker Seep and IV Super Seep generally were dominated by a medium sand fraction but the two seeps differed in that IV Super Seep also was characterized by tar deposits in sediment cores and on the sediment surface. Methane sediment concentrations for both seep sites were in the millimolar range and increased with increasing sediment depth, from 0.05 mmol L^{-1} at the sediment surface (0-1.5 cm b.s.f. = centimeters below the seafloor) to 1.5 mmol L^{-1} at 10 cm b.s.f. (Fig. 19d). Total cell counts were consistent over the entire depth range (~ 1.5×10^9 cells cm^{-3}; Jordan et al. (2020), Supplementary Table S1), although MOB abundances as a percentage of total cell counts decreased from ~7% at the sediment surface (~ 8×10^7 cells cm^{-3}) to ~0.5% at 10.5 cm depth (Fig. 19e).

Water column temperature profiles taken over the course of the sampling campaign indicated the build up of a thermocline over several hours that then collapsed from mixing during the course of the day. Throughout the sampling campaign, bottom currents followed the coast, consistent with typical northern Santa Barbara Basin currents, which are driven by the Davidson Current (Leifer 2019). Water column turbidity changed on a daily basis, resulting in a visibility that ranged from <50 cm up to 10 m (reported by divers). The water in the vicinity of both seep sites was enriched in methane (Fig. 19a) which varied on a daily basis. Mean methane concentrations were consistently lower at Rostocker Seep than IV Super Seep by a factor of about two throughout the water column. At Rostocker Seep, MOx increased with increasing water depth, with the highest rate occurring in the bottom waters (min. 0.1 nmol L^{-1} d^{-1} and max. 27.4 nmol L^{-1} d^{-1}, (Fig. 19b). By contrast, at IV Super Seep, the highest oxidation rate was measured in intermediate waters (min. 0.7 nmol L^{-1} d^{-1}, max. 15 $nmol^{-1}$ d^{-1}, (Fig. 19b). Total cell numbers were consistent throughout the water column and seep sites (~2 × 10^6 cells mL^{-1}; Jordan et al. (2020), Supplementary Table S2), with MOB abundances of ~4 × 10^3cells mL^{-1} (0.1–0.2% of DAPI-stained cells) at both seep sites (Fig. 19c). Total cell numbers were approximately three orders of magnitude lower in the water column than in the sediment and MOB abundances approximately four orders of magnitude lower. Cell-specific methane oxidation rates ranged from 7.4 × 10^{-4} fmol L^{-1} h^{-1} to 1.6 × 10^{-2} fmol L^{-1} h^{-1}.

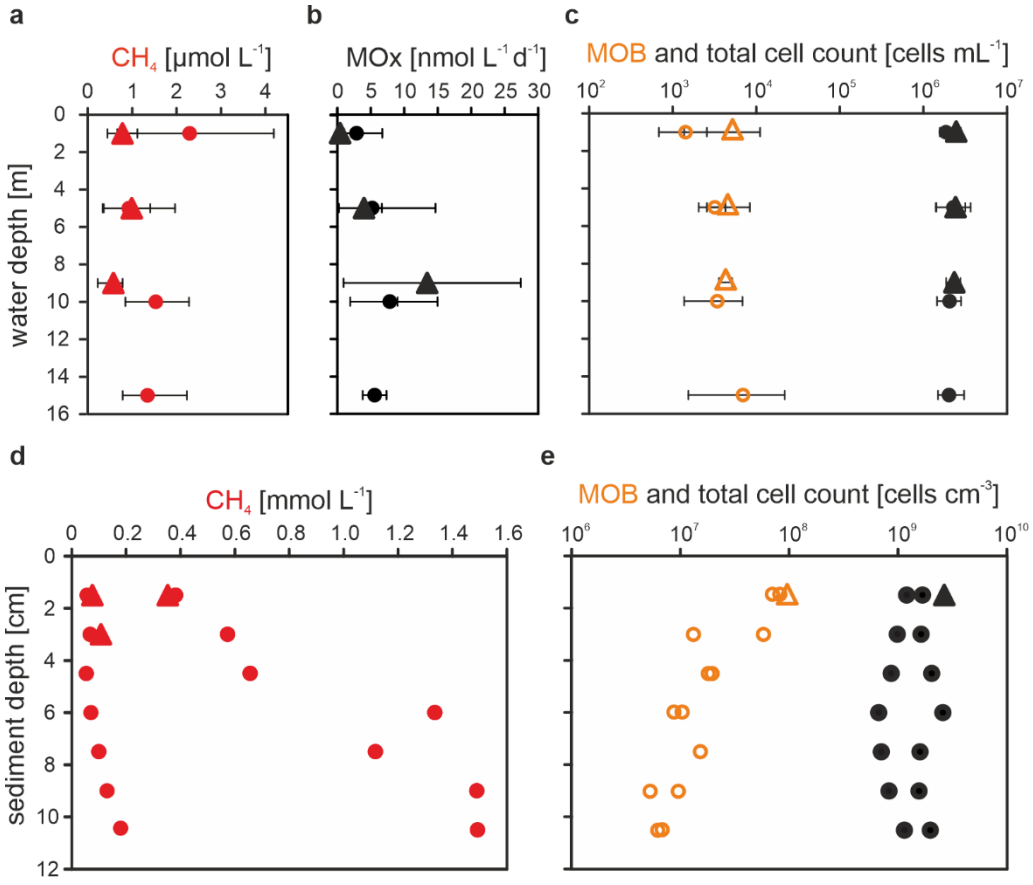

Fig. 19 | Methane related biogeochemical parameters. Depth profiles of parameters determined in the water column **a**–**c,** and in the sediment **d**, **e**, at the Rostocker Seep (triangle) and the IV Super Seep (circles). **a**, mean water column methane concentration, **b**, mean water column methane oxidation (MOx), **c**, abundance of methane-oxidizing bacteria (MOB, open orange symbols) and total cells (black) in the water column, **d**, sediment methane concentration, **e**, abundance of MOB (open orange symbols) and total cells (filled black) in the sediment. The bars in **a–c** indicate the range of values between three fieldwork days.

4.1.3 Bubble size distribution

A Bubble Measuring System collected seep bubble videos for the Rostocker Seep and IV Super Seep where the Bubble Catcher samples were taken. Analysis of the bubble size distribution (the number of bubbles per second per radius increment passing through a plane) for a Rostocker Seep vent revealed two emissions modes at *r*=1,660 and 2,750 µm (RSV1, Fig. 20a). This seep was well described as by Gaussian functions, e.g., a minor seep with formation not resulting from bubble fragmentation (Leifer and Boles 2005). Emissions were as a bubble pulse of bubbles that lasted ~3.5 s and comprised 774 bubble images. The volumetric gas flow (*Q*) was 1.0 mL s^{-1} and the bubble surface area flux (*A*) was 10.9 cm^2 s^{-1}, dominated by the larger mode.

Analysis of 5,236 bubble images from a second, smaller, minor Rostocker Seep vent (RSV2, Fig. 20b) identified a dominant mode at r=1,505 µm and a second much smaller mode at

r=1,710 µm. Three complete pulses spanning 20 s were analyzed, with the second pulse lasting ~5 s. Similar to the other pulsing vent at Rostocker Seep, the onset of a bubble pulse at the second vent was accompanied by larger bubbles. *Q* was 0.29 mL s^{-1} and *A* was 4.9 cm^2 s^{-1}.

A small minor vent at IV Super Seep (SSV1, Fig. 20c) was analyzed based on 7,850 bubble images and found bubbles spanning 400 < *r* < 8,000 µm with a dominant mode at *r* = 1,540 µm and *Q* = 0.16 mL s^{-1}, and *A* = 3.0 cm^2 s^{-1}.

The only major vent (where the bubble size distribution is well described by a power law and results from bubble fragmentation) was from the main area of IV Super Seep (SSV2, Fig. 20d); all other vents were minor (Fig. 20a-c). At the IV Super Seep main vent (SSV2), 2,404 bubbles spanning 500–2,600 µm radius were analyzed (Fig. 20d). *Q* was 1.3 mL s^{-1} per vent and *A* was 22.7 cm^2 s^{-1} per vent. *Q* varied by a factor of ~3 on a ~2 s timescale (Fig. 21). The dominant emission mode was *r*~1,530 µm, with a second mode at *r*~2,270 µm.

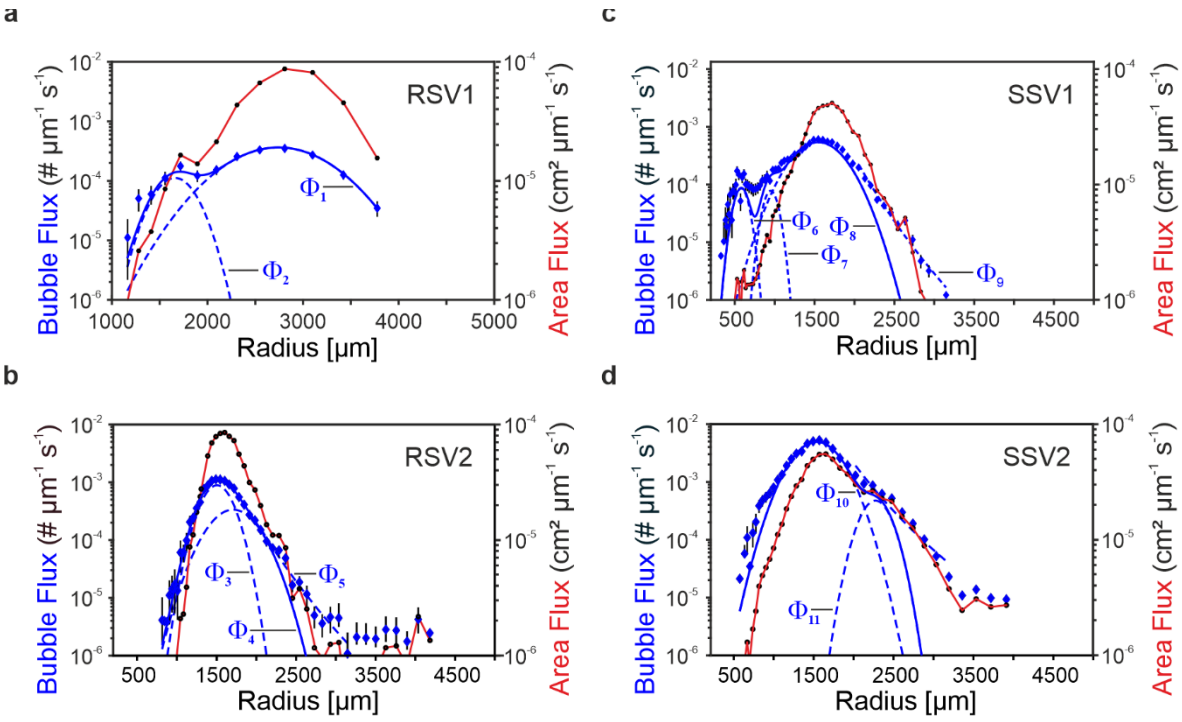

Fig. 20 | Bubble size distribution. Bubble emission size distribution (Φ) for bubbles crossing an arbitrary height above the seabed per second per unit radius *(r)*, for the four Bubble Catcher and BMS studied vents: **a**, **b**, Rostocker Seep, **c**, **d**, IV Super Seep. Emission modes determined by least-squares linear-regressions, fit equations Φ1–11 can be found in Table 5. Also shown is the bubble surface area flux versus *r*.

The *A/Q* ratios of three of the vents (SSV1, RSV2, SSV2) were similar, ~18 cm^{-1} (Table 2), which was expected given the similarity in the dominant modes of the vents. Emissions were far less steady at the minor than at the major vent and even ceased for ~1 s in the 40 s analyzed video, which also showed clear pulsing. Pulses were associated with larger bubbles. The dominant mode similarity with the major vent indicates that grain size (mid sand fraction at all sampling sites) controlled the emissions and that *Q* was non-critical (Leifer and Culling 2010; Vazquez et al. 2010) for all vents. For non-critical flow, *Q* increases the number of bubbles but the size remains the same, for critical flow, the bubble size increases with *Q*. At the minor vent, much less important modes at 580 and 960 µm, corresponding to ~1/3 and 2/3 of the major mode, were detected.

Table 5 | Bubble size fit equations. Overview of parameter values describing the fit equation of the bubble emission size distribution (Φ), peak radius (R_p), width (W^2), and exponent (A). For the corresponding equation see section 3.3.5.

Seep	Fit Number (Φ)	R_P [µm]	W [µm]	A
RSV1	1	2744	672	
RSV1	2	1660	268	
RSV2	3	1505	240	
RSV2	4	1709	380	
RSV2	5			-10.7
SSV1	6	580	118	
SSV1	7	950	120	
SSV1	8	1540	410	
SSV1	9			-8.1
SSV2	10	1531	372	
SSV2	11	2271	234	

The BMS data from the IV Super Seep's major vent showed an upwelling flow (V_{up}) of ~4 cm s^{-1}, which agreed well with the field data-derived relationship between V_{up} and *Q* in Leifer (2010), in which V_{up}~4 cm s^{-1} corresponded to *Q*~1.2 mL s^{-1}. For the IV Super Seep minor vent, V_{up} ~1 cm s^{-1}, in good agreement with the V_{up} of ~1.05 cm s^{-1} as reported previously (Leifer 2010), corresponds to *Q*~1.6 mL s^{-1}. Interestingly, $V_X(r)$ for the main vent followed the shape of $V_{up}(r)$ for dirty (coated by oil or other surface-active substances) bubbles whereas V_x for the minor vent followed $V_{up}(r)$ for clean bubbles.

For Rostocker Seep, V_x suggested clean bubbles. V_{up} was quite small, roughly 0.25 cm s^{-1} but was challenging to derive for the pulses, as V_x varied strongly with time, growing nearly an

order of magnitude larger in the middle of the pulse. This introduced a ~30% error into the multiple count correction due to the variation in V_x and thus in Q and A, but not into A/Q. As such, there was little change in the A/Q ratio over time, which allowed its application to the BC volumetric fluxes to derive the Bubble Catcher area fluxes, even though BMS and BC measurements were not concurrent.

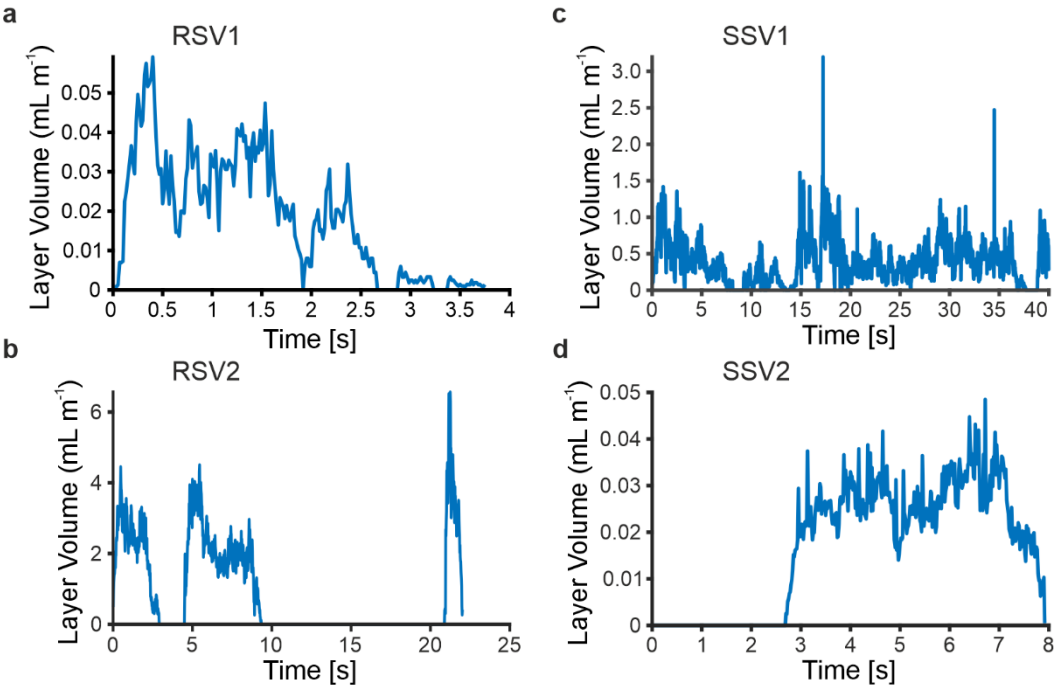

Fig. 21 | Layer volume flux. The bubble volume in a 1-cm-thick layer for the four Bubble Catcher and BMS studied vents: **a**, **b**, Rostocker Seep, **c**, **d**, IV Super Seep. Vent name labelled on figure.

4.1.4 Implications of seepage parameters on transport efficiency

The bubble transport process was studied using the Bubble Catcher by sampling gas bubbles escaping (1) a natural vent ("BC vent") and (2) an engineered gas outlet without any sediment contact ("BC engineered"). The volumetric flow of the examined vents ranged from 0.07 (±8%) to 0.73 (±2%) mL gas s^{-1} at Rostocker Seep and from 0.04 (±2%) to 2.20 (±3%) mL gas s^{-1} at IV Super Seep (Table 2). The number of transported cells was normalized for time (Fig. 22a), volume of emitted gas (Fig. 22b), transported bubble surface area (Fig. 22c), and seabed seepage area (Fig. 22d) to determine the parameters influencing in the bubble-mediated transport of benthic MOB. MOB were transported in all "BC vent" experiments. The total number of transported cells at the individual vents per time ranged from 1.4×10^4 to 1.3×10^5 cells s^{-1}. Transported MOB per vent ranged from 4.1×10^2 to 7.8×10^3 cells s^{-1} (Fig.

22a). The number of transported MOB and total cells per milliliter of emitted gas (Fig. **22**b) decreased with increasing volumetric flow, following an inverse trend that indicated the transport of a 100 times more MOB (2.27×10^4 cells mL_{gas}^{-1}) at the lowest volumetric gas flow (0.07 mL s^{-1}) than at the maximum investigated flow (2.2 mL s^{-1}, 1.9×10^2 cells mL_{gas}^{-1}). Total cell counts showed a similar trend, with an initial count of 9.96×10^5 cells mL_{gas}^{-1} at 0.07 mL s^{-1} that declined to 6.2×10^3 cells mL_{gas}^{-1} at 2.20 mL s^{-1}. Cell transport per unit surface area followed the same inverse trend, ranging from 2.2×10^3 MOB cm^{-2} (RSV1) to 1.0×10^1 MOB cm^{-2} (SSV2) at a transported bubble surface area (A) of 0.8 cm^2 s^{-1} and 39.6 cm^2 s^{-1}, respectively (Fig. 22c). The distribution pattern of the total cell counts was essentially identical, with an initial count of 9.4 $x10^4$ cells cm^{-2} at 0.8 cm^2 s^{-1} that decreased to 3.5×10^2 cells cm^{-2} at 39.6 cm^2 s^{-1}. Based on the vents per square meter at the respective study sites, the largest number of MOB was transported by IV Super Seep bubbles, where the vent density was highest, up to 700 vent orifices per m^2 (1.2×10^{11} cells m^{-2} d^{-1}; Fig. 22d), and the lowest number at Rostocker Seep, with only 5 vents per m^2 (7.1×10^8 cells m^{-2} d^{-1}) – a difference of three orders of magnitude. Note that the observed gas flow spanned over two orders of magnitude (Fig. 22).

DAPI analysis showed that the total cell abundance in the “BC engineered” experiments was ~3×10^3 cells mL^{-1}, such that mean cell counts in the “BC vent” experiments were ~17 (SS) to 94 (RS) times higher. MOB abundance in the ”BC vent” was 24 (SS) to 62 (RS) times higher than in the controls (4×10^1 cells mL^{-1}; Jordan et al. (2020), Supplementary Table S4). In the “BC engineered” experiments at Rostocker Seep, cell numbers of 8.0×10^5 cells mL_{gas}^{-1} and 4×10^3 MOB cells mL_{gas}^{-1} were determined, whereas at IV Super Seep only 1×10^4 cells mL_{gas}^{-1} and 4×10^2 MOB mL_{gas}^{-1} were transported into the Bubble Catcher. A comparison of the “BC engineered” and “BC vent” experiments indicated that the mean number of total transported cells in the “BC vent” experiments was two (RS) to eight (SS) times higher and four (RS) to six (SS) times higher for MOB.

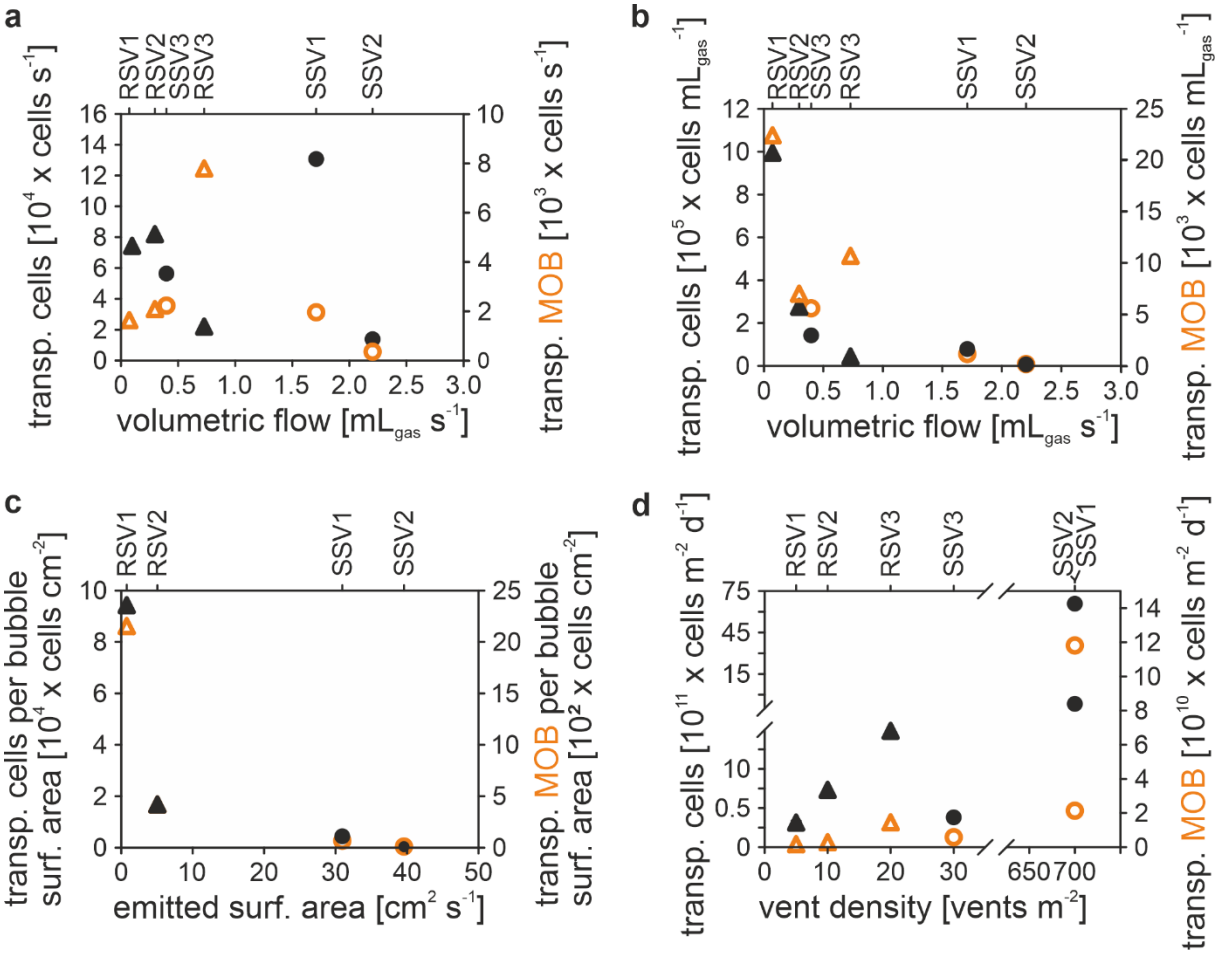

Fig. 22 | Cell transportation. Transported total cells (black) and MOB (orange) at Rostocker Seep (triangle) and IV Super Seep (circles) normalized to **a,** time and **b,** emitted gas as a function of volumetric flow, **c,** bubble surface area as a function of emitted surface area, **d**, transported cells per square meter and day versus vent density.

4.2 Identification of transported methanotrophs at the Coal Oil Point seep field and their survival in the water column

4.2.1 Comparison of transported methanotrophs with benthic and pelagic methanotrophic communities

To identify transported MOB, the recovered OTUs and ASVs were searched with respect to previously known methanotrophic families. All extracted OTUs were mostly associated with unclassified methanotrophic genera (e.g., unclassified *Methylomonaceae,* Marine Methylotrophic Group 2, see Jordan et al. (2020), Supplementary Table S5). OTUs closely related to known MOB have a high probability of being methanotrophic bacteria and hereafter referred to as methanotrophic OTUs. Twenty of 40 detected methanotrophic genera belonging to the family *Methylomonaceae* were selected for visualization (Fig. 23a). The remaining 20 OTUs were detected only in the sediment. The heat map reveals that some methanotrophic OTUs were detected in all sample groups whereas others had a divergent distribution pattern.

Relative abundances based on methanotrophic reads were highest in sediment samples, lower in the “BC vent” sample, and lowest in samples taken from the “BC engineered” experiments and the water column. The highest relative abundance of single methanotrophic OTUs was 0.1–1%. In addition to the family *Methylomonaceae*, six OTUs assigned to the genus *Cycloclasticus* (Fig. 23c) were identified, including four OTUs in the sediment, “BC vent,” and water column samples. The maximum relative OTU abundance related to *Cycloclasticus* was ~1%.

From the particulate methane monooxygenase *(pmoA)* analysis, 650 ASVs were assigned, of which 42 were found in the Bubble Catcher and in sediments (Fig. 23b). The patterns for *pmoA* (Fig. 23b) and 16S-rRNA genes analysis (Fig. 23a) were similar, with nine ASVs detected in all sample groups and 15 present in the sediment, “BC vent” experiments, and water columns. Of the 36 ASVs belonging to the family *Methylomonaceae*, 29 could be assigned to *Methyloglobulus morosus* and three to *Methylomicrobium kenyense*. One ASV was associated with the family *Methylocystaceae*, belonging to the order *Rhizobiales*, and four ASVs were assigned as MOB-like.

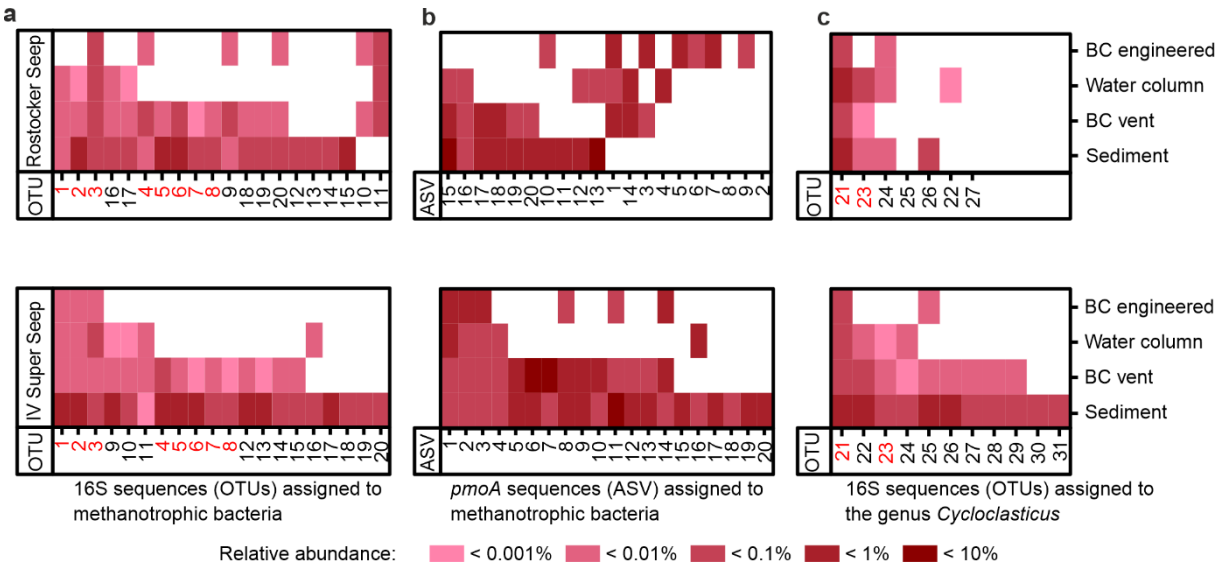

Fig. 23 | Phylogenetic analysis of MOB and *Cycloclasticus*. Relative abundance of **a,** selected 16S rRNA gene sequences (OTUs) assigned to the methanotrophic family *Methylomonaceae* and **b,** selected *pmoA* sequences (ASVs), and **c**, OTUs assigned to the genus *Cycloclasticus* in the different sampling groups obtained from the Rostocker Seep and IV Super Seep sites. Note that the OTUs marked in red in **a**, **c** had similar distribution patterns at the two seep sites. For taxonomic information on the OTUs and ASVs, see Jordan et al. (2020), Supplementary Tables S5 and S6, respectively.

4.2.2 Methane incubation experiments

Incubation experiments with “BC vent" (Inc1, Inc2) and “BC engineered” (IncE) sample water from the Rostocker Seep site showed an increase in the total cell numbers after one-week incubation time (~24–77 times) as well as an increase of the MOB cell numbers (~454–1408 times). However, after three weeks the total (~7–35 times) and MOB (~172–375 times) cell numbers declined but were still elevated when compared with the respective starting cell numbers (Fig. 24). In the incubation experiments with "BC engineered" sample water, cell abundance increased only slightly over the incubation runtime when compared with the mean values obtained in the “BC vent” experiments (7 days: total 31 times; MOB 161 times; 21 days: total ~14 times; MOB ~70 times; Fig. 24). In control experiments with pasteurized sample water, total cell numbers did not change or decrease (~0.4–1.1) and MOB cell numbers (~1–18 times) only slightly increased with regard to the start of the incubations. Oxygen was present at all times during the experiments and did not fall below 270 µmol L^{-1}. Tracer experiments with ^{3}H-methane showed methane oxidation during the three weeks of incubation, except for heat-treated incubations (Table 6).

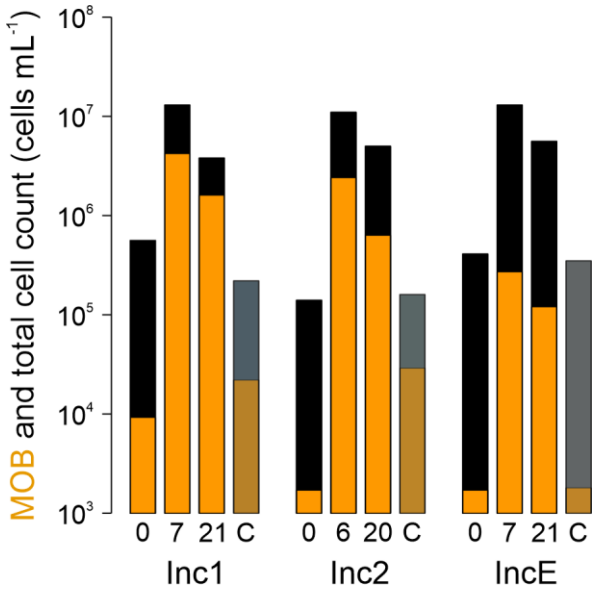

Fig. 24 | Total cell and MOB counts of incubation experiments from Bubble Catcher sample water. The incubations "Inc1" (RSV3) and "Inc2" (RSV4) were subsampled from “BC vent” sample water, whiles the control incubation “IncE” (RSE1) was derived from “BC engineered” sample water.

Table 6 | Overview of incubation experiments' parameters. Listed are the incubations respective incubation time, total cell numbers (DAPI), methane-oxidizing bacteria (MOB) abundance, and methane oxidation first-order rate constant (k').

name	time [d]	DAPI [cells mL^{-1}_{sample}]	MOB [cells mL^{-1}_{sample}]	k'
Inc1 t0	0	5.6E+05	9.2E+03	0.00037
Inc1 t1	7	1.3E+07	4.2E+06	0.00255
Inc1 t3	21	3.8E+06	1.6E+06	0.00038
Inc1 80C t3	21	2.2E+05	2.2E+04	0.00004
Inc2 t0	0	1.4E+05	1.7E+03	<LOD
Inc2 t1	6	1.1E+07	2.4E+06	0.00004
Inc2 t3	20	5.0E+06	6.3E+05	0.00060
Inc2 80C t3	20	1.6E+05	2.9E+04	N.A.
IncE t0	0	4.1E+05	1.7E+03	0.00080
IncE t1	7	1.3E+07	2.7E+05	0.00003
IncE t3	21	5.6E+06	1.2E+05	0.00051
IncE 80C t3	21	3.5E+05	1.8E+03	<LOD

4.3 Assessment of the contribution of bentho-pelagic transport processes to the local methane sink at North Sea blowout well 22/4b

4.3.1 Gas seepage activity

During the expedition, the first step was to investigate the gas release activity within the Blowout region. By daylight, the typical surface patch above the Blowout was visible; its diameter was ~10 m Fig. 6a). Four major vents were detected in the Blowout's crater by the ROV (Fig. 25b and Jordan et al. 2021, Movie S2, S3) and were active during all dives. Countless smaller vents were also detected (Jordan et al. 2021, Movie S2). The four major vents formed three bubble plumes in the crater (Schneider von Deimling 2017) because two of the vents were only 0.1–0.2 m apart such that their plumes merged (Schneider von Deimling 2016; Jordan et al. 2021, Movie S3). Thus all but one of the major vents reported by Leifer (2015) and Schneider von Deimling et al. (2015, Video S3) were located. At ~25 m above the crater's bottom, bubbles released from different sources merged into a single rising gas mega-plume with a diameter of ~10 m (Schneider von Deimling 2017; Jordan et al. 2021, Movie S2). The hydroacoustic snapshot flare image showed that the gas-bubble release from the Blowout crater created an extensive bubble plume divided into one part that stays below the lower thermocline (located in 35 m water depth, Jordan et al. 2021, Movie S2) and the other breaking through it (Fig. 25b), with a maximum diameter of ~19 m. As seen in the depth profile (Fig.

25a), the water body above the Blowout was well stratified, forming an upper (~20 m) and a lower (~35 m) thermocline.

Additional multibeam surveys in the Blowout perimeter revealed eight additional gas vents characterized by single bubble chains but, in contrast to the Blowout, no bubble plume formation. Furthermore, vents southwest and one vent east and another west of the Blowout (Fig. 25) were identified. In addition to these single vents, a smaller, previously observed crater located southeast of the Blowout was detected. In an earlier study the emissions flux from this southeast crater was estimated to be significantly less than that of the Blowout; however, only an estimate was possible because the crater was too small to be explored using a ROV (Leifer and Judd 2015). Video footage from the crater's rim suggested that the volume of gas emitted from this crater was only a small fraction of that of the Blowout (Wilson et al. 2015). Nonetheless, even if the crater's total emission contributed only 1% of the Blowout's plume, the resulting plume would still classify as a mega plume (Leifer and Judd 2015). In this case, total emissions would range between 0.9 and 1.5 L s^{-1}, a rate equal to that of one of the four major vents of the Blowout. Given the minor gas emissions, the gas release of the single vents and the small south-eastern crater were excluded from the Lagrangian particle-tracking model.

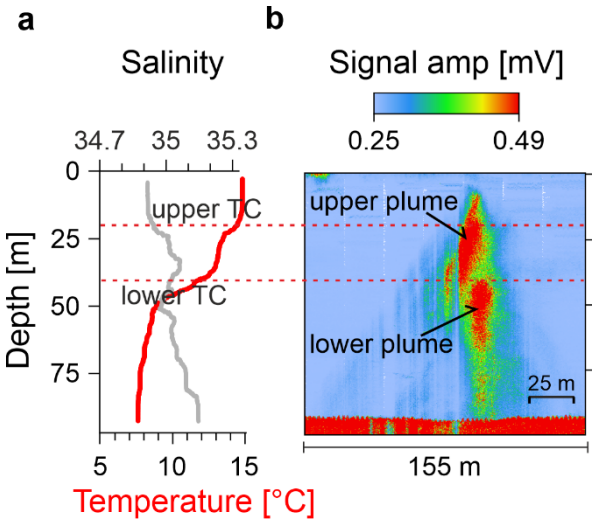

Fig. 25 | Temperature and salinity profile and water column flare image. a, Temperature (red) and salinity (grey) profiles of the water column above the Blowout; **b**, echogram multibeam view of the Blowout (full width: 155 m). Signal amplitudes (Signal amp) are mapped with a linear color bar. A lower plume is visible until ~35 m water depth while an upper plume reaches the sea surface. The cruising speed during hydroacoustic data recording was ~0.5 kn.

In addition to acoustically based observations of the plume, the Blowout's gas flux was analyzed in gas-capture experiments and using the ROV's video system. The gas flux ranged from 0.470 to 0.729 L s^{-1} (Table 7).

Table 7 | Gas flux experiments. Results of the gas-capture experiments conducted at the Blowout. Gas fluxes were determined for the major vent classes described by Leifer (2015). The displayed fluxes represent a 30 × 30 cm seafloor area covering one of the Blowout's major gas vents.

Experiment	Vent class	Mean flux (l s^{-1})	Number of experiments	Deviation (%)
1	major	0.729	2	10.0
2	major	0.470	2	3.4

4.3.2 Water mass movement

Measurements of the water mass showed a northward residual current (2.5–10 cm s^{-1}) of sub-thermocline waters (35–85 m water depth) over the entire ADCP run time, while the surface waters circled in a northeastern direction (Fig. 26). Given the flat bathymetry of this area, one can expect these currents to be representative of the entire survey area. The thermocline decoupled the surface water (upper 20 m) from the lower part of the water column. This decoupling was also apparent from the difference in the current directions (Fig. 26). The averaged residual current speed was 9 cm s^{-1} below the thermocline and 5 cm s^{-1} above it. During the campaign, the tidal excursions were 3.7 km below and 4.6 km above the thermocline, based on the ADCP data.

The ocean model performed well based on a comparison of its results with the field observations, with the predicted currents below the thermocline similar in magnitude and direction to those determined by the field ADCP measurements (Fig. 26). However, the model underestimated the current speeds in the surface water and the modelled current direction deviated from the actual one by 5° to the east.

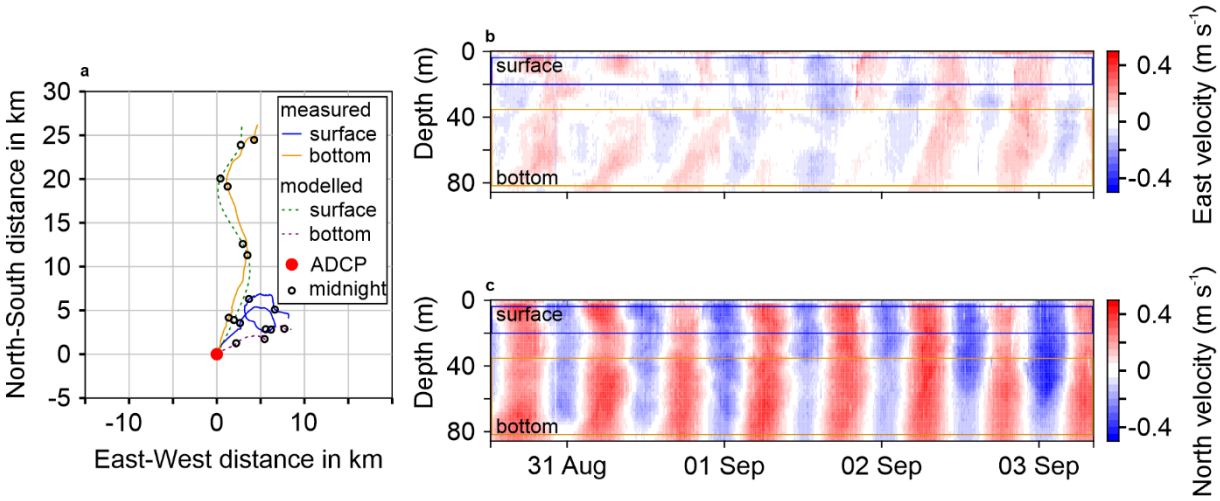

Fig. 26 | Residual currents. a, Comparison of the measured (solid lines) and modelled (dashed lines) residual current for the surface water (4–20 m water depth) and the sub-thermocline water (35–90 m water depth) from August 30, 2016, 11:35 UTC until September 3, 2016, 8:32 UTC, depicted using a progressive vector plot. The starting point is the position of the ADCP (red circle). The open black circles represent midnight (UTC). **b**, **c**, Water mass current direction and velocity over time. **b**, East velocity and **c**, north velocity over time (92 h total) and water depth obtained from ADCP measurements. The tides are clearly visible as alternating vertical bands, especially in panel **c**, as the tidal excursions in the north-south direction were more pronounced than in the east-west direction. The residual bottom current (35–85 m) towards the north can be seen as stronger northwards (red) than southwards (blue) bands. The surface layer (4–20 m) above the upper thermocline, which is visible as a discontinuity in the vertical bands just above 20 m depth, was also influenced by wind and had stronger east-west movement resulting in a more circular than rectilinear movement

4.3.3 Pelagic methane-related biogeochemistry

According to the depth profiles above the Blowout (station BC), both the maximum methane concentration (50 m, ~112 nmol L^{-1}) and the maximum methane oxidation rate (35 m, 0.6 nmol L^{-1} d^{-1}) occurred below the thermocline, followed by a slow decline of both with depth (Fig. 27a). MOB abundance changed only slightly from the surface down to 65 m (1.5 ± 0.23 × 10^8 cells L^{-1}), with an outlier at 50 m (2.5 ± 0.12 × 10^7 cells L^{-1}), and then decreased to 2.5 ± 0.03 × 10^7 cells L^{-1} at ~93 m. The ROV was used to collect two water samples within the Blowout. The first was taken 0.5 m above one of the major vents and included ~0.25 g of suspended sandy sediment L^{-1}. MOB abundance in this sample was 2.2% (2.2 × 10^7 MOB cells L^{-1}) of the total cell counts. The second sample was taken adjacent to the first sample and 0.5 m next to the major vent. MOB cell abundance in this sample was ~9.7% (7.9 × 10^7 MOB cells L^{-1}) of the total cell counts. At the background station (BG), the methane concentration was low over the first ~35 m (<5 nmol L^{-1}, Fig. 27b) but then increased slightly with depth (from ~31 nmol L^{-1} to 64 nmol L^{-1}, Fig. 27b) down to 80 m, followed by a steep increase towards the bottom (199 nmol L^{-1}, 95 m). Methane oxidation rates mostly followed methane concentrations (0.004–1.65 nmol L^{-1} d^{-1}) except for the higher rate at

10 m (0.89 nmol L^{-1} d^{-}). Methanotrophs abundance was highest above the thermocline (6.9 ± 0.25 × 10^7), declined with depth below the thermocline to 6.6 ± 0.19 × 10^7 cells L^{-1}, and reached a minimum of ~2.8 ± 0.04 × 10^6 cells L^{-1} at 95 m.

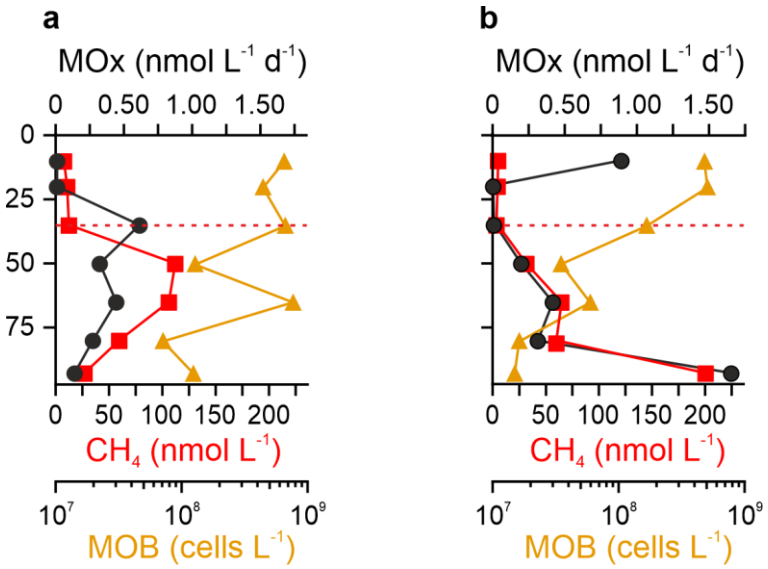

Fig. 27 | Depth profiles of methane related parameters above the Blowout crater and the background station. Methane concentration (red squares), methane oxidation (MOx, black circles), and the abundance of methane-oxidizing bacteria (MOB; orange triangles): **a**, at the Blowout station and **b**, at the background station. The red dotted line represents the lower thermocline at ~35 m.

The sections displayed in Fig. 28 show an overall increase in the methane concentration, MOB abundance, and the methane oxidation rate from the upcurrent-located IN transect (Fig. 28b, d, f) to the downcurrent-located OUT transect (Fig. 28a, c, e). At the IN transect (Fig. 28b), methane concentrations were generally <75 nmol, except at I3 (80 m, ~154 nmol L^{-1}) and I1 (90 m, ~1063 nmol L^{-1}). The latter station was close to a natural seep cluster (Fig. 28). After passing the Blowout, the sub-thermocline water mass along the OUT transect became enriched in methane, with concentrations rarely dropping below 100 nmol L^{-1} (Fig. 28a). At two OUT stations, elevated methane concentrations were detected in and above the thermocline, at 35 m (O4, ~195 nmol L^{-1}) and 20 m depth (O4, 467 nmol L^{-1}; O5, 307 nmol), respectively. However, the transects did not cover the whole methane plume, as the vertical inventories did not include background concentrations. MOB cell concentrations were elevated in the surface water at both transects, similar to the concentrations at the crater and background station, with higher concentration in the OUT transect (Fig. 28c: 1.3 ± 0.01 × 10^7 to 2.3 ± 0.08 × 10^8 cells L^{-1}; Fig. 28d: 1.6 ± 0.02 × 10^7 to 1.2 ± 0.02 × 10^8 cells L^{-1}), especially at its central station (O3). MOB cells were highly enriched below the thermocline in the OUT transect (O3 35 m, 5.3 ± 0.15 × 10^8 cells L^{-1}). In general, the methane oxidation rates followed the methane

concentration distribution and were low in the IN transect (0.004–4.65 nmol L^{-1} d^{-1}), with a median of 0.11 nmol L^{-1} d^{-1}, but higher after passing the Blowout (0.0002–2.13 nmol L^{-1} d^{-1}; Fig. 28e, f), with a median of 0.31 nmol L^{-1} d^{-1}.

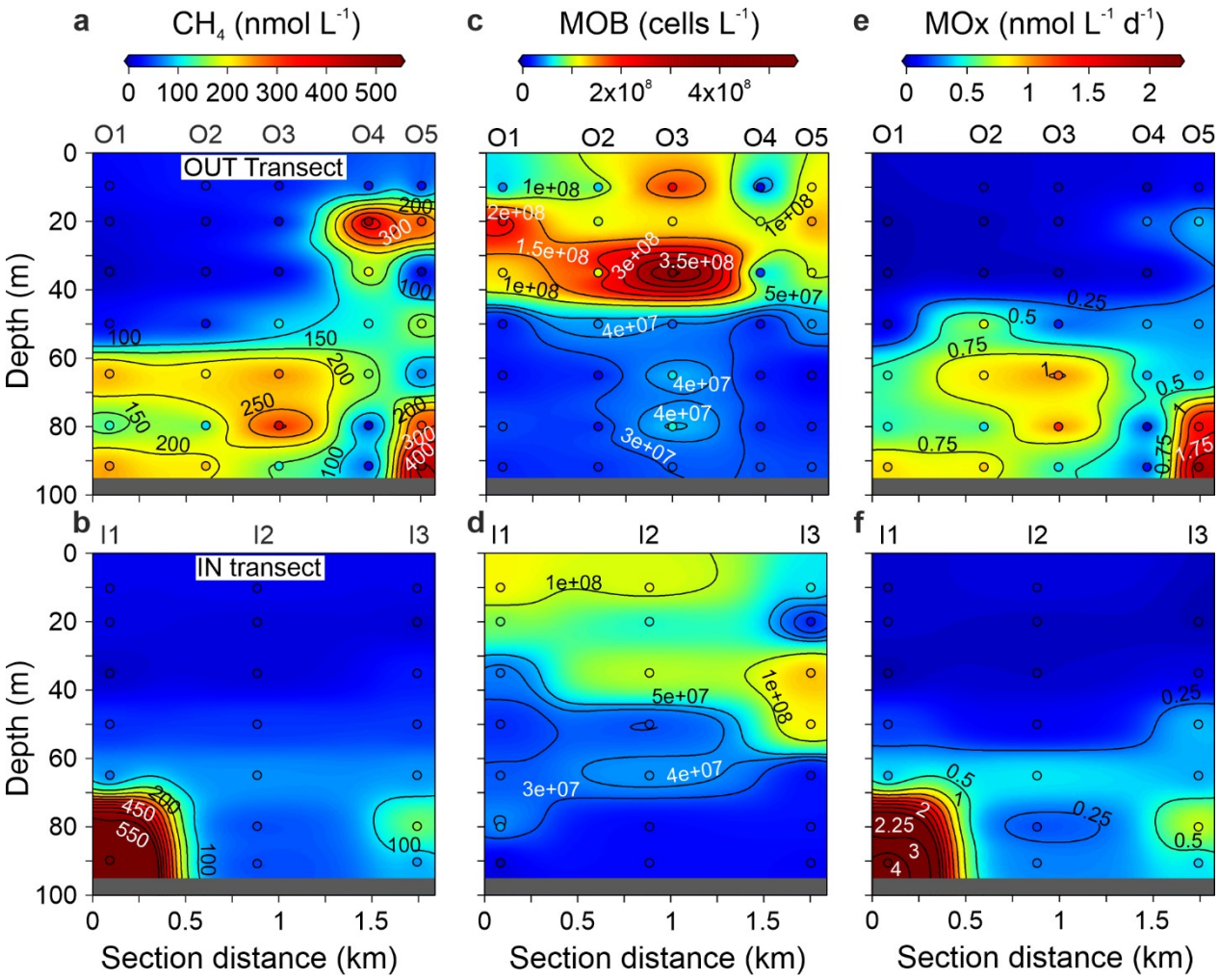

Fig. 28 | Methane-related biogeochemical parameters. Sections of methane-related biogeochemical parameters along the IN and OUT transects. **a**, **c**, **e**, The sections of the OUT transect with five stations (west to east O1–O5) and **b**, **d**, **f**, the IN transect with three stations (west to east I1–I3) are depicted. **a**, **b**, The water-column methane concentration, **c**, **d**, abundance of aerobic methane-oxidizing bacteria (MOB), and **e**, **f**, methane oxidation rates (MOx) are shown. The parameters are displayed over depth and along the transect distance. The grey area at the bottom of each graph indicates the seafloor.

To determine the water mass most strongly affected by the transport of benthic MOB into the water column, the MOB cell abundance in the two transects were compared with the MOB cell distribution at the background site. The enrichment of MOB cells in the two transects relative to the background station was calculated by dividing the average MOB cell number per transect and depth by the MOB cell number measured at the background station (Eq. 9):

$$\mathrm{x-fold\ MOB\ cell\ increase} = \mathrm{MOB\ cells_{IN\ or\ OUT}} \,/\, \mathrm{MOB\ cells_{RF}} \quad (9)$$

The results showed that MOB cell abundance was only slightly elevated in the mixed layer (0.8–2 – fold) but highly elevated below the thermocline (2.2–9.8 – fold; Fig. 29). This pointed to the sub-thermocline water as the water mass most strongly influenced by the released methane and the ejection of benthic MOB cells from the Blowout. To concentrate the assessment of the impact of MOB cell transport on methane biogeochemistry in the Blowout region, the further focus lays on this lower part of the water column (35–90 m), where the clear northward-oriented residual current direction contrasted with the more complex current pattern of the surface waters.

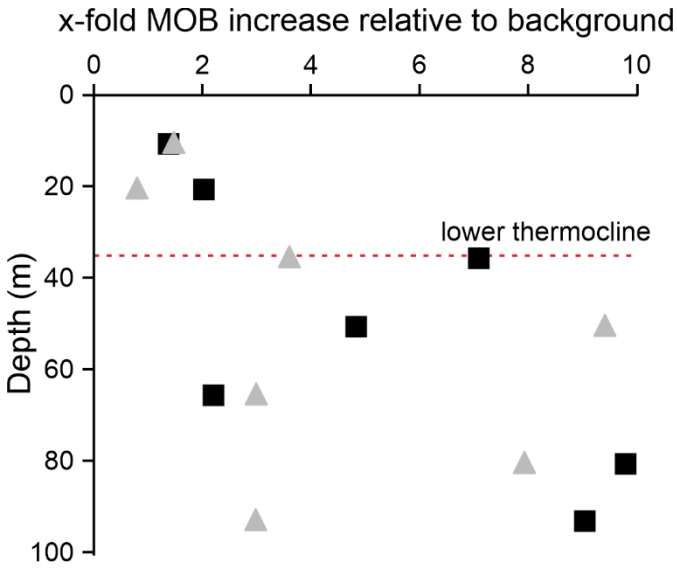

Fig. 29 | Comparison of MOB abundance between background site and transects. Horizontally averaged profiles of the methane-oxidizing bacteria (MOB) cell numbers for the IN (triangle) and OUT (square) per transects relative to the background station (BG): x-fold MOB increase = MOB cells$_{IN\ or\ OUT}$ / MOB cells$_{BG}$. The red dotted line represents the lower thermocline at ~35 m.

The depth-integrated and cross-sectional MOB inventories reported in the following were calculated using the trapezoid method (Schmale et al. 2012b). Inventories were plotted as a function of distance along the transects from west to east (Fig. 30). Both the depth-integrated methane concentration and MOB cell abundance were calculated from the dataset obtained at the background station (dotted lines in Fig. 30a, b). These inventories underlined the higher methane concentration and higher MOB cell abundances in the OUT than in the IN transect (Fig. 30). The cross-sectional inventories of methane showed a ~1.9-fold increase from the IN (~7.3 mol m^{-1}) to the OUT (~14 mol m^{-1}) transect, with the greatest difference at the central station (~4.4-fold). Similarly, the cross-sectional inventories of MOB cells showed a ~1.3-fold

increase across the two transects (from ~3.7 ± 0.18 × 10^{15} cells m^{-1} to ~5 ± 0.27 × 10^{15} cells m^{-1}), with the greatest difference again occurring at the central station. The vertical inventory of methane oxidation rates followed the methane concentration, with an increase of 1.5-fold from the IN (0.03 mol m^{-2} d^{-1}) to the OUT (0.05 mol m^{-2} d^{-1}) transect. Oxidation rates were highest at the central station (O3) and at the most eastern station (O5), with ~0.04 mmol m^{-2} d^{-1} determined at both.

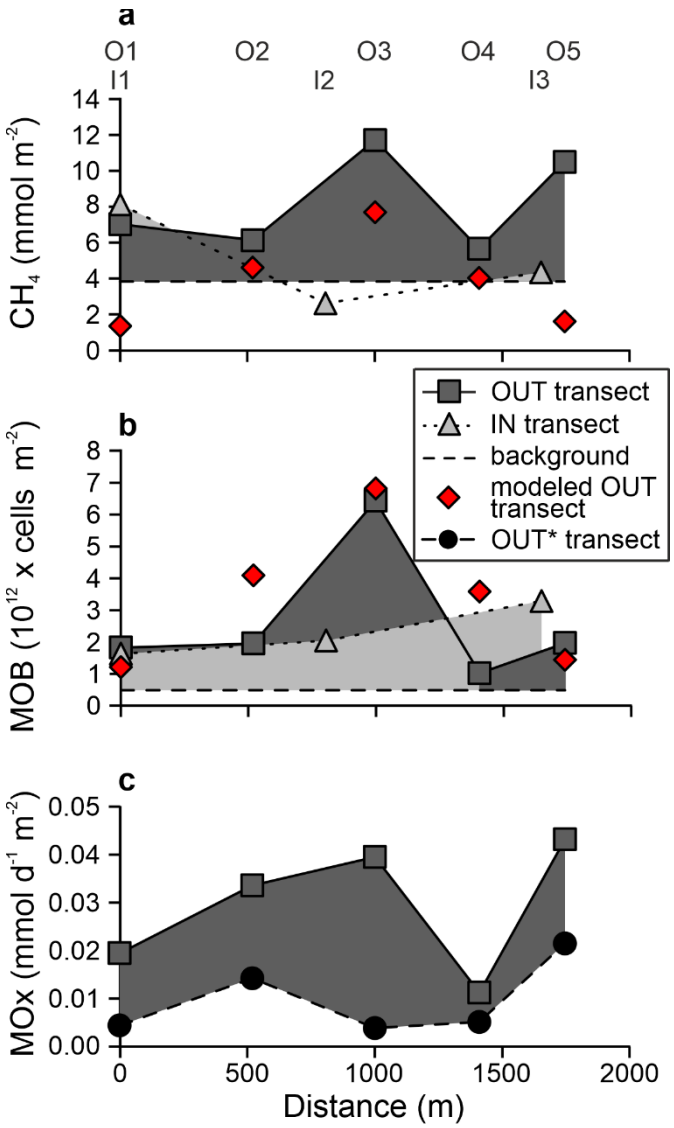

Fig. 30 | Depth-integrated (35–90 m) inventories. a, Methane and **b**, methane-oxidizing bacteria (MOB) for the IN (light grey triangles) and OUT (dark grey squares) transects and for the modelled OUT transect (red diamonds). The dashed line indicates the values measured at the background station. In **c**, methane oxidation rates (MOx) are shown for the OUT (grey squares) and OUT* (black circles) transects. The latter was calculated as the MOB cell abundances of the background site multiplied by the cell-specific methane oxidation rates (MOx) of the OUT transect for each depth (see section 5.3.5).

4.3.4 Particle ejection from the Blowout and dispersion in the water column

In dynamic ocean settings influenced by tidal cycles, sampling can provide only a snapshot of the water column's biogeochemical status. Thus, to reconstruct the events of the field campaign, a Lagrangian particle model was employed. Fig. 31 shows the modelled vertical MOB cell inventories (35–90 m) along the transects as determined during sampling (Fig. 31a, OUT transect; b, IN transect). To match the inventories at the sampling stations, a linear scaling factor was applied such that each particle in the model represented a certain number of MOB cells; this was done by fitting the modelled to the observed inventories. A further important parameter that influenced the results and the particles' spatial spreading was the horizontal diffusivity. The ocean model predicted an average horizontal diffusivity of 3 $m^2\ s^{-1}$ but this value resulted in a particle plume that was too narrow. Thus, sensitivity experiments were performed by varying the diffusivity between 4 and 20 $m^2\ s^{-1}$. A value of 8 $m^2\ s^{-1}$ achieved the best agreement with the observed inventories at all sampling stations (Fig. 31). Although it deviated from the prediction of the ocean model, the model had a spatial resolution of one nautical mile. Thus, it could only resolve horizontal shear and strain at this length scale. Since the sampling regions spanned only a few kilometers, the ocean model likely underestimated small-scale horizontal turbulence. In accordance with this procedure, it was estimated that each discrete particle was representative of 1.016×10^9 MOB cells. Both of the modelled distributions shown in Fig. 31 revealed an apparently northward-directed MOB cell plume, consistent with the low tide. The MOB abundance in the plume was between ~10^{12} and ~10^{13} but lower in the rest of the Blowout area (~10^{11}). For the period corresponding to the fieldwork (August 31–September 7, 2016), the model described the variability in MOB cell abundance and the clockwise motion of the plume with the tides (Jordan et al. 2021, Movie S1).

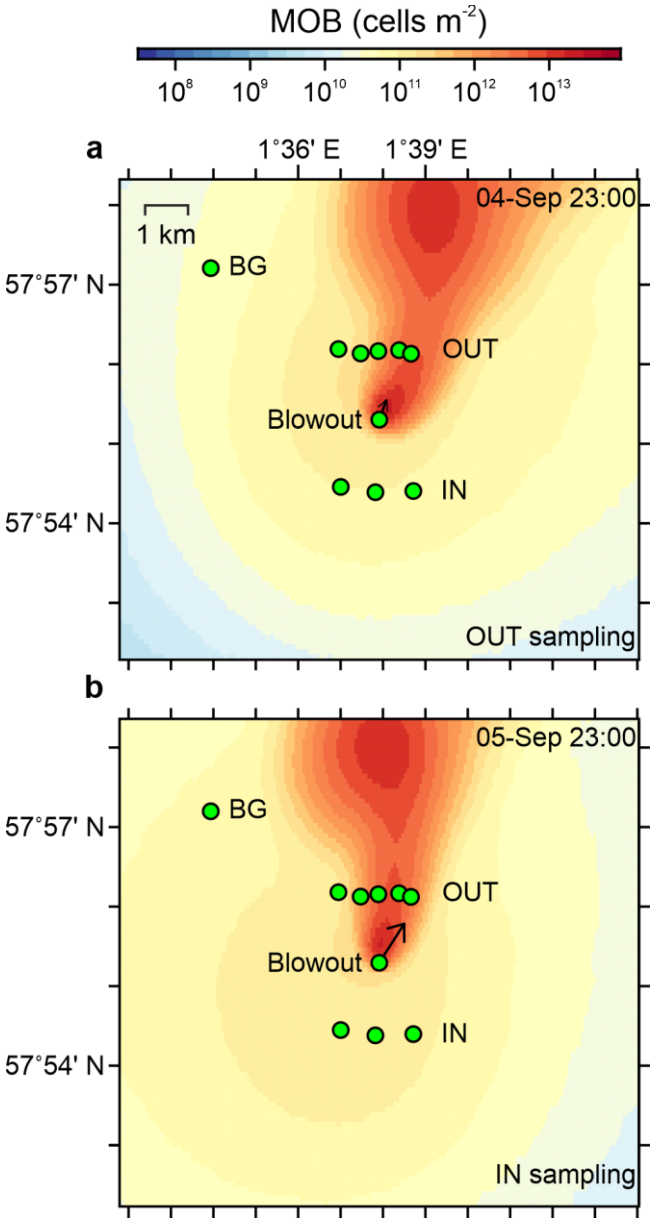

Fig. 31 | Modelled spatial distributions of MOB using a Lagrangian particle-tracking model. Sampling dates are indicated in the figure for **a**, the OUT transect and **b,** the IN transect over a depth range of 35–90 m. The color-coding represents the MOB cell concentration, the green dots the sampling stations, and the arrow the instantaneous current direction.

Based on the particle-tracking model, a release rate from the crater of 4.29 ± 1.9 × 10^{12} MOB cells s^{-1} was predicted. The OUT transect covered ~12% (1.74 km) of the plume's total width (~14 km) containing ~70% of the released MOB cells (Fig. 32c). Following the same procedure, the model was used to estimate that 62 ± 40.9 L CH_4 s^{-1} had to be released by the Blowout at seabed level to account for the measured methane distribution. However, as Leifer (2015) used lab-supported video measurements for the entire crater, the estimated 90 L s^{-1} were used for further calculation. In addition, the model was used to calculate the mean escape time for the released particles; that is, the time needed for a particle to move 3, 5, and 10 km away

from the Blowout (Fig. 32a). The results showed that the particles were fastest on August 28, covering a distance of 10 km within one day, in contrast to the 7 days needed during most of the sampling campaign. The mean escape time estimated from the residual current speed (Fig. **32**b) yielded a similar overall pattern, with a maximum of ~10 cm s^{-1} at the beginning of the field campaign and a decrease to ~5 cm s^{-1} towards the end. The minimal residual current speed occurred on September 3 (~0.1 cm s^{-1}), and the maximum on August 28 (~14 cm s^{-1}).

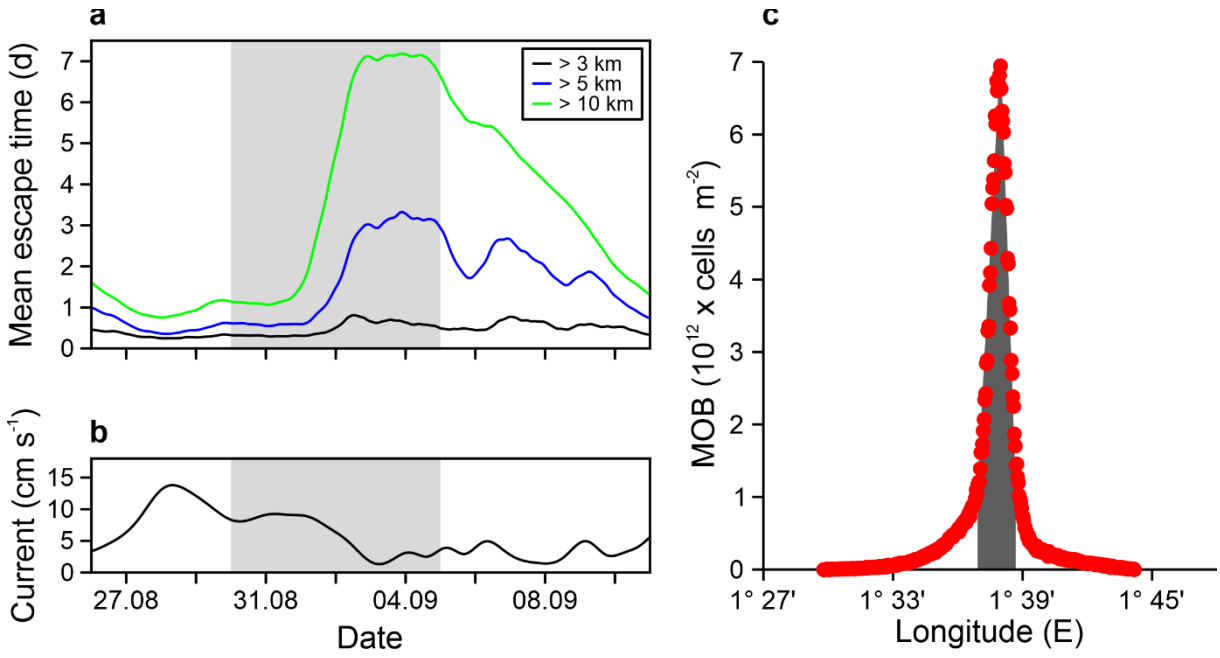

Fig. 32 | Residual current speed, mean escape time of modelled MOB cells and plume coverage. **a**, Mean escape time of released MOB cells over distances of 3, 5, and 10 km and **b**, the respective residual current speed during the fieldwork campaign (shown in grey). **c**, MOB plume coverage along the OUT transect. MOB cell inventories calculated by the particle model for the whole plume released by the Blowout at the Latitude of the sampled OUT transect (dark grey) and its coverage of the plume. All depicted MOB concentrations were above the background station's inventory.

5 Discussion

5.1 Characterization of the bubble-mediated transport process: an example from the Coal Oil Point seep field

5.1.1 The Coal Oil Point seep field

The high gas-venting activity in the Coal Oil Point seep field was reflected by elevated dissolved methane in the sediment and water column (Fig. 19a, d), and agreed with previous studies at similar gas-venting sites (Treude and Ziebis 2010; Schmale et al. 2015; Steinle et al. 2016). Water column methane concentrations above the COP seep sites correlated with gas seepage intensity, featuring higher methane concentrations at the more active IV Super Seep site compared to the moderately active Rostocker Seep site.

Total cell numbers in the sediment at both sites were in the range reported in previous studies conducted at COP (Treude and Ziebis 2010; Schmale et al. 2015). MOB were detected at deeper, potentially anoxic sediment depths, a pattern that was previously described by Schmale et al. (2015) at Rostocker Seep, who proposed that the oxygen penetration depth is increased by bubble-driven pore water convection (Dando et al. 2000; Haeckel et al. 2007; Treude and Ziebis 2010). Such convection would allow MOB to settle in deeper, normally anoxic sediment strata. However, MOB cell numbers shown above were one order of magnitude lower than those reported by Schmale et al. (2015). This difference might be explained by the disturbance of the surface sediment by the heavy wind-induced surf in the days before the start of the fieldwork. Kersten et al. (2005) showed that such events have the potential to mix the upper sediment layer and to dislocate surface sediments over distance scales of meters (Williams and Rose 2001; Kersten et al. 2005). This surface-sediment refreshing sand transport would have brought MOB-poor sediment into the sample sites at COP possibly explaining the lower cell numbers. Such an event-driven introduction of medium sand grains of similar sizes to both seep sites would explain the similarity in the bubble size distribution pattern as analyzed at all four seep vents (Fig. 20).

5.1.2 Transport efficiency

By including different seep sites, this present study allowed for a first-time parameterization of the factors controlling the bubble transport mechanism. These experiments showed that MOB transportation rates (e.g., cells emitted per mL of gas) were highest at a low (RSV1: 0.07 mL s^{-1}, 2.3 × 10^4 cells mL^{-1}_{gas}) and lowest at a high volumetric gas flow (SSV2, 2.2 mL s^{-1}, 2 × 10^2 cells mL^{-1}_{gas}) with a mean of 8 × 10^3 cells mL^{-1}_{gas} (Fig. 22), indicating that volumetric gas flow substantially affects bentho-pelagic transport efficiency. The observed

decrease in transportation rates at higher gas flows implied that microorganisms were removed faster from the sediment than could be compensated by growth and/or supply from the surrounding environment. Another possible explanation for the lower transportation rate could be differences in bubble migration characteristics. At low volumetric gas flows, the sediment migration pathway collapses or partially collapses after each bubble, whereas at higher volumetric flows the conduit remains open for a prolonged period of time (Boudreau et al. 2005; Algar et al. 2011). In collapsed conduits, particles, pore water, and microorganisms refill the bubble migration pathway. Thus, bubbles slowly migrating through a collapsed conduit have greater potential to interact with the surrounding sediment than do bubbles rising through an open migration path. In addition, it is likely that the continuous gas bubble sparging in an open rise path more rapidly depletes microorganisms. However, a corresponding decrease in cell numbers in the sediment taken above an active vent was not detected in sediment samples (Fig. 19). This might have resulted from the sampling approach, in which sediment slices were homogenized before subsamples were taken for cell counting. Thus, background sediment cell numbers of 10^9–10^{10} cells cm^{-3} could have masked localized depletion.

The overall impact of the bubble transport mechanism on the abundance of MOB in the overlying water column was determined by extrapolating the numbers of cells transported per volumetric gas flow over the number of active vents per square meter of seabed (Fig. 33). These data show that even vents with high volumetric gas flows and accordingly low numbers of transported cells per gas bubble (e.g., SSV2, Fig. 22b, c) can have comparatively high cell transportation rates given the high numbers of active vents per seabed area (Fig. 22d). However, as the bubble-mediated transport itself is coupled to the volumetric gas flow, one can propose that factors influencing this flow, such as hydrostatic pressure (including waves and tides; Schneider von Deimling et al. 2010; Römer et al. 2016; Leifer 2019; Lohrberg et al. 2020) and temperature (Aben et al. 2017), likely affect the transportation rate of MOBs though these were beyond the scope of the data collected.

Two additional types of Bubble Catcher experiments were conducted to allow for the transportation of water-borne microorganisms (“BC engineered”) and the introduction of contamination during Bubble Catcher handling (“BC control”) and “BC vent” experiments. The “BC control” experiments without gas bubble transport into the sampling cylinder featured low numbers of microorganisms, indicative of minor contamination of these samples by air- and/or water-borne microorganisms. The majority of this contamination (10^3 cells mL^{-1}) probably resulted from the scuba-diver operations with the Bubble Catcher at the seafloor. Additional microorganisms may have been introduced through sediment that was resuspended by wind and wave action (Orvain et al. 2003; Ferguson et al. 2005). Air-borne contamination during sample handling and filtration were likely low, due to the differences in cell concentration of air (10^3–10^7 cells m^{-3}; Hu et al. 2017) and sample water (10^{10}–10^{11} cells m^{-3}).

Although in the “BC vent” experiments, bubbles escaping into the water column were likely loaded with bacteria, fine particles, and surfactants collected from the sediment, the “BC engineered” experiments were designed to assess the contribution of water column-borne microorganisms to the bubble transport mechanism. Previous studies have shown that particles and microorganisms in the sediment adsorb to the bubble interfaces due to the surface activity of bacterial cells (Wan et al. 1994; Wan and Wilson 1994b). Different to the “BC vent” experiments, bubbles in the engineered bubble experiment were not pre-coated by surfactants prior to their migration through the water column. Thus, engineered bubbles likely provided a greater available surface area for transportation and therefore collected more water-column bacteria before entering the Bubble Catcher (5 cm from sediment to Bubble Catcher entrance). If the engineered bubbles were indeed more efficient in sparging microbes from the water column into the Bubble Catcher, then MOB transport rates, and total cell numbers calculated for the “BC vent” experiments would be underestimated.

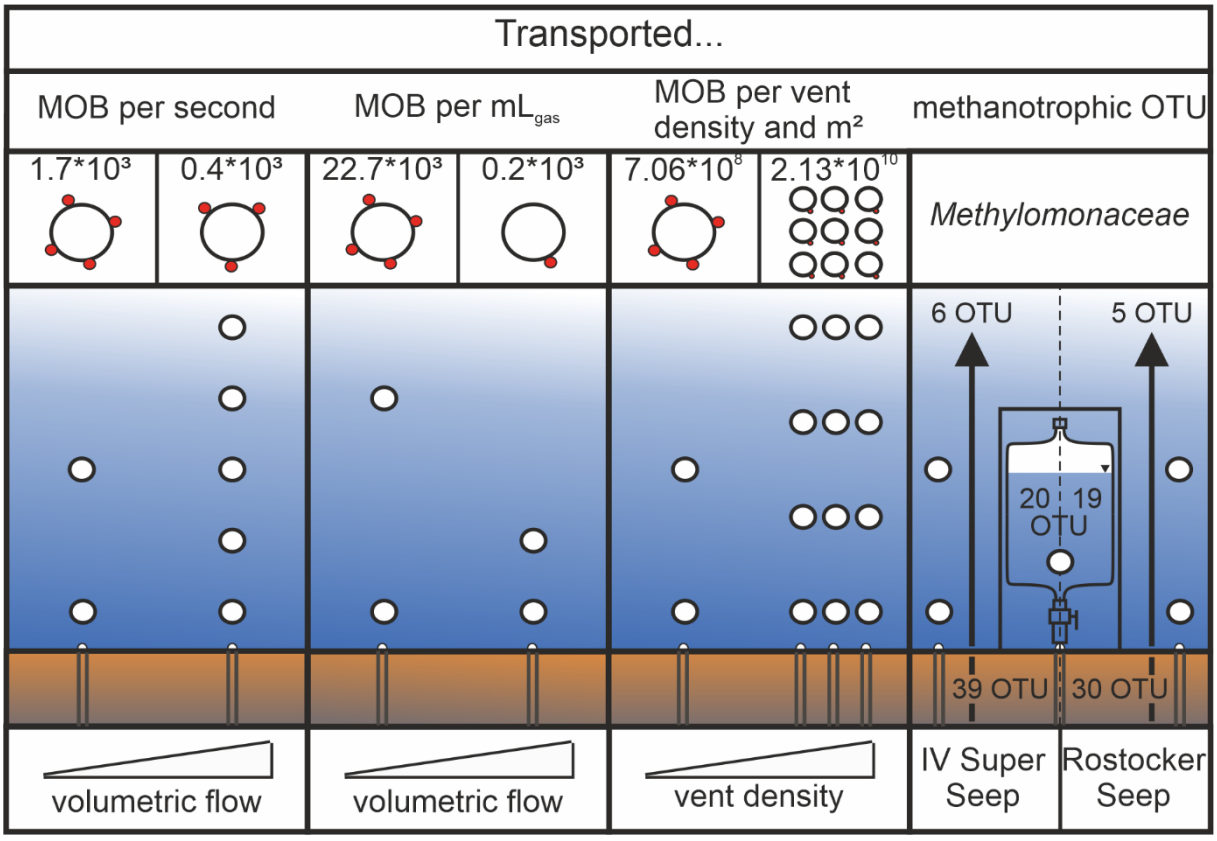

Fig. 33 | Summary of the parameters influencing the bentho-pelagic transport process of MOB. Influence of the volumetric flow and vent density on the transport of benthic MOB. Comparison of Rostocker Seep and IV Super Seep regarding the OTU assigned to the family *Methylomonaceae* found in the three compartments sediment, Bubble Catcher and water column.

5.2 Genetic identification and survival of transported microorganisms at the Coal Oil Point seep field

The quantitatively observed transport of MOB with CARD-FISH was supported by genetic analysis. Based on methanotrophic OTUs, some benthic MOB were transported from the sediment into the water column while others remained in the sediment. A bubble-mediated bentho-pelagic transport of methanotrophs was indicated by the detection of methanotrophic OTUs, in the sediment, in the "BC vent", and in the water column samples (IV Super Seep OTUs: 1, 2, 3, 9, 10, 11; Rostocker Seep OTUs: 1, 2, 3, 17, 16). Four of these OTUs were also found in the samples from the "BC engineered" experiments (IV Super Seep: 3; Rostocker Seep: 1), which confirmed the bubble-induced stripping of bacteria from the water column into the Bubble Catcher sampling cylinder. This mechanism would have the potential to dislocate microorganisms within the water column, even across boundary layers such as pycnoclines. The detection of 18 methanotrophic OTUs in both sediment and "BC vent" samples (IV Super Seep OTUs 4–8, 12–15; Rostocker Seep OTUs 4–8, 9, 18–20), which were absent in the water column, suggests that some MOB cells transported into the Bubble Catcher either quickly sank back to the seafloor or perished in the pelagic environment. The transport patterns from 8 of 20 methanotrophic OTUs were similar at the two seep sites (red OTU numbers, Fig. 23a), whereas there was no such similarity for the ASV distribution. Microbial transport efficiency may be affected by the specific cell surface activity of microorganisms, which results, for example, from inter-species differences in outer membrane composition and extracellular components (Schäfer et al. 1998; Malhotra et al. 2019) but also depends on the growth conditions (e.g., nutrient levels; Stenstrom 1989). Also, the cell position in a biofilm can influence their anchorage on particles and their likelihood of detachment by external forces (Jang et al. 2017). In addition, a recent study on the aerosolisation of bacteria and viruses at the ocean-atmosphere interface suggested that cell morphology is a critical parameter that influences bubble-induced transport between these two environments (Michaud et al. 2018).

Our *pmoA* analysis supported the 16S-rRNA-based transportation pattern. The six ASVs found in the sediment, "BC vent" experiment, and water column provided evidence of the bubble-mediated transport of benthic MOB across these habitats. Among the transported ASVs, 37 were assigned to the family *Methylomonaceae*, which agreed with the 16S rRNA gene results. However, the identified ASVs probably belonged to unknown marine species, because the only assignments that could be made using the reference database was to a species isolated from a freshwater lake (*Methyloglobulus morosus*), whose growth is reduced already at a very low salinity (Deutzmann et al. 2014), as well as to a species isolated from a Kenyan soda lake, which grows optimum is at pH >9 (*Methylomicrobium kenyense*; Kalyuzhnaya et al. 2008).

Based on current knowledge, neither species was likely to have existed in the sampled environment.

A previous study by Tavormina et al. (2008) used *pmoA* sequences from sediment and water column (3 m above sea floor) samples to investigate MOB community structure in two methane vent environments at water depths between 500 and 700 m, at the Eel River Basin and the Santa Monica Basin, respectively. A comparison of the 16 *pmoA* isolates in sediment and water samples from the two sites showed distinct methanotrophic communities with very little overlap between the two environments. In addition, the 16S rRNA gene analysis did not recover methanotrophic lineages. By contrast, 40 OTUs belonging to methanotrophic lineages were detected at the COP (Jordan et al. 2020), of which eight were shared by the seep sediment and overlaying water column. However, using next generation sequencing methods resulted in a higher sequencing depth than achieved with the clone-library-dependent sequencing technique used by Tavormina et al. (2008). The difference in techniques and the respective sensitivities might explain the differences in the observed community overlap. Another possible explanation for the absence of benthic MOB in the water column in the Tavormina et al. (2008) study could have been the sampling depth (3 m above the seafloor). During their travel through the water column, ascending gas bubbles released at greater water depth continuously exchange gases with the surrounding water via their surfaces, resulting in a general decrease in bubble size with increasing distance from the seabed. It is expected that the constant shrinking of the gas bubbles surface during ascending (McGinnis et al. 2006) increases the shear stress on the attached microbial cells leading to a preferential release of MOB at shallower water depth. For the time of the study the elevated shear stress at the bubble surface provoked by wake eddies (Clift et al. 1978) support the detachment of microorganisms already near the seabed. Differences in environmental factors, such as oxygen concentration in the water column, seep characteristics, and volumetric gas flows, between the COP seep field and the seep sites investigated by Tavormina et al. (2008) may also explain the lack of MOB in the water column. Although the 16S rRNA gene analysis indicated an overlap between the methanotrophic communities.

The fact that some of the transported OTUs were found in the water column while others occurred only in the “BC vent” experiments suggest different survival rates of sediment-borne bacteria in the water column. However, Bubble Catcher water samples from the “BC vent” experiments provided direct evidence of methane oxidation in incubations performed over a 3-day runtime directly after Bubble Catcher subsampling. Averaged methane oxidation rates of “BC vent” (~900 nmol L^{-1} d^{-1}) were three orders of magnitude higher than “BC engineered” (~0.6 nmol L^{-1} d^{-1}) and five orders of magnitude higher than “BC control” (~0.005 nmol L^{-1} d^{-1}) rates. Thus, at least some of the transported MOB were active after their dislocation into the water column.

In addition, the incubation experiments with Bubble Catcher sample water indicated that the benthic MOB remain active after transportation and showed a drastic increase in MOB cell abundances after one week of incubation, which decreased again over time but was still elevated after three weeks. Methane oxidation rate constants (k') were highest for the incubation Inc1 after one week and still elevated after three weeks compared to the beginning of the incubation (see Table 6). For incubations Inc2, on the other hand, k' increased over the incubation period whereas in the control incubation IncE k' decreased after one week and then increased again after another two weeks though was still less than at the beginning. However, due to the difference in the timing of growth and the increase in methane oxidation between Inc1 and Inc2, bottle effects during incubations cannot be completely excluded. Taken together, these incubation experiments showed MOB growth and thus increasing methane oxidation over time. Transferred to the seep site, this indicates ongoing activity of benthic MOB after transportation and even growth in an ageing plume that further accelerates methane oxidation. Mesocosm experiments by Chan et al. (2019) showed that methane oxidation increased sharply after a lag phase of ~1–2 weeks following methane release and remained high even after a significant decrease of the methane concentration.

Aside from MOB, genetic analysis further indicated the transport of OTUs assigned to the genus *Cycloclasticus* (Fig. 23). Members of this genus have been reported to metabolize polycyclic aromatic hydrocarbons (PAHs; Messina et al. 2016; Wang et al. 2018) and have been playing a dominant role in the degradation of oil (Hazen et al. 2016), for example in the Deepwater Horizon oil spill (Kleindienst et al. 2016; Gutierrez et al. 2016). In addition, symbiotic *Cycloclasticus* associated with mussels and sponges use short-chain alkanes rather than PAHs. However, so far no members of the genus *Cycloclasticus* were observed to oxidize methane (Lai et al. 2012; Kleindienst et al. 2016). One can propose that *Cycloclasticus* species play a role in the degradation of petroleum compounds in the sediment and water column of COP (Hornafius et al. 1999; Leifer et al. 2000), with the latter being enhanced by the bubble-mediated transport. A similar effect was suggested for the wave- and wind-induced resuspension of sediment particles and, thus, benthic microorganisms, hydrolytic enzymes, and organic matter, which could then enhance microbial metabolism in the water column (Garstecki et al. 2002; Ziervogel and Arnosti 2009; Bertagnolli et al. 2011). Consequently, it is conceivable that the bubble-mediated transport mechanism influences other biogeochemical processes in the vicinity of gas seeps, too.

5.3 The impact of dislocated benthic methane-oxidizing bacteria on the pelagic methane dynamics

5.3.1 Contribution of transported methanotrophs onto the pelagic methanotrophic community at the Coal Oil Point seep field

To assess the impact of the Bubble Transport Mechanism in the COP water column on MOB abundance, a rough calculation to derive the transportation time and distance required to achieve the detected water column MOB stock was performed (Fig. 19c). The transportation distance (∆x) needed to achieve the detected average water column MOB cell concentration (c) was calculated from the current velocity (v), the water depth (z), and the sediment-born MOB flux (F) as shown in Eq. 10.

$$\Delta x = (c * v *\cdot z) / F \qquad (10)$$

Calculations were performed with the variables listed in Table 8:

Table 8 | Parameters used to estimate the Bubble Transport Mechanism to the water column MOB stock.

	c (cells m^{-3})	v (m s^{-1})	z (m)	F (cells m^{-2} s^{-1})
IV Super Seep	1×10^9	0.1[a,b]	16	1.38×10^6
Rostocker Seep	1×10^9	0.1[a,b]	10	8217

[a]Clark et al. (2000), [b]Winant et al. (2003)

For the calculation, a constant bubble-mediated MOB input into the overlying water column and survival of the transported organisms was assumed. Calculation was performed for two different intensities of sediment-born MOB inputs: (i) maximum input as measured at the IV Super Seep site, and (ii) minimum input as detected at the Rostocker seep site (Fig. 22). According to these assumptions, it takes about (i) 3 hours (1 km) to (ii) 14 days (121 km), respectively, of bubble-mediated transport to reach the number of water column MOB cells observed. Even if MOB cell division (about 3 days; Kessler et al. 2011) within the methane-enriched plume water would further shorten these transportation times, the assessment shows that a relevant part of the water-column MOB stock was likely transported from gas-releasing seep sites further upstream from the COP seep field. Such a scenario is likely since the shallow waters along the southern Californian coast harbor gas-bubble releasing seep sites for at least

over 100 km upcurrent (Heintz et al. 2012; Leifer 2019). These seeps will contribute to a high ambient water column MOB concentration while the waters are transported northwards by the coastal current system (Hickey 1992; Winant et al. 2003; Heintz et al. 2012). However, for a solid estimate of the effect of the bubble-transport mechanism on the water column MOB stock in seep regions, an isolated seep area, with low and uniform background MOB concentrations, and a defined current system would be required.

5.3.2 Gas seepage activity at the North Sea blowout well 22/4b and its impact on the methane plume distribution

Since the drilling accident in 1990, the Blowout location has been repeatedly examined to track the intensity of gas liberation from its crater. During this field expedition, video footage obtained with an ROV was used to determine gas seepage activity from the crater (Jordan et al. 2021, Movie S2, S3) and revealed that neither the morphological appearance of the Blowout nor the intensity of gas bubble release had visibly changed since the last video-based crater observations, in 2012 (Schneider von Deimling et al. 2015, Video S3).

For mega seeps sites with a gas flow of ~10^6 L d^{-1} (e.g., Blowout) some additional plume mechanics apply, e.g., this benthic flow created scars in the crater rim along the major inflow paths (Schneider von Deimling et al. 2015). Schneider von Deimling et al. (2015) observed that gas jets, which were released under high pressure, showed a spiral vortex motion with a frequency of about 2–4 Hz. This spiral motion enhances the travel distance and thus results in a vortical bubble trapping. They further showed that the overall bubble plume followed a similar spiral rotation. Hydroacoustic images of the water column during the expedition showed that the Blowout crater's gas-bubble release created an extensive bubble plume that divided into two parts. This splitting of the bubble plume was also described by Schneider von Deimling et al. (2015) using data from a field expedition in 2006, which indicates that the dynamics of the plume did not significantly change between 2006 and 2016. Earlier investigations found that the Blowout's bubble plumes were mainly created by five major vents (Leifer 2015; Schneider von Deimling et al. 2015), with an in situ gas flux in the range of 0.50–3.50 L s^{-1} (Leifer 2015). However, the respective gas fluxes determined in the study ranged between 0.470 and 0.729 L s^{-1}, suggesting a decrease in the intensity of gas seepage, at least for these major vents, between 2011 (Leifer 2015) and 2016 (Jordan et al. 2021).

Long-term acoustic monitoring studies conducted between July 2011 and January 2012 documented relatively consistent gas fluxes from the Blowout, albeit interrupted by a series of major episodic gas outburst events (Wiggins et al. 2015). The video observations from the ROV supported vigorous outbursts, where one can note large lumps (~0.5–2 m, Fig. 6d;

Jordan et al. 2021, Movie S2) of solid sediment, most likely clay, within the crater and at its rim. These sediments might have been ejected from deeper sediment strata and were not reported in previous studies of the Blowout.

Previous studies showed that gas bubbles released from the Blowout crater partly dissolve during their passage through the water column and thereby create a plume of dissolved methane (Leifer et al. 2015; Schneider von Deimling et al. 2015). In during the expedition the plume was mapped inside the sub-thermocline water body within a distance of 1.6 km from the Blowout (Fig. 28 and Videos S1+S2). A comparison of the sub-thermocline methane inventories along the two transects showed a nearly two-fold higher inventory in the OUT compared to the IN transect (Fig. 30a and Table 2). Moreover, only ~9% (IN) and ~23% (OUT) of the total methane inventory was located in the upper 35 m of the water column, indicating a quick release of methane from the bubbles during their ascent through the sub-thermocline water column (Leifer et al. 2015) and a hampered transport of dissolved methane through the lower thermocline (Nauw et al. 2015b). Previous studies at the Blowout demonstrated that <10% of the released methane reaches the mixed layer during the pronounced water column stratification in summer (Leifer 2015; Schneider von Deimling et al. 2015; Sommer et al. 2017). However, a local methane concentration anomaly within the mixed layer (~300 nmol L^{-1} at 20 m, station O4; Jordan et al. 2021) was detected that accounted for ~21% of the total vertical methane inventory at this station. The station O4 laid directly in the downcurrent direction of he dissolved methane plume during sampling time. One can assume that, as the plume orientation changes with the current direction (Jordan et al. 2021, Movie S1), the methane plume penetrates the thermocline the most when rising straight upward, e.g., during slack water tidal phase. Schneider von Deimling et al. (2015) proposed a similar mechanism. Such a mechanism combined with plume-induced upwelling might be able to periodically increase methane transport across the lower thermocline. This methane is transported downcurrent when the slack water tidal phase ends and the current velocity increases again.

5.3.3 Dispersion of the ejected methanotrophic bacteria in the water column surrounding the Blowout location

MOB cell distribution showed about ~40% of the total vertical inventory of MOB cells in the OUT and IN transect below the lower thermocline (Fig. 30b), while at the background station only ~20% of the MOB cells were located below the lower thermocline (Fig. 27b). However, while in the mixed layer the MOB concentration was high, the methane oxidation rate was low, consistent with the low methane concentration and inhibitory effects of light (Murase and Sugimoto 2005) and high oxygen concentration (Rudd et al. 1976; Steinle et al. 2017). However, similar to the methane distribution, the highest MOx capacity was detected in the

OUT transect below the lower thermocline (~94% of the total MOx capacity; Table 1), consistent with the northward residual transport. A comparison of the sub-thermocline MOB inventories along the IN and OUT transects showed a 1.3-fold higher inventory in the downcurrent positioned OUT transect (Fig. 30b), indicating an immediate impact of the methane point source on the pelagic MOB abundance. Compared with the background station 5 km away from the Blowout, the MOB cell concentrations in the two transects were up to 10-fold higher than at the background station (Fig. 29). The substantial enrichment of MOB cells in the near field of the Blowout was reproduced by the particle-tracking model (Fig. 31). The model demonstrated that the northward-oriented spreading of the MOB cell plume was affected by tidal cycles, which caused a clockwise oscillating motion of the plume (Jordan et al. 2021, Movie S1). This movement forced the plume multiple times into the vicinity of the Blowout, resulting in repeated collections of MOB cells ejected from the seep site. The calculated mean escape time described above revealed that high current velocities (10–14 cm s^{-1}, Fig. 32b) would lead to the rapid removal of MOB cells from the Blowout region (Fig. 32a) and thus a dilution of their abundance (Jordan et al. 2021, Movie S1; time frame: August 26 to September 9, 2016). In contrast, a lower current velocity would result in both a longer mean escape time (1.5–2 cm s^{-1}, Fig. 32a) and an enrichment of MOB cells in the Blowout region. Hence, one can disregard MOB community growth effects on the plume MOB stock in sub-thermocline waters, because the water and associated MOB community were swept away from the Blowout regions on times scales shorter than average MOB cell doubling times (~3 days; Murrell 2010; Kessler et al. 2011; Fig. 32 and Jordan et al. 2021, Movie S1).

Patches of elevated MOB cell concentrations were detected in the surface waters at station O3 and O5 of the OUT transect (Fig. 28c), presumably indicating a bubble-mediated (Schmale et al. 2015; Jordan et al. 2020) cross-thermocline transport of these cells. By contrast, methane concentrations in the surface water at both stations were relatively low (Fig. 28a, b and section 5.3.2). In general, while methane is quickly released from the bubbles into the surrounding water (Leifer et al. 2015), they also continuously take up gas (e.g., nitrogen and oxygen) from the water, which counteracts their complete dissolution (McGinnis et al. 2006) and enables their further ascent through the water column. Particles (including bacteria) attached to bubble surfaces can thus be transported across strong density gradients, such as thermoclines, that inhibit an exchange of particles or dissolved substances by pure diffusion or advection (Nauw et al. 2015b; Schmale et al. 2016). Leifer et al. (2015) proposed that the bubble rise velocity is accelerated by the bubble-plume-induced upwelling flow (Schneider von Deimling et al. 2015), which in turn favors the survival of the bubbles and therewith bubble-mediated transportation of MOB cells into the mixed layer. This bubble-mediated cross-thermocline transport would be increased by the low residual current velocity in the mixed layer (5 km in 4 days, Fig. 26) as the waterbody has more time to accumulate MOB. The slow movement of the surface and

mixed layer provides enough time for a slight increase of MOB cells due to subsequent cell doubling (MOB doubling time of ~3 days).

5.3.4 Estimated number of methane-oxidizing bacteria and amount of methane ejected from the Blowout

The particle-tracking model proved to be a highly valuable tool with which to estimate MOB cell numbers and the amount of methane ejected from the Blowout into the water column. The model output indicated that 4.29 ± 1.9 × 10^{12} MOB cells s^{-1} were released from the Blowout into the water column to maintain the sub-thermocline MOB cell inventory measured along the IN and OUT transects (Fig. 30b). Based on a gas release of 90 L s^{-1} from the crater (Leifer 2015), a MOB cell-ejection rate of 4.8 × 10^{10} MOB cells L^{-1} gas were computed, for rates of 142 L gas s^{-1} and 50 L gas s^{-1}, the corresponding ejection rates would be 1.7 × 10^{10} MOB cells L^{-1} and 1.2 × 10^{11} MOB cells L^{-1}. A comparison of the bubble-mediated MOB cell transport in the Coal Oil Point seep field at the Isla Vista Super Seep (1.2 × 10^{11} MOB cells m^{-2} d^{-1}, 700 vents m^{-2}; Jordan et al. 2020) with the Blowout crater (1.35 ± 0.6 × 10^{15} MOB cells m^{-2} d^{-1}, based on a seepage area within the crater of ~275.5 m^2; Leifer 2015), suggests that MOB cell transport per square meter of active seepage area was four orders of magnitude higher at the Blowout. Based on this comparison, one can propose that the resuspension of crater sediment (Schneider von Deimling et al. 2015) played an essential role for the coupling of benthic and pelagic MOB communities at the Blowout, in addition to the bubble-mediated transport of MOB cells. The letter were identified as the dominant transport process in the Coal Oil Point seep field (Jordan et al. 2020). This conclusion is further supported by phylogenetic analysis indicating similarities in the microbial community composition between Blowout crater surface sediments and bottom water (Steinle et al. 2016), as well as an elevated turbidity in the crater interior (Fig. 6b, e, Jordan et al. 2021, Movie S2, S3). The strong turbidity inside the crater (Jordan et al. 2021, Movie S2) and the high particle load deposited on the sample-filter from above a major vent (see section 4.3.3), suggested that the enhanced resuspension is driven by vigorous gas-bubble fluxes and resulting in an induced upwelling flow, followed by compensation of the removed water by enhanced lateral water flows into the crater (Wilson et al. 2015). The MOB abundance in the mega bubble plume (2.2% of total cells) above the corresponding major vent was less than that at a location immediately next to the plume (9.7% of total cells), which suggests that medium and small vents, together with indirect resuspension, result in the transport of more MOB cells into the water column than achieved from major vents. Moreover, these transport mechanisms are not limited to benthic MOB cells, as in a previous study Jordan et al. (2020) described the transport for benthic oil-degrading bacteria of the genus *Cycloclasticus*.

Other studies showed that the bubbles emitted from the crater accelerate an upwelling flow that supports the upward transportation of resuspended sediment particles and their enrichment below the lower thermocline (Schneider von Deimling et al. 2015; Wilson et al. 2015). The MOB cell-enrichment detected in the center of the OUT transect (Fig. 28c, station O3, 5.3×10^8 MOB cells L^{-1} at 35 m) likely resulted from such a transport mechanism. The bubble stream's upward movement was evidenced by the hydroacoustic water column data, which were consistent with a splitting of the gas bubble flare near the lower thermocline (at ~35 m water depth, Fig. 25b). The thermocline probably acted as a barrier, with small bubbles trapped in sub-thermocline water (Schneider von Deimling et al. 2015) and larger bubbles ascending more rapidly (Leifer et al. 2009) and able to reach the surface. Leifer et al. (2015) proposed that the rising speed of the bubbles is accelerated by the bubble-plume-induced upwelling flow, which in turn increases the distance they travel. MOB cells could be transported into the mixed layer via this route, thus contributing to the relatively high MOB cell concentrations at shallow water depths. However, a dye experiment conducted by Schneider von Deimling et al. (2015) at the Blowout site showed that, after initially following the bubble plume, the dye was transported back to the seabed and no coloring of the water surface occurred. These results instead suggest that most resuspended particles, small bubbles, and already-detached MOB cells stay below the lower thermocline during stratification of the water column in summer.

Both Leifer and Judd (2015) and Schneider von Deimling et al. (2015) estimated that >90% of the released methane stays below the lower thermocline. Under this assumption, the Lagrangian particle distribution calculated for MOB cells was retuned using the measured methane concentration to assess the methane release of the Blowout. This approach suggests the release of 62 ± 40.9 L CH_4 s^{-1} at the seabed level. The methane inventories calculated from the model output peaked at the central station (O3, Fig. 31) but were lower than the inventories of the sampled concentrations (Fig. 30), such that the actual methane release was slightly underestimated. The calculated methane release rate falls within the lower end of the previously reported 45–128 L CH_4 s^{-1}, with a best estimate of 81 L CH_4 s^{-1} (Leifer 2015). The flux determined at two of the major vents (0.470–0.729 L s^{-1}, Table 7) was in the lower range of the 0.51–3.5 L s^{-1} reported by Leifer (2015). Together, these results, including the calculated methane release, point to a slight decrease in the Blowout's activity since 2011.

5.3.5 Impact of methane-oxidizing bacteria ejection from the Blowout crater on the water column methane sink

The model results suggest that the MOB enrichment in the plume waters (Fig. 31) results from the ejection of cells from Blowout crater sediments into the water column. Following this assumption, the data obtained in the downcurrent-oriented OUT transect were used to estimate the impact of MOB cell ejection on the efficacy of the pelagic methane sink. Therefore, an OUT transect unaffected by MOB cells' ejection (hereafter referred to as OUT*) was deduced. First, the cell-specific methane oxidation rate (cell-specific MOx) was determined per sampled depth (Eq. 11).

$$\text{cell-specific } \mathrm{MOx} = \mathrm{MOx} \,/\, [\mathrm{MOB}]_{\mathrm{OUT}} \tag{11}$$

The methane oxidation at each depth (MOx*) of OUT* was calculated by multiplying the cell-specific MOx with the MOB cell count for the corresponding depth of the background station (MOB_{BG}, Eq. 12, Jordan et al. 2021, Table S3).

$$\mathrm{MOx}^{*} = \text{cell-specific } \mathrm{MOx} * [\mathrm{MOB}]_{\mathrm{BG}} \tag{12}$$

The resulting MOx* rate was used to calculate the fractional turnover rate of OUT* (k'*) following Eq. 13.

$$\mathrm{k'}^{*} = \mathrm{MOx}^{*} \,/\, [\mathrm{CH_4}] \tag{13}$$

Subsequently, the depth-weighted k'* and k' were determined for the sub-thermocline water column by integrating the sub-thermocline k'* and k', respectively, using the trapezoid method, and normalized to the respective depth intervals. Finally, transect-wide k' and k'* were calculated to estimate transect-wide turnover times τ (Eq. 6) for OUT and OUT* using the same integration method and dividing by the transect length.

This approach results in an upper estimate of the methane oxidation capacity within the OUT* transect, since the particle-tracking model indicates that the background station was still slightly impacted by the Blowout MOB ejection (Jordan et al. 2021, Movie S1). The comparison of the methane oxidation inventories (Fig. 30c and Jordan et al. 2021, Table S3) of the OUT and OUT* transects suggests that the methane oxidation capacity along the OUT transect (~0.076 mol m^{-1} d^{-1}) was ~4.6 times higher compared to the OUT* transect (~0.017 mol m^{-1} d^{-1}). The elevated methane oxidation capacity along the OUT transect led to a reduction of the methane turnover time by the same factor (turnover time along OUT* of 883 days vs. 183 days for the OUT transect, Table 9), suggesting that the ejection of MOB cells considerably increased the efficacy of the pelagic methane sink. A near-field comparison between the IN and OUT transects showed that the cell export of benthic MOB into the down current plume increased the methane turnover capacity by ~27%.

As the waters in the Blowout area are seasonally stratified from April/May until October/November (Nauw et al. 2015a), deep-water masses are decoupled from the mixed layer during this period (180–240 days), leading to an accumulation of methane below the lower thermocline. During autumn, this thermal stratification is cancelled out by the mixing of sub-thermocline waters with the sea surface due to storms and colder surface-water temperatures, thus allowing the methane to largely bypass microbial oxidation. A simplified estimate, without invoking changes in the pelagic bacterial community or MOB growth and activity, showed that the methane oxidation inventory, with a turnover of ~183 days, has the potential to oxidize the methane (up to 62%) released into the sub-thermocline waters during the seasonal stratification. Over the same period, the background methane oxidation capacity (calculated from the OUT* transect), with a turnover of ~883 days, would lead to the oxidation of only up to 14% of the methane present in the OUT transect. However, the methane oxidation in the OUT transect would increase over time, as the initial MOB inoculant begins to grow and thus further increases methane turnover. Thus, in addition to the thermocline, the high abundances of MOB cells below this layer might be able to hinder the passage of dissolved methane to the mixed layer and ultimately into the atmosphere.

Table 9 | Methane-related biogeochemical parameters across the IN and OUT transects.

upper water column (0–35 m)	IN	OUT	OUT*
MOB inventory	5.47×10^{15} cells m^{-1}	7.88×10^{15} cells m^{-1}	
CH_4 inventory	0.7 mol m^{-1}	4.2 mol m^{-1}	
MOx capacity	0.0013 mol m^{-1} d^{-1}	0.0052 mol m^{-1} d^{-1}	
Sub-thermocline water body (35–90 m)			
MOB inventory	3.74×10^{15} cells m^{-1}	5.01×10^{15} cells m^{-1}	8.61×10^{14} cells m^{-1}
CH_4 inventory	7.3 mol m^{-1}	14.0 mol m^{-1}	14.0 mol m^{-1}
MOx capacity	0.031 mol m^{-1} d^{-1}	0.076 mol m^{-1} d^{-1}	0.017 mol m^{-1} d^{-1}
k'	0.0043 d^{-1}	0.0055 d^{-1}	0.0012 d^{-1}
CH_4 turnover time	233 d	183 d	833 d

6 Conclusion

Pelagic microbial methane oxidation is the final sink for seabed-derived methane before its release into the atmosphere. Especially at cold seeps, where large amounts of methane bypass the sedimentary microbial methane sink as bubbles, the role of pelagic methane oxidation in reducing the methane emission from the ocean into the atmosphere becomes even more important. However, the combination of short water residence times at most seep sites and the long doubling time of methanotrophs cannot explain the high abundances of methanotrophs often detected directly above the seep sites. Hence, scientists proposed a bentho-pelagic transport process for methanotrophs attached to gas bubbles released from the seabed into the water column to explain the observed abundances above seep sites (Schubert et al. 2006b). This transport process was first described in 2015 for a single seep site (Schmale et al. 2015) but left open questions about the parameters controlling the transportation efficiency, the identity of the transported microorganisms, their survival and activity in the water column, and effect on the pelagic methane sink.

The bubble catching experiments conducted in this thesis at the Coal Oil Point seep field, California, provide an insight into the factors controlling the bentho-pelagic exchange of methanotrophs via gas bubbles. These experiments showed that the transport efficiency of the methanotrophs at single gas vents depend on the volumetric gas flow. Specifically, an increase in bubble flux decreases the transport efficiency while the bubble size does not significantly influence the transport process. However, the difference in seep intensities was reduced by higher vent density, so that the most intense seep site, which had also the highest vent density, transported the most MOB per square meter per day.

The bubble-mediated link between the benthic and pelagic environments was further supported by genetic analyses. The comparison of sediment, water column, and the Bubble Catcher microbial communities, made it possible to assign the transported sequences to the methanotrophic family *Methylomonaceae*. Furthermore, this genetic analysis of the captured seep bubbles from the Coal Oil Point seep field suggested the transport of benthic oil degrading bacteria assigned to the genus *Cycloclasticus* into the water column, which could increase the pelagic microbial degradation of oil. This leads to the hypothesis that, in addition to methanotrophs and oil degrading bacteria, other microorganisms are subject to dislocation by the bubble-mediated transport process. These transported microorganisms inoculate the water column, influence the pelagic microbial community, and could also affect pelagic biogeochemical processes in the vicinity of gas seeps.

The subsequent survival and activity of benthic methanotrophs in the water column was shown by incubation of Bubble Catcher sample water. The conducted experiments indicated an increase of the methanotrophs' abundances as well as prolonged methanotrophic activity over

a period of three weeks, suggesting the survival of the benthic methanotrophs after dislocation from their natural environment.

The pelagic methane turnover at highly active seeps is controlled by environmental factors such as methane availability (Crespo-Medina et al. 2014), differential circulation patterns (Steinle et al. 2015), and redox conditions (Kessler et al. 2011). The results presented in this thesis demonstrate that, apart from these factors, the dislocation of benthic methanotrophs into the water column can spontaneously boost the methane oxidation capacity within the dispersing methane plume. This transport mechanism becomes even more critical at seep sites characterized by water residence times that are too short to allow the relatively slow-growing methanotrophic community to establish a resilient methane sink. However, *in situ* studies to investigate the survival and activity of benthic MOB as well as a potential shift in the microbial community composition in the ageing plume waters are necessary to complement the laboratory survival experiments of this thesis. In addition, future investigations should not be limited to the bentho-pelagic coupling of methanotrophs but should also look at other biogeochemical processes.

Even though the impact of environmental factors on MOB abundance and activity may vary between seep locations, one can contend that the bentho-pelagic transportation of methanotrophs causes a positive feedback on the pelagic methane sink by reducing methane turnover time and atmospheric flux.

7 References

Aben, R. C. H., N. Barros, E. van Donk, and others. 2017. Cross continental increase in methane ebullition under climate change. Nat. Commun. **8**: 1682. doi:10.1038/s41467-017-01535-y

Acinas, S. G., L. A. Marcelino, V. Klepac-Ceraj, and M. F. Polz. 2004. Divergence and redundancy of 16S rRNA sequences in genomes with multiple *rrn* operons. J. Bacteriol. **186**: 2629–2635. doi:10.1128/JB.186.9.2629-2635.2004

Algar, C. K., B. P. Boudreau, and M. A. Barry. 2011. Release of multiple bubbles from cohesive sediments. Geophys. Res. Lett. **38**: 2–5. doi:10.1029/2011GL046870

Aloisi, G., I. Bouloubassi, S. Heijs, and others. 2002. CH_4-consuming microorganisms and the formation of carbonate crusts at cold seeps. Earth Planet. Sci. Lett. **203**: 195–203. doi:10.1016/S0012-821X(02)00878-6

Amann, R. I., B. J. Binder, R. J. Olson, S. W. Chisholm, R. Devereux, and D. A. Stahl. 1990. Combination of 16S rRNA-targeted oligonucleotide probes with flow cytometry for analyzing mixed microbial populations. Appl. Environ. Microbiol. **56**: 1919–1925. doi:10.1128/aem.56.6.1919-1925.1990

de Angelis, M. A. A., M. D. D. Lilley, and J. A. A. Baross. 1993. Methane oxidation in deep-sea hydrothermal plumes of the endeavour segment of the Juan de Fuca Ridge. Deep Sea Res. Part I Oceanogr. Res. Pap. **40**: 1169–1186. doi:10.1016/0967-0637(93)90132-M

Auman, A. J., and M. E. Lidstrom. 2002. Analysis of sMMO-containing Type I methanotrophs in Lake Washington sediment. Environ. Microbiol. **4**: 517–524. doi:10.1046/j.1462-2920.2002.00323.x

Bakkaloglu, S., D. Lowry, R. E. Fisher, M. Menoud, M. Lanoisellé, H. Chen, T. Röckmann, and E. G. Nisbet. 2022. Stable isotopic signatures of methane from waste sources through atmospheric measurements. Atmos. Environ. **276**. 119021 doi:10.1016/j.atmosenv. 2022.119021

Bauer, R. K., U. Gräwe, D. Stepputtis, C. Zimmermann, and C. Hammer. 2014. Identifying the location and importance of spawning sites of Western Baltic herring using a particle backtracking model. ICES J. Mar. Sci. **71**: 499–509. doi:10.1093/icesjms/fst163

Bauer, R. K., D. Stepputtis, U. Gräwe, C. Zimmermann, and C. Hammer. 2013. Wind-induced variability in coastal larval retention areas: a case study on Western Baltic spring-spawning herring. Fish. Oceanogr. **22**: 388–399. doi:10.1111/fog.12029

Bertagnolli, A., A. Treusch, O. Mason, U. Stingl, K. Vergin, F. Chan, B. Beszteri, and S. Giovannoni. 2011. Bacterial diversity in the bottom boundary layer of the inner continental shelf of Oregon, USA. Aquat. Microb. Ecol. **64**: 15–25. doi:10.3354/ame01504

Bezdek, H. F., and A. F. Carlucci. 1972. Surface Concentration of Marine Bacteria. Limnol. Oceanogr. **17**: 566–569. doi:10.4319/lo.1972.17.4.0566

Boetius, A., K. Ravenschlag, C. J. Schubert, and others. 2000. A marine microbial consortium apparently mediating anaerobic oxidation of methane. Nature **407**: 623–626. doi:10.1038/35036572

Boetius, A., and F. Wenzhöfer. 2013. Seafloor oxygen consumption fuelled by methane from cold seeps. Nat. Geosci. **6**: 725–734. doi:10.1038/ngeo1926

Boudreau, B. P., C. K. Algar, B. D. Johnson, and others. 2005. Bubble growth and rise in soft sediments. Geology **33**: 517. doi:10.1130/G21259.1

Bourne, D. G., I. R. McDonald, and J. C. Murrell. 2001. Comparison of *pmoA* PCR primer sets as tools for investigating methanotroph diversity in three Danish soils. Appl. Environ. Microbiol. **67**: 3802–3809. doi:10.1128/AEM.67.9.3802-3809.2001

Bousquet, P., P. Ciais, J. B. Miller, and others. 2006. Contribution of anthropogenic and natural sources to atmospheric methane variability. Nature **443**: 439–443. doi:10.1038/nature 05132

Bussmann, I., A. Matousu, R. Osudar, and S. Mau. 2015. Assessment of the radio ^{3}H-CH_4 tracer technique to measure aerobic methane oxidation in the water column. Limnol. Oceanogr. Methods **13**: 312–327. doi:10.1002/lom3.10027

Callahan, B. J., P. J. McMurdie, M. J. Rosen, A. W. Han, A. J. A. Johnson, and S. P. Holmes. 2016. DADA2: High-resolution sample inference from Illumina amplicon data. Nat. Methods **13**: 581–583. doi:10.1038/nmeth.3869

Chan, E. W., A. M. Shiller, D. J. Joung, and others. 2019. Investigations of aerobic methane oxidation in two marine seep environments: Part 1—Chemical kinetics. J. Geophys. Res. Ocean. **124**: 8852–8868. doi:10.1029/2019JC015594

Clark, J. F., L. Washburn, J. S. Hornafius, and B. P. Luyendyk. 2000. Dissolved hydrocarbon flux from natural marine seeps to the southern California Bight. J. Geophys. Res. Ocean. **105**: 11509–11522. doi:10.1029/2000JC000259

Clift, R., J. R. Grace, and M. E. Weber. 1978. Bubbles, Drops, and Particles.

Costello, A. M., and M. E. Lidstrom. 1999. Molecular characterization of functional and phylogenetic genes from natural populations of methanotrophs in lake sediments. Appl. Environ. Microbiol. **65**: 5066–5074.

Crespo-Medina, M., C. D. Meile, K. S. Hunter, and others. 2014. The rise and fall of methanotrophy following a deepwater oil-well blowout. Nat. Geosci. **7**: 423–427. doi:10. 1038/ngeo2156

Cunliffe, M., A. Engel, S. Frka, and others. 2013. Sea surface microlayers: A unified physicochemical and biological perspective of the air–ocean interface. Prog. Oceanogr. **109**: 104–116. doi:10.1016/j.pocean.2012.08.004

Daims, H., A. Brühl, R. Amann, K.-H. Schleifer, and M. Wagner. 1999. The domain-specific probe EUB338 is insufficient for the detection of all bacteria: Development and evaluation of a more comprehensive probe set. Syst. Appl. Microbiol. **22**: 434–444. doi:10.1016/S0723-2020(99)80053-8

Damm, E., E. Helmke, S. Thoms, U. Schauer, E. Nöthig, K. Bakker, and R. P. Kiene. 2010. Methane production in aerobic oligotrophic surface water in the central Arctic Ocean. Biogeosciences **7**: 1099–1108. doi:10.5194/bg-7-1099-2010

Dando, P. R., S. Aliani, H. Arab, and others. 2000. Hydrothermal studies in the Aegean Sea. Phys. Chem. Earth, Part B Hydrol. Ocean. Atmos. **25**: 1–8. doi:10.1016/S1464-1909 (99)00112-4

Deng, Y., X. Cui, C. Lüke, and M. G. Dumont. 2013. Aerobic methanotroph diversity in Riganqiao peatlands on the Qinghai-Tibetan Plateau. Environ. Microbiol. Rep. **5**: 566–574. doi:10.1111/1758-2229.12046

Deutzmann, J. S., M. Hoppert, and B. Schink. 2014. Characterization and phylogeny of a novel methanotroph, *Methyloglobulus morosus* gen. nov., spec. nov. Syst. Appl. Microbiol. **37**: 165–169. doi:10.1016/j.syapm.2014.02.001

Dubilier, N., C. Bergin, and C. Lott. 2008. Symbiotic diversity in marine animals: the art of harnessing chemosynthesis. Nat. Rev. Microbiol. **6**: 725–740. doi:10.1038/nrmicro1992

Dumestre, J. F., J. Guézennec, C. Galy-Lacaux, R. Delmas, S. Richard, and L. Labroue. 1999. Influence of light intensity on methanotrophic bacterial activity in Petit Saut Reservoir, French Guiana. Appl. Environ. Microbiol. **65**: 534–9. doi:10.1128/AEM.65.2.534-539.1999

Dunfield, P. F., A. Yuryev, P. Senin, and others. 2007. Methane oxidation by an extremely acidophilic bacterium of the phylum Verrucomicrobia. **450**: 879–883. doi:10.1038/nature06411

Durisch-Kaiser, E., L. Klauser, B. Wehrli, and C. Schubert. 2005. Evidence of intense archaeal and bacterial methanotrophic activity in the Black Sea water column. Appl. Environ. Microbiol. **71**: 8099–8106. doi:10.1128/AEM.71.12.8099-8106.2005

Dutaur, L., and L. V. Verchot. 2007. A global inventory of the soil CH_4 sink. Global Biogeochem. Cycles **21**: 1–9. doi:10.1029/2006GB002734

Ehhalt, D. H. 1974. The atmospheric cycle of methane. Tellus **26**: 58–70. doi:10.3402/tellusa.v26i1-2.9737

Eller, G., S. Stubner, and P. Frenzel. 2001. Group-specific 16S rRNA targeted probes for the detection of type I and type II methanotrophs by fluorescence in situ hybridisation. FEMS Microbiol. Lett. **198**: 91–97. doi:10.1111/j.1574-6968.2001.tb10624.x

EPA. 2016. Inventory of US greenhouse gas emissions and sinks: 1990-2014.

Ferguson, D. M., D. F. Moore, M. A. Getrich, and M. H. Zhowandai. 2005. Enumeration and speciation of enterococci found in marine and intertidal sediments and coastal water in southern California. J. Appl. Microbiol. **99**: 598–608. doi:10.1111/j.1365-2672.2005.02660.x

Fischer, J. P. 1978. Oil and tar seeps, Santa Barbara basin, California, p. 1–62. *In* California Offshore Gas, Oil and Tar Seeps. California State Lands Commission.

Forehead, H., P. Thomson, and G. A. Kendrick. 2013. Shifts in composition of microbial communities of subtidal sandy sediments maximise retention of nutrients. FEMS Microbiol. Ecol. **83**: 279–298. doi:10.1111/j.1574-6941.2012.01472.x

Garstecki, T., S. A. Wickham, and H. Arndt. 2002. Effects of experimental sediment resuspension on a coastal planktonic microbial food web. Estuar. Coast. Shelf Sci. **55**: 751–762. doi:10.1006/ecss.2001.0937

Goffredi, S. K., E. Tilic, S. W. Mullin, and others. 2020. Methanotrophic bacterial symbionts fuel dense populations of deep-sea feather duster worms (Sabellida, Annelida) and extend the spatial influence of methane seepage. Sci. Adv. **6**. doi:10.1126/sciadv.aay8562

Gräwe, U., P. Holtermann, K. Klingbeil, and H. Burchard. 2015. Advantages of vertically adaptive coordinates in numerical models of stratified shelf seas. Ocean Model. **92**: 56–68. doi:10.1016/j.ocemod.2015.05.008

Greinert, J., Y. Artemov, V. Egorov, M. Debatist, and D. McGinnis. 2006. 1300-m-high rising bubbles from mud volcanoes at 2080m in the Black Sea: Hydroacoustic characteristics and temporal variability. Earth Planet. Sci. Lett. **244**: 1–15. doi:10.1016/j.epsl.2006.02.011

Grossart, H.-P., K. Frindte, C. Dziallas, W. Eckert, and K. W. Tang. 2011. Microbial methane production in oxygenated water column of an oligotrophic lake. Proc. Natl. Acad. Sci. **108**: 19657–19661. doi:10.1073/pnas.1110716108

Guizien, K., C. Dupuy, P. Ory, H. Montanié, H. Hartmann, M. Chatelain, and M. Karpytchev. 2014. Microorganism dynamics during a rising tide: Disentangling effects of resuspension and mixing with offshore waters above an intertidal mudflat. J. Mar. Syst. **129**: 178–188. doi:10.1016/j.jmarsys.2013.05.010

Gutierrez, T., D. Berry, A. Teske, and M. Aitken. 2016. Enrichment of fusobacteria in sea surface oil slicks from the Deepwater Horizon oil spill. Microorganisms **4**: 24. doi:10.3390/microorganisms4030024

Haeckel, M., B. P. Boudreau, and K. Wallmann. 2007. Bubble-induced porewater mixing: A 3-D model for deep porewater irrigation. Geochim. Cosmochim. Acta **71**: 5135–5154. doi:10.1016/j.gca.2007.08.011

Hazen, T. C., R. C. Prince, and N. Mahmoudi. 2016. Marine oil biodegradation. Environ. Sci. Technol. **50**: 2121–2129. doi:10.1021/acs.est.5b03333

Heintz, M. B., S. Mau, and D. L. Valentine. 2012. Physical control on methanotrophic potential in waters of the Santa Monica Basin, Southern California. Limnol. Oceanogr. **57**: 420–432. doi:10.4319/lo.2012.57.2.0420

Herlemann, D. P. R., M. Labrenz, K. Jürgens, S. Bertilsson, J. J. Waniek, and A. F. Andersson. 2011. Transitions in bacterial communities along the 2000 km salinity gradient of the Baltic Sea. ISME J. **5**: 1571–1579. doi:10.1038/ismej.2011.41

Heyer, J., V. F. Galchenko, and P. F. Dunfield. 2002. Molecular phylogeny of type II methane-oxidizing bacteria isolated from various environments. Microbiology **148**: 2831–2846. doi:10.1099/00221287-148-9-2831

Hickey, B. M. 1992. Circulation over the Santa Monica-San Pedro Basin and Shelf. Prog. Oceanogr. **30**: 37–115. doi:10.1016/0079-6611(92)90009-O

Hindson, B. J., K. D. Ness, D. A. Masquelier, and others. 2011. High-throughput droplet digital PCR system for absolute quantitation of DNA copy number. Anal. Chem. **83**: 8604–8610. doi:10.1021/ac202028g

Hirayama, H., M. Abe, M. Miyazaki, T. Nunoura, Y. Furushima, H. Yamamoto, and K. Takai. 2014. *Methylomarinovum caldicuralii* gen. nov., sp. nov., a moderately thermophilic methanotroph isolated from a shallow submarine hydrothermal system, and proposal of the family *Methylothermaceae* fam. nov. Int. J. Syst. Evol. Microbiol. **64**: 989–999. doi:10.1099/ijs.0.058172-0

von Hoffmann, A. W. 1866. Introduction to modern chemistry, experimental and theoretic. Fortnightly **3**.

Holmes, A. J., A. Costello, M. E. Lidstrom, and J. C. Murrell. 1995a. Evidence that participate methane monooxygenase and ammonia monooxygenase may be evolutionarily related. FEMS Microbiol. Lett. **132**: 203–208. doi:10.1111/j.1574-6968.1995.tb07834.x

Holmes, A. J., N. J. P. Owens, and J. C. Murrell. 1995b. Detection of novel marine methanotrophs using phylogenetic and functional gene probes after methane enrichment. Microbiology **141**: 1947–1955. doi:10.1099/13500872-141-8-1947

Holmes, M. E., F. J. Sansone, T. M. Rust, and B. N. Popp. 2000. Methane production, consumption, and air-sea exchange in the open ocean: An evaluation based on carbon isotopic ratios. Global Biogeochem. Cycles **14**: 1–10. doi:10.1029/1999GB001209

Hornafius, J. S., D. Quigley, and B. P. Luyendyk. 1999. The world's most spectacular marine hydrocarbon seeps (Coal Oil Point, Santa Barbara Channel, California): Quantification of emissions. J. Geophys. Res. Ocean. **104**: 20703–20711. doi:10.1029/1999JC900148

Horz, H.-P., M. T. Yimga, and W. Liesack. 2001. Detection of Methanotroph Diversity on Roots of Submerged Rice Plants by Molecular Retrieval of *pmoA*, *mmoX*, *mxaF*, and 16S rRNA and Ribosomal DNA, Including *pmoA*-Based Terminal Restriction Fragment Length Polymorphism Profiling. Appl. Environ. Microbiol. **67**: 4177–4185. doi:10.1128/AEM.67.9.4177-4185.2001

Hu, W., K. Murata, S. Fukuyama, Y. Kawai, E. Oka, M. Uematsu, and D. Zhang. 2017. Concentration and viability of airborne bacteria over the Kuroshio extension region in the northwestern pacific ocean: Data from three cruises. J. Geophys. Res. Atmos. **122**: 12,892-12,905. doi:10.1002/2017JD027287

Hunt, J. M. 1995. Petroleum geochemistry and geology, 2nd ed. W.H. Freeman.

Jacobs, E., H. C. Bittig, U. Gräwe, C. A. Graves, M. Glockzin, J. D. Müller, B. Schneider, and G. Rehder. 2021. Upwelling-induced trace gas dynamics in the Baltic Sea inferred from 8 years of autonomous measurements on a ship of opportunity. Biogeosciences **18**: 2679–2709. doi:10.5194/bg-18-2679-2021

Jakobs, G., P. Holtermann, C. Berndmeyer, G. Rehder, M. Blumenberg, G. Jost, G. Nausch, and O. Schmale. 2014. Seasonal and spatial methane dynamics in the water column of the central Baltic Sea (Gotland Sea). Cont. Shelf Res. **91**: 12–25. doi:10.1016/j.csr.2014.07.005

Jamieson, R. C., D. M. Joy, H. Lee, R. Kostaschuk, and R. J. Gordon. 2005. Resuspension of sediment-associated *Escherichia coli* in a Natural Stream. J. Environ. Qual. **34**: 581–589. doi:10.2134/jeq2005.0581

Jang, H., R. Rusconi, and R. Stocker. 2017. Biofilm disruption by an air bubble reveals heterogeneous age-dependent detachment patterns dictated by initial extracellular matrix distribution. npj Biofilms Microbiomes **3**: 1–6. doi:10.1038/s41522-017-0014-5

Jessen, G. L., S. Pantoja, M. A. Gutiérrez, R. A. Quiñones, R. R. González, J. Sellanes, M. Y. Kellermann, and K.-U. Hinrichs. 2011. Methane in shallow cold seeps at Mocha Island off central Chile. Cont. Shelf Res. **31**: 574–581. doi:10.1016/j.csr.2010.12.012

Jordan, S. F. A., U. Gräwe, T. Treude, E. M. Lee, J. Schneider von Deimling, G. Rehder, and O. Schmale. 2021. Pelagic methane sink enhanced by benthic methanotrophs ejected from a gas seep. Geophys. Res. Lett. **48**. e2021GL094819. doi:10.1029/2021GL094819

Jordan, S. F. A., T. Treude, I. Leifer, R. Janßen, J. Werner, H. Schulz-Vogt, and O. Schmale. 2020. Bubble-mediated transport of benthic microorganisms into the water column: Identification of methanotrophs and implication of seepage intensity on transport efficiency. Sci. Rep. **10**: 4682. doi:10.1038/s41598-020-61446-9

Judd, A., G. Davies, J. Wilson, R. Holmes, G. Baron, and I. Bryden. 1997. Contributions to atmospheric methane by natural seepages on the UK continental shelf. Mar. Geol. **137**: 165–189.

Judd, A. G. 2003. The global importance and context of methane escape from the seabed. Geo-Marine Lett. **23**: 147–154. doi:10.1007/s00367-003-0136-z

Judd, A. G. 2004. Natural seabed gas seeps as sources of atmospheric methane. Environ. Geol. **46**: 988–996. doi:10.1007/s00254-004-1083-3

Judd, A., and M. Hovland. 2007. Seabed Fluid Flow, Cambridge University Press.

Kai, F. M., S. C. Tyler, J. T. Randerson, and D. R. Blake. 2011. Reduced methane growth rate explained by decreased Northern Hemisphere microbial sources. Nature **476**: 194–197. doi:10.1038/nature10259

Kallistova, A. Y., A. Y. Merkel, I. Y. Tarnovetskii, and N. V. Pimenov. 2017. Methane formation and oxidation by prokaryotes. Microbiology **86**: 671–691. doi:10.1134/S0026261717060091

Kalyuzhnaya, M. G., O. A. Gomez, and J. C. Murrell. 2019. The methane-oxidizing bacteria (methanotrophs), p. 245–278. *In* Taxonomy, Genomics and Ecophysiology of Hydrocarbon-Degrading Microbes. Springer International Publishing.

Kalyuzhnaya, M. G., V. Khmelenina, B. Eshinimaev, D. Sorokin, H. Fuse, M. Lidstrom, and Y. Trotsenko. 2008. Classification of halo(alkali)philic and halo(alkali)tolerant methanotrophs provisionally assigned to the genera *Methylomicrobium* and *Methylobacter* and emended description of the genus *Methylomicrobium*. Int. J. Syst. Evol. Microbiol. **58**: 591–596. doi:10.1099/ijs.0.65317-0

Kaserer, H. 1905. Über die Oxydation des Wasserstoffes und des Methans durch Mikroorganismen, Hartleben.

Keir, R. S., J. Sültenfuß, M. Rhein, G. Petrick, and J. Greinert. 2006. Separation of ^{3}He and CH_4 signals on the Mid-Atlantic Ridge at 5°N and 51°N. Geochim. Cosmochim. Acta **70**: 5766–5778. doi:10.1016/j.gca.2006.06.005

Kelley, D. S., J. A. Karson, G. L. Früh-Green, and others. 2005. A serpentinite-hosted ecosystem: The Lost City hydrothermal field. Science. **307**: 1428–1434. doi:10.1126/science.1102556

Kersten, M., T. Leipe, and F. Tauber. 2005. Storm disturbance of sediment contaminants at a hot-spot in the Baltic Sea assessed by ^{234}Th radionuclide tracer profiles. Environ. Sci. Technol. **39**: 984–990. doi:10.1021/es049391y

Kessler, J. D., D. L. Valentine, M. C. Redmond, and others. 2011. A persistent oxygen anomaly reveals the fate of spilled methane in the deep Gulf of Mexico. Science. **331**: 312–315. doi:10.1126/science.1199697

Kharitonov, S., M. Semenov, A. Sabrekov, O. Kotsyurbenko, A. Zhelezova, and N. Schegolkova. 2021. Microbial communities in methane cycle: Modern molecular methods gain insights into their global ecology. Environments **8**: 16. doi:10.3390/environments8020016

Kinnaman, F. S., J. B. Kimball, L. Busso, D. Birgel, H. Ding, K. U. Hinrichs, and D. L. Valentine. 2010. Gas flux and carbonate occurrence at a shallow seep of thermogenic natural gas. Geo-Marine Lett. **30**: 355–365. doi:10.1007/s00367-010-0184-0

Kleindienst, S., S. Grim, M. Sogin, A. Bracco, M. Crespo-Medina, and S. B. Joye. 2016. Diverse, rare microbial taxa responded to the Deepwater Horizon deep-sea hydrocarbon plume. ISME J. **10**: 400–415. doi:10.1038/ismej.2015.121

Klingbeil, K., and H. Burchard. 2013. Implementation of a direct nonhydrostatic pressure gradient discretisation into a layered ocean model. Ocean Model. **65**: 64–77. doi:10.1016/j.ocemod.2013.02.002

Knief, C. 2015. Diversity and habitat preferences of cultivated and uncultivated aerobic methanotrophic bacteria evaluated based on *pmoA* as molecular marker. Front. Microbiol. **6**. doi:10.3389/fmicb.2015.01346

Knittel, K., and A. Boetius. 2009. Anaerobic oxidation of methane: Progress with an unknown process. Annu. Rev. Microbiol. **63**: 311–334. doi:10.1146/annurev.micro.61.080706.093130

Kozich, J. J., S. L. Westcott, N. T. Baxter, S. K. Highlander, and P. D. Schloss. 2013. Development of a dual-index sequencing strategy and curation pipeline for analyzing amplicon sequence data on the MiSeq Illumina sequencing platform. Appl. Environ. Microbiol. **79**: 5112–5120. doi:10.1128/AEM.01043-13

Lai, Q., W. Li, B. Wang, Z. Yu, and Z. Shao. 2012. Complete genome sequence of the pyrene-degrading bacterium *Cycloclasticus* sp. strain P1. J. Bacteriol. **194**: 6677–6677. doi:10.1128/JB.01837-12

Law, C. S., S. D. Nodder, J. J. Mountjoy, A. Marriner, A. Orpin, C. A. Pilditch, P. Franz, and K. Thompson. 2010. Geological, hydrodynamic and biogeochemical variability of a New Zealand deep-water methane cold seep during an integrated three-year time-series study. Mar. Geol. **272**: 189–208. doi:10.1016/j.margeo.2009.06.018

Leifer, I. 2010. Characteristics and scaling of bubble plumes from marine hydrocarbon seepage in the Coal Oil Point seep field. J. Geophys. Res. **115**: C11014. doi:10.1029/2009JC005844

Leifer, I. 2015. Seabed bubble flux estimation by calibrated video survey for a large blowout seep in the North Sea. Mar. Pet. Geol. **68**: 743–752. doi:10.1016/j.marpetgeo.2015.08.032

Leifer, I. 2017. Life aquatic chemosynthetic in the photic zone-Up the food chain? Oceanogr. Fish. Open access J. **4**: 1–4. doi:10.19080/OFOAJ.2017.04.555636

Leifer, I. 2019. A synthesis review of emissions and fates for the Coal Oil Point marine hydrocarbon seep field and California marine seepage. Geofluids **2019**: 1–48. doi:10.1155/2019/4724587

Leifer, I., and J. Boles. 2005. Measurement of marine hydrocarbon seep flow through fractured rock and unconsolidated sediment. Mar. Pet. Geol. **22**: 551–568. doi:10.1016/j.marpetgeo.2004.10.026

Leifer, I., and J. Clark. 2002. Modeling trace gases in hydrocarbon seep bubbles. Application to marine hydrocarbon seeps in the Santa Barbara channel. Geol. i Geofiz. **43**: 613–621.

Leifer, I., J. F. Clark, and R. F. Chen. 2000. Modifications of the local environment by natural marine hydrocarbon seeps. Geophys. Res. Lett. **27**: 3711–3714. doi:10.1029/2000GL011619

Leifer, I., and D. Culling. 2010. Formation of seep bubble plumes in the Coal Oil Point seep field. Geo-Marine Lett. **30**: 339–353. doi:10.1007/s00367-010-0187-x

Leifer, I., H. Jeuthe, S. H. Gjøsund, and V. Johansen. 2009. Engineered and Natural Marine Seep, Bubble-Driven Buoyancy Flows. J. Phys. Oceanogr. **39**: 3071–3090. doi:10.1175/2009JPO4135.1

Leifer, I., and A. Judd. 2015. The UK22/4b blowout 20 years on: Investigations of continuing methane emissions from sub-seabed to the atmosphere in a North Sea context. Mar. Pet. Geol. **68**: 706–717. doi:10.1016/j.marpetgeo.2015.11.012

Leifer, I., M. J. Kamerling, B. P. Luyendyk, and D. S. Wilson. 2010. Geologic control of natural marine hydrocarbon seep emissions, Coal Oil Point seep field, California. Geo-Marine Lett. **30**: 331–338. doi:10.1007/s00367-010-0188-9

Leifer, I., G. de Leeuw, and L. H. Cohen. 2003. Optical Measurement of Bubbles: System Design and Application. J. Atmos. Ocean. Technol. **20**: 1317–1332. doi:10.1175/1520-0426(2003)020<1317:OMOBSD>2.0.CO;2

Leifer, I., and R. K. Patro. 2002. The bubble mechanism for methane transport from the shallow sea bed to the surface: A review and sensitivity study. Cont. Shelf Res. **22**: 2409–2428. doi:10.1016/S0278-4343(02)00065-1

Leifer, I., E. Solomon, J. Schneider von Deimling, G. Rehder, R. Coffin, and P. Linke. 2015. The fate of bubbles in a large, intense bubble megaplume for stratified and unstratified water: Numerical simulations of 22/4b expedition field data. Mar. Pet. Geol. **68**: 806–823. doi:10.1016/j.marpetgeo.2015.07.025

Leifer, I., and D. Tang. 2007. The acoustic signature of marine seep bubbles. J. Acoust. Soc. Am. **121**: EL35–EL40. doi:10.1121/1.2401227

Leifer, I., and K. Wilson. 2007. The tidal influence on oil and gas emissions from an abandoned oil well: Nearshore Summerland, California. Mar. Pollut. Bull. **54**: 1495–1506. doi:10.1016/j.marpolbul.2007.03.014

Lenhart, K., T. Klintzsch, G. Langer, G. Nehrke, M. Bunge, S. Schnell, and F. Keppler. 2016. Evidence for methane production by the marine algae *Emiliania huxleyi*. Biogeosciences **13**: 3163–3174. doi:10.5194/bg-13-3163-2016

Levin, L. A., A. R. Baco, D. A. Bowden, and others. 2016. Hydrothermal vents and methane seeps: Rethinking the sphere of influence. Front. Mar. Sci. **3**: 1–23. doi:10.3389/fmars.2016.00072

Lohrberg, A., O. Schmale, I. Ostrovsky, H. Niemann, P. Held, and J. Schneider von Deimling. 2020. Discovery and quantification of a widespread methane ebullition event in a coastal inlet (Baltic Sea) using a novel sonar strategy. Sci. Rep. **10**: 1–13. doi:10.1038/s41598-020-60283-0

Lovley, D. R. 2017. Happy together: Microbial communities that hook up to swap electrons. ISME J. **11**: 327–336. doi:10.1038/ismej.2016.136

Luesken, F. A., B. Zhu, T. A. van Alen, and others. 2011. *pmoA* primers for detection of anaerobic methanotrophs. Appl. Environ. Microbiol. **77**: 3877–3880. doi:10.1128/AEM.02960-10

Magen, C., L. L. Lapham, J. W. Pohlman, K. Marshall, S. Bosman, M. Casso, and J. P. Chanton. 2014. A simple headspace equilibration method for measuring dissolved methane. Limnol. Oceanogr. Methods **12**: 637–650. doi:10.4319/lom.2014.12.637

Malhotra, R., B. Dhawan, B. Garg, V. Shankar, and T. Nag. 2019. A comparison of bacterial adhesion and biofilm formation on commonly used orthopaedic metal implant materials: An *In vitro* study. Indian J. Orthop. **53**: 148. doi:10.4103/ortho.IJOrtho_66_18

Matveeva, T., A. S. Savvichev, A. Semenova, E. Logvina, A. N. Kolesnik, and A. A. Bosin. 2015. Source, origin, and spatial distribution of shallow sediment methane in the Chukchi Sea. Oceanography **28**: 202–217. doi:10.5670/oceanog.2015.66

Mau, S., M. B. Heintz, F. S. Kinnaman, and D. L. Valentine. 2010. Compositional variability and air-sea flux of ethane and propane in the plume of a large, marine seep field near Coal Oil Point, CA. Geo-Marine Lett. **30**: 367–378. doi:10.1007/s00367-010-0185-z

Mau, S., M. B. Heintz, and D. L. Valentine. 2012. Quantification of CH_4 loss and transport in dissolved plumes of the Santa Barbara Channel, California. Cont. Shelf Res. **32**: 110–120. doi:10.1016/j.csr.2011.10.016

Mau, S., D. L. Valentine, J. F. Clark, J. Reed, R. Camilli, and L. Washburn. 2007. Dissolved methane distributions and air-sea flux in the plume of a massive seep field, Coal Oil Point, California. Geophys. Res. Lett. **34**: L22603. doi:10.1029/2007GL031344

McDonald, I. R., L. Bodrossy, Y. Chen, and J. C. Murrell. 2008. Molecular Ecology Techniques for the study of aerobic methanotrophs. Appl. Environ. Microbiol. **74**: 1305–1315. doi:10.1128/AEM.02233-07

McGinnis, D. F., J. Greinert, Y. Artemov, S. E. Beaubien, and A. Wüest. 2006. Fate of rising methane bubbles in stratified waters: How much methane reaches the atmosphere? J. Geophys. Res. **111**: C09007. doi:10.1029/2005JC003183

McMurdie, P. J., and S. Holmes. 2013. phyloseq: An R package for reproducible interactive analysis and graphics of microbiome census data. PLoS One **8**: e61217. doi:10.1371/journal.pone.0061217

Messina, E., R. Denaro, F. Crisafi, and others. 2016. Genome sequence of obligate marine polycyclic aromatic hydrocarbons-degrading bacterium *Cycloclasticus* sp. 78-ME, isolated from petroleum deposits of the sunken tanker Amoco Milford Haven, Mediterranean Sea. Mar. Genomics **25**: 11–13. doi:10.1016/j.margen.2015.10.006

Michaud, J. M., L. R. Thompson, D. Kaul, and others. 2018. Taxon-specific aerosolization of bacteria and viruses in an experimental ocean-atmosphere mesocosm. Nat. Commun. **9**. doi:10.1038/s41467-018-04409-z

Milucka, J., T. G. Ferdelman, L. Polerecky, and others. 2012. Zero-valent sulphur is a key intermediate in marine methane oxidation. Nature **491**: 541–546. doi:10.1038/nature11656

Murase, J., and A. Sugimoto. 2005. Inhibitory effect of light on methane oxidation in the pelagic water column of a mesotrophic lake (Lake Biwa, Japan). Limnol. Oceanogr. **50**: 1339–1343. doi:10.4319/lo.2005.50.4.1339

Murrell, J. C. 2010. The aerobic methane oxidizing bacteria (methanotrophs), p. 1953–1966. *In* K.N. Timmis [ed.], Handbook of Hydrocarbon and Lipid Microbiology. Springer Berlin Heidelberg.

Myhre, G., D. Shindell, F.-M. Bréon, and others. 2014. Anthropogenic and natural radiative forcing, p. 659–740. *In* Intergovernmental Panel on Climate Change [ed.], Climate Change 2013 - The Physical Science Basis. Cambridge University Press.

Nauw, J., H. de Haas, and G. Rehder. 2015a. A review of oceanographic and meteorological controls on the North Sea circulation and hydrodynamics with a view to the fate of North Sea methane from well site 22/4b and other seabed sources. Mar. Pet. Geol. **68**: 861–882. doi:10.1016/j.marpetgeo.2015.08.007

Nauw, J., P. Linke, and I. Leifer. 2015b. Bubble momentum plume as a possible mechanism for an early breakdown of the seasonal stratification in the northern North Sea. Mar. Pet. Geol. **68**: 789–805. doi:10.1016/j.marpetgeo.2015.05.003

Nazaries, L., J. C. Murrell, P. Millard, L. Baggs, and B. K. Singh. 2013. Methane, microbes and models: Fundamental understanding of the soil methane cycle for future predictions. Environ. Microbiol. **15**: 2395–2417. doi:10.1111/1462-2920.12149

Niemann, H., P. Linke, K. Knittel, and others. 2013. Methane-carbon flow into the benthic food web at cold seeps - A case study from the Costa Rica subduction zone. PLoS One **8**: 4–13. doi:10.1371/journal.pone.0074894

Niemann, H., L. Steinle, J. Blees, I. Bussmann, T. Treude, S. Krause, M. Elvert, and M. F. Lehmann. 2015. Toxic effects of lab-grade butyl rubber stoppers on aerobic methane oxidation. Limnol. Oceanogr. Methods **13**: 40–52. doi:10.1002/lom3.10005

Nisbet, E. G., E. J. Dlugokencky, and P. Bousquet. 2014. Methane on the rise–Again. Science. **343**: 493–495. doi:10.1126/science.1247828

Olson, D. J. 1982. Surface and subsurface geology of the Santa Barbara-Goleta metropolitan area, Santa Barbara County, California. Masters Thesis.

Op den Camp, H. J. M., T. Islam, M. B. Stott, and others. 2009. Environmental, genomic and taxonomic perspectives on methanotrophic *Verrucomicrobia*. Environ. Microbiol. Rep. **1**: 293–306. doi:10.1111/j.1758-2229.2009.00022.x

Orvain, F., P. Le Hir, and P. Sauriau. 2003. A model of fluff layer erosion and subsequent bed erosion in the presence of the bioturbator, *Hydrobia ulvae*. J. Mar. Res. **61**: 821–849. doi:10.1357/002224003322981165

Oswald, K., J. Milucka, A. Brand, S. Littmann, B. Wehrli, M. M. M. Kuypers, and C. J. Schubert. 2015. Light-dependent aerobic methane oxidation reduces methane emissions from seasonally stratified lakes. 1–22. doi:10.1371/journal.pone.0132574

Parks, D. H., M. Chuvochina, D. W. Waite, C. Rinke, A. Skarshewski, P.-A. Chaumeil, and P. Hugenholtz. 2018. A standardized bacterial taxonomy based on genome phylogeny substantially revises the tree of life. Nat. Biotechnol. **36**: 996–1004. doi:10.1038/nbt.4229

Pawlowicz, R., B. Beardsley, and S. Lentz. 2002. Classical tidal harmonic analysis including error estimates in MATLAB using T_TIDE. Comput. Geosci. **28**: 929–937. doi:10.1016/S0098-3004(02)00013-4

Pernthaler, A., J. Pernthaler, and R. Amann. 2002. Fluorescence in situ hybridization and catalyzed reporter deposition for the identification of marine bacteria. Appl. Environ. Microbiol. **68**: 3094–3101. doi:10.1128/AEM.68.6.3094-3101.2002

Petersen, J. M., and N. Dubilier. 2009. Methanotrophic symbioses in marine invertebrates. Environ. Microbiol. Rep. **1**: 319–335. doi:10.1111/j.1758-2229.2009.00081.x

Picone, N., P. Blom, A. J. Wallenius, and others. 2021. *Methylacidimicrobium thermophilum* AP8, a novel methane- and hydrogen-oxidizing bacterium isolated from volcanic soil on Pantelleria Island, Italy. Front. Microbiol. **12**. doi:10.3389/fmicb.2021.637762

Powelson, D. K., and A. L. Mills. 1998. Water Saturation and surfactant efeccts on bacterial transport in sand columns. Soil Sci. **163**: 694–704. doi:10.1097/00010694-199809000-00003

Priestley, J. 1776. Experiments and observations on different kinds of air, 2nd ed. Johnson, J.

QGIS Development Team. 2022. QGIS Geographic Information System.

R Core Team. 2018. R: A language and environment for statistical computing.

Redmond, M. C., D. L. Valentine, and A. L. Sessions. 2010. Identification of novel methane-, ethane-, and propane-oxidizing bacteria at marine hydrocarbon seeps by stable isotope probing. Appl. Environ. Microbiol. **76**: 6412–6422. doi:10.1128/AEM.00271-10

Reeburgh, W. S. 2007. Oceanic methane biogeochemistry. Chem. Rev. **107**: 486–513. doi:10.1021/cr050362v

Regnier, P., A. W. Dale, S. Arndt, D. E. LaRowe, J. Mogollón, and P. Van Cappellen. 2011. Quantitative analysis of anaerobic oxidation of methane (AOM) in marine sediments: A modeling perspective. Earth-Science Rev. **106**: 105–130. doi:10.1016/j.earscirev.2011.01.002

Rehder, G., P. W. Brewer, E. T. Peltzer, and G. Friederich. 2002. Enhanced lifetime of methane bubble streams within the deep ocean. Geophys. Res. Lett. **29**: 21-1-21–4. doi:10.1029/2001GL013966

Rehder, G., R. S. Keir, E. Suess, and T. Pohlmann. 1998. The multiple sources and patterns of methane in North Sea waters. Aquat. Geochemistry **4**: 403–427. doi:10.1023/A:1009644600833

Rehder, G., R. S. Keir, E. Suess, and M. Rhein. 1999. Methane in the northern Atlantic controlled by microbial oxidation and atmospheric history. Geophys. Res. Lett. **26**: 587–590. doi:10.1029/1999GL900049

Repeta, D. J., S. Ferrón, O. A. Sosa, C. G. Johnson, L. D. Repeta, M. Acker, E. F. DeLong, and D. M. Karl. 2016. Marine methane paradox explained by bacterial degradation of dissolved organic matter. Nat. Geosci. **9**: 884–887. doi:10.1038/ngeo2837

Römer, M., M. Riedel, M. Scherwath, M. Heesemann, and G. D. Spence. 2016. Tidally controlled gas bubble emissions: A comprehensive study using long-term monitoring data from the NEPTUNE cabled observatory offshore Vancouver Island. Geochemistry, Geophys. Geosystems **17**: 3797–3814. doi:10.1002/2016GC006528

Rudd, J. W. M., A. Furutani, R. J. Flett, and R. D. Hamilton. 1976. Factors controlling methane oxidation in shield lakes: The role of nitrogen fixation and oxygen concentration1. Limnol. Oceanogr. **21**: 357–364. doi:10.4319/lo.1976.21.3.0357

Ruppel, C. D., and J. D. Kessler. 2017. The interaction of climate change and methane hydrates. Rev. Geophys. **55**: 126–168. doi:10.1002/2016RG000534

Russell, T. L., K. M. Yamahara, and A. B. Boehm. 2012. Mobilization and transport of naturally occurring enterococci in beach sands subject to transient infiltration of seawater. Environ. Sci. Technol. **46**: 5988–5996. doi:10.1021/es300408z

Sadhal, S. S., and R. E. Johnson. 1983. Stokes flow past bubbles and drops partially coated with thin films. Part 1. Stagnant cap of surfactant film - exact solution. J. Fluid Mech. **126**: 237–250. doi:10.1017/S0022112083000130

Saunois, M., P. Bousquet, B. Poulter, and others. 2016. The global methane budget 2000–2012. Earth Syst. Sci. Data **8**: 697–751. doi:10.5194/essd-8-697-2016

Saunois, M., P. Bousquet, B. Poulter, and others. 2017. Variability and quasi-decadal changes in the methane budget over the period 2000-2012. Atmos. Chem. Phys. **17**: 11135–11161. doi:10.5194/acp-17-11135-2017

Saunois, M., A. R. Stavert, B. Poulter, and others. 2020. The global methane budget 2000-2017. Earth Syst. Sci. Data **12**: 1561–1623. doi:10.5194/essd-12-1561-2020

Savvichev, A. S., V. V Kadnikov, A. Y. Kallistova, I. I. Rusanov, D. A. Voronov, E. D. Krasnova, and L. Bannoe. 2019. Light-dependent methane oxidation is the major process of the methane cycle in the water column of the Bol'shie Khruslomeny polar lake. **88**: 370–374. doi:10.1134/S002626171903010X

Schaefer, H., S. E. M. Fletcher, C. Veidt, and others. 2016. A 21st-century shift from fossil-fuel to biogenic methane emissions indicated by $^{13}CH_4$. Science. **352**: 80–84. doi:10.1126/science.aad2705

Schäfer, A., H. Harms, and A. J. B. Zehnder. 1998. Bacterial accumulation at the air-water interface. Environ. Sci. Technol. **32**: 3704–3712. doi:10.1021/es980191u

Schmale, O., S. E. E. Beaubien, G. Rehder, J. Greinert, and S. Lombardi. 2010. Gas seepage in the Dnepr paleo-delta area (NW-Black Sea) and its regional impact on the water column methane cycle. J. Mar. Syst. **80**: 90–100. doi:10.1016/j.jmarsys.2009.10.003

Schmale, O., M. Blumenberg, K. Kießlich, G. Jakobs, C. Berndmeyer, M. Labrenz, V. Thiel, and G. Rehder. 2012a. Aerobic methanotrophy within the pelagic redox-zone of the Gotland Deep (central Baltic Sea). Biogeosciences **9**: 4969–4977. doi:10.5194/bg-9-4969-2012

Schmale, O., S. Krause, P. Holtermann, N. C. Power Guerra, and L. Umlauf. 2016. Dense bottom gravity currents and their impact on pelagic methanotrophy at oxic/anoxic transition zones. Geophys. Res. Lett. **43**: 5225–5232. doi:10.1002/2016GL069032

Schmale, O., I. Leifer, J. S. Von Deimling, C. Stolle, S. Krause, K. Kießlich, A. Frahm, and T. Treude. 2015. Bubble Transport Mechanism: Indications for a gas bubble-mediated inoculation of benthic methanotrophs into the water column. Cont. Shelf Res. **103**: 70–78. doi:10.1016/j.csr.2015.04.022

Schmale, O., J. Wäge, V. Mohrholz, N. Wasmund, U. Gräwe, G. Rehder, M. Labrenz, and N. Loick-Wilde. 2018. The contribution of zooplankton to methane supersaturation in the oxygenated upper waters of the central Baltic Sea. Limnol. Oceanogr. **63**: 412–430. doi:10.1002/lno.10640

Schmale, O., M. Walter, J. Schneider von Deimling, J. Sültenfuß, S. Walker, G. Rehder, and R. Keir. 2012b. Fluid and gas fluxes from the Logatchev hydrothermal vent area. Geochemistry, Geophys. Geosystems **13**: Q07007. doi:10.1029/2012GC004158

Schneider, C. A., W. S. Rasband, and K. W. Eliceiri. 2012. NIH Image to ImageJ: 25 years of image analysis. Nat. Methods **9**: 671–5. doi:10.1038/nmeth.2089

Schneider von Deimling, J. 2017. Cruise Report R/V POSEIDON POS504-Seepage process analyses at the abandoned well Blowout site (22/4b, North Sea), 27.08. 2016–09.09. 2016 (Kiel-Kiel). Germany.

Schneider von Deimling, J., J. Greinert, N. R. Chapman, W. Rabbel, and P. Linke. 2010. Acoustic imaging of natural gas seepage in the North Sea: Sensing bubbles controlled by variable currents. Limnol. Oceanogr. Methods **8**: 155–171. doi:10.4319/lom.2010.8.155

Schneider von Deimling, J., P. Linke, M. Schmidt, and G. Rehder. 2015. Ongoing methane discharge at well site 22/4b (North Sea) and discovery of a spiral vortex bubble plume motion. Mar. Pet. Geol. **68**: 718–730. doi:10.1016/j.marpetgeo.2015.07.026

Schneider von Deimling, J., G. Rehder, J. Greinert, D. F. McGinnnis, A. Boetius, and P. Linke. 2011. Quantification of seep-related methane gas emissions at Tommeliten, North Sea. Cont. Shelf Res. **31**: 867–878. doi:10.1016/j.csr.2011.02.012

Schubert, C. J., M. J. L. Coolen, L. N. Neretin, and others. 2006a. Aerobic and anaerobic methanotrophs in the Black Sea water column. Environ. Microbiol. **8**: 1844–1856. doi:10.1111/j.1462-2920.2006.01079.x

Schubert, C. J., E. Durisch-Kaiser, C. P. Holzner, and others. 2006b. Methanotrophic microbial communities associated with bubble plumes above gas seeps in the Black Sea. Geochemistry, Geophys. Geosystems **7**: Q04002. doi:10.1029/2005GC001049

Schwietzke, S., O. A. Sherwood, L. M. P. Bruhwiler, and others. 2016. Upward revision of global fossil fuel methane emissions based on isotope database. Nature **538**: 88–91. doi:10.1038/nature19797

Semrau, J. D., A. A. DiSpirito, W. Gu, and S. Yoon. 2018. Metals and Methanotrophy I. Cann [ed.]. Appl. Environ. Microbiol. **84**: 7–14. doi:10.1128/AEM.02289-17

Shakhova, N., I. Semiletov, and E. Chuvilin. 2019. Understanding the permafrost–hydrate system and associated methane releases in the East Siberian Arctic Shelf. Geosci. **9**. doi:10.3390/geosciences9060251

Shakhova, N., I. Semiletov, I. Leifer, and others. 2014. Ebullition and storm-induced methane release from the East Siberian Arctic Shelf. Nat. Geosci. **7**: 64–70. doi:10.1038/ngeo2007

Shibata, T., H. M. Solo-Gabriele, L. E. Fleming, and S. Elmir. 2004. Monitoring marine recreational water quality using multiple microbial indicators in an urban tropical environment. Water Res. **38**: 3119–3131. doi:10.1016/j.watres.2004.04.044

Shimeta, J., C. L. Amos, S. E. Beaulieu, and O. M. Ashiru. 2002. Sequential resuspension of protists by accelerating tidal flow: Implications for community structure in the benthic boundary layer. Limnol. Oceanogr. **47**: 1152–1164. doi:10.4319/lo.2002.47.4.1152

Shrestha, P. M., C. Kammann, K. Lenhart, B. Dam, and W. Liesack. 2012. Linking activity, composition and seasonal dynamics of atmospheric methane oxidizers in a meadow soil. ISME J. **6**: 1115–1126. doi:10.1038/ismej.2011.179

Silyakova, A., P. Jansson, P. Serov, and others. 2020. Physical controls of dynamics of methane venting from a shallow seep area west of Svalbard. Cont. Shelf Res. **194**: 104030. doi:10.1016/j.csr.2019.104030

Smith, C. R., A. G. Glover, T. Treude, N. D. Higgs, and D. J. Amon. 2015. Whale-fall ecosystems: Recent insights into ecology, paleoecology, and evolution. Ann. Rev. Mar. Sci. **7**: 571–596. doi:10.1146/annurev-marine-010213-135144

Söhngen, N. L. 1906. Über Bakterien, welche Methan als Kohlenstoffnahrung und Energiequelle gebrauchen. Bakteriol Parasitenk Infekt. **15**: 513–517.

Sommer, S., M. Schmidt, and P. Linke. 2015. Continuous inline mapping of a dissolved methane plume at a blowout site in the Central North Sea UK using a membrane inlet mass spectrometer – Water column stratification impedes immediate methane release into the atmosphere. Mar. Pet. Geol. **68**: 766–775. doi:10.1016/j.marpetgeo.2015.08.020

Sommer, T., F. Danza, J. Berg, and others. 2017. Bacteria-induced mixing in natural waters. Geophys. Res. Lett. **44**: 9424–9432. doi:10.1002/2017GL074868

Stawiarski, B., S. Otto, V. Thiel, and others. 2019. Controls on zooplankton methane production in the central Baltic Sea. Biogeosciences **16**: 1–16. doi:10.5194/bg-16-1-2019

Steinle, L., C. A. Graves, T. Treude, and others. 2015. Water column methanotrophy controlled by a rapid oceanographic switch. Nat. Geosci. **8**: 378–382. doi:10.1038/ngeo2420

Steinle, L., J. Maltby, T. Treude, and others. 2017. Effects of low oxygen concentrations on aerobic methane oxidation in seasonally hypoxic coastal waters. Biogeosciences **14**: 1631–1645. doi:10.5194/bg-14-1631-2017

Steinle, L., M. Schmidt, L. Bryant, and others. 2016. Linked sediment and water-column methanotrophy at a man-made gas blowout in the North Sea: Implications for methane budgeting in seasonally stratified shallow seas. Limnol. Oceanogr. **61**: S367–S386. doi:10.1002/lno.10388

Stenstrom, T. A. 1989. Bacterial hydrophobicity, an overall parameter for the measurement of adhesion. **55**: 142–147. 10.1128/aem.55.1.142-147.1989

Stevens, H., T. Brinkhoff, and M. Simon. 2005. Composition of free-living, aggregate-associated and sediment surface-associated bacterial communities in the German Wadden Sea. Aquat. Microb. Ecol. **38**: 15–30. doi:10.3354/ame038015

Stoecker, K., B. Bendinger, B. Schöning, and others. 2006. Cohn's Crenothrix is a filamentous methane oxidizer with an unusual methane monooxygenase. Proc. Natl. Acad. Sci. **103**: 2363–2367. doi:10.1073/pnas.0506361103

Strong, P. J., M. Kalyuzhnaya, J. Silverman, and W. P. Clarke. 2016. A methanotroph-based biorefinery: Potential scenarios for generating multiple products from a single fermentation. Bioresour. Technol. **215**: 314–323. doi:10.1016/j.biortech.2016.04.099

Suess, E. 1980. Particulate organic carbon flux in the oceans - Surface productivity and oxygen utilization. Nature **288**: 260–263. doi:10.1038/288260a0

Suess, E. 2014. Marine cold seeps and their manifestations: geological control, biogeochemical criteria and environmental conditions. Int. J. Earth Sci. **103**. doi:10.1007/s00531-014-1010-0

Tavormina, P. L., W. Ussler, and V. J. Orphan. 2008. Planktonic and sediment-associated aerobic methanotrophs in two seep systems along the North American Margin. Appl. Environ. Microbiol. **74**: 3985–3995. doi:10.1128/AEM.00069-08

van Teeseling, M. C. F., A. Pol, H. R. Harhangi, S. van der Zwart, M. S. M. Jetten, H. J. M. Op den Camp, and L. van Niftrik. 2014. Expanding the Verrucomicrobial methanotrophic world: Description of three novel species of *Methylacidimicrobium* gen. nov. H.L. Drake [ed.]. Appl. Environ. Microbiol. **80**: 6782–6791. doi:10.1128/AEM.01838-14

Teske, A., K. U. Hinrichs, V. Edgcomb, A. De Vera Gomez, D. Kysela, S. P. Sylva, M. L. Sogin, and H. W. Jannasch. 2002. Microbial diversity of hydrothermal sediments in the Guaymas Basin: Evidence for anaerobic methanotrophic communities. Appl. Environ. Microbiol. **68**: 1994–2007. doi:10.1128/AEM.68.4.1994-2007.2002

Thauer, R. K., and S. Shima. 2008. Methane as fuel for anaerobic microorganisms. Ann. N. Y. Acad. Sci. **1125**: 158–170. doi:10.1196/annals.1419.000

Treude, T., S. Krause, J. Maltby, A. W. Dale, R. Coffin, and L. J. Hamdan. 2014. Sulfate reduction and methane oxidation activity below the sulfate-methane transition zone in Alaskan Beaufort Sea continental margin sediments: Implications for deep sulfur cycling. Geochim. Cosmochim. Acta **144**: 217–237. doi:10.1016/j.gca.2014.08.018

Treude, T., J. Niggemann, J. Kallmeyer, P. Wintersteller, C. J. Schubert, A. Boetius, and B. B. Jørgensen. 2005. Anaerobic oxidation of methane and sulfate reduction along the Chilean continental margin. Geochim. Cosmochim. Acta **69**: 2767–2779. doi:10.1016/j.gca.2005.01.002

Treude, T., V. Orphan, K. Knittel, A. Gieseke, C. H. House, and A. Boetius. 2007. Consumption of methane and CO_2 by methanotrophic microbial mats from gas seeps of the anoxic Black Sea. Appl. Environ. Microbiol. **73**: 2271–2283. doi:10.1128/AEM.02685-06

Treude, T., and W. Ziebis. 2010. Methane oxidation in permeable sediments at hydrocarbon seeps in the Santa Barbara Channel, California. Biogeosciences **7**: 3095–3108. doi:10.5194/bg-7-3095-2010

Tsien, H. C., B. J. Bratina, K. Tsuji, and R. S. Hanson. 1990. Use of oligodeoxynucleotide signature probes for identification of physiological groups of methylotrophic bacteria. Appl. Environ. Microbiol. **56**: 2858–2865. doi:10.1128/AEM.56.9.2858-2865.1990

Turrell, W. R., E. W. Henderson, G. Slesser, R. Payne, and R. D. Adams. 1992. Seasonal changes in the circulation of the northern North Sea. Cont. Shelf Res. **12**: 257–286. doi:10.1016/0278-4343(92)90032-F

Valentine, D. L. 2011. Emerging topics in marine methane biogeochemistry. Ann. Rev. Mar. Sci. **3**: 147–171. doi:10.1146/annurev-marine-120709-142734

Vartoukian, S. R., R. M. Palmer, and W. G. Wade. 2010. Strategies for culture of 'unculturable' bacteria. FEMS Microbiol. Lett. **309**: 1-7. doi:10.1111/j.1574-6968.2010.02000.x

Vazquez, A., I. Leifer, and R. M. Sánchez. 2010. Consideration of the dynamic forces during bubble growth in a capillary tube. Chem. Eng. Sci. **65**: 4046–4054. doi:10.1016/j.ces.2010.03.041

Vielstädte, L., M. Haeckel, J. Karstens, P. Linke, M. Schmidt, L. Steinle, and K. Wallmann. 2017. Shallow Gas migration along hydrocarbon wells–An unconsidered, anthropogenic source of biogenic methane in the North Sea. Environ. Sci. Technol. **51**: 10262–10268. doi:10.1021/acs.est.7b02732

Volta, A. 1777. Volta letters on flammable Air of Marshes.

Wäge, J., O. Schmale, and M. Labrenz. 2020. Quantification of methanogenic Archaea within Baltic Sea copepod faecal pellets. Mar. Biol. **167**: 1–7. doi:10.1007/s00227-020-03759-x

Wäge, J., J. F. H. Strassert, A. Landsberger, and others. 2019. Microcapillary sampling of Baltic Sea copepod gut microbiomes indicates high variability among individuals and the potential for methane production. FEMS Microbiol. Ecol. **95**: 1–13. doi:10.1093/femsec/fiz024

Wallace, G. T., and R. A. Duce. 1978. Transport of particulate organic matter by bubbles in marine waters 1. Limnol. Oceanogr. **23**: 1155–1167. doi:10.4319/lo.1978.23.6.1155

Wallmann, K., E. Pinero, E. Burwicz, M. Haeckel, C. Hensen, A. Dale, and L. Ruepke. 2012. The global inventory of methane hydrate in marine sediments: A theoretical approach. Energies **5**: 2449–2498. doi:10.3390/en5072449

Wallner, G., R. Amann, and W. Beisker. 1993. Optimizing fluorescent in situ hybridization with rRNA-targeted oligonucleotide probes for flow cytometric identification of microorganisms. Cytometry **14**: 136–143. doi:10.1002/cyto.990140205

Wan, J., and J. L. Wilson. 1994a. Visualization of the role of the gas-water interface on the fate and transport of colloids in porous media. Water Resour. Res. **30**: 11–23. doi:10.1029/93WR02403

Wan, J., and J. L. Wilson. 1994b. Colloid transport in unsaturated porous media. Water Resour. Res. **30**: 857–864. doi:10.1029/93WR03017

Wan, J., J. L. Wilson, and T. L. Kieft. 1994. Influence of the gas-water interface on transport of microorganisms through unsaturated porous media. Appl. Environ. Microbiol. **60**: 509–516. doi: 10.1128/aem.60.2.509-516.1994

Wang, W., L. Wang, and Z. Shao. 2018. Polycyclic aromatic hydrocarbon (PAH) degradation pathways of the obligate marine PAH degrader *Cycloclasticus* sp. Strain P1. Appl. Environ. Microbiol. **84**: e01261-18. doi:10.1128/AEM.01261-18

Wang, X. N., G. X. Sun, and Y. G. Zhu. 2017. Thermodynamic energy of anaerobic microbial redox reactions couples elemental biogeochemical cycles. J. Soils Sediments **17**: 2831–2846. doi:10.1007/s11368-017-1767-4

Watanabe, H., K. Fujikura, S. Kojima, J.-I. Miyazaki, and Y. Fujiwara. 2010. Japan: Vents and seeps in close proximity, p. 379–401. *In* S. Kiel [ed.], The Vent and Seep Biota. Springer.

Weber, T., N. A. Wiseman, and A. Kock. 2019. Global ocean methane emissions dominated by shallow coastal waters. Nat. Commun. **10**: 4584. doi:10.1038/s41467-019-12541-7

Whelan, J., L. Eglinton, L. Cathles, S. Losh, and H. Roberts. 2005. Surface and subsurface manifestations of gas movement through a N–S transect of the Gulf of Mexico. Mar. Pet. Geol. **22**: 479–497. doi:10.1016/j.marpetgeo.2004.08.008

Whiticar, M. J. 1999. Carbon and hydrogen isotope systematics of bacterial formation and oxidation of methane. Chem. Geol. **161**: 291–314. doi:10.1016/S0009-2541(99)00092-3

Whiticar, M. J. 2020. The biogeochemical methane cycle, p. 1–78. *In* H. Wilkes [ed.], Hydrocarbons, Oils and Lipids: Diversity, Origin, Chemistry and Fate. Springer, Cham.

Wickham, H. 2009. ggplot2: elegant graphics for data analysis, Springer Verlag.

Williams, J. J., and C. P. Rose. 2001. Measured and predicted rates of sediment transport in storm conditions. Mar. Geol. **179**: 121–133. doi:10.1016/S0025-3227(01)00191-8

Wilson, D. S., I. Leifer, and E. Maillard. 2015. Megaplume bubble process visualization by 3D multibeam sonar mapping. Mar. Pet. Geol. **68**: 753–765. doi:10.1016/j.marpetgeo. 2015.07.007

Wilson, S. T., H. W. Bange, D. L. Arévalo-Martínez, and others. 2018. An intercomparison of oceanic methane and nitrous oxide measurements. Biogeosciences **15**: 5891–5907. doi:10.5194/bg-15-5891-2018

Winant, C. D., E. P. Dever, and M. C. Hendershott. 2003. Characteristic patterns of shelf circulation at the boundary between central and southern California. J. Geophys. Res. Ocean. **108**: 1-13. doi:10.1029/2001JC001302

World Meteorological Organization, and Atmosphere Watch Global. 2017. The state of greenhouse gases in the atmosphere based on global observations through 2016. World Meteorol. Organ. Bull. 1–4.

Yamahara, K. M., B. A. Layton, A. E. Santoro, and A. B. Boehm. 2007. Beach sands along the California coast are diffuse sources of fecal bacteria to coastal waters. Environ. Sci. Technol. **41**: 4515–4521. doi:10.1021/es062822n

Yang, S., X. Wen, and S. Liebner. 2016. *pmoA* gene reference database (fasta-formatted sequences and taxonomy). GFZ Data Serv. doi:http://doi.org/10.5880/GFZ.5.3.2016.001

Zhang, Y., and H. Xie. 2015. Photomineralization and photomethanification of dissolved organic matter in Saguenay River surface water. Biogeosciences **12**: 6823–6836. doi:10.5194/bg-12-6823-2015

Zhou, J., K. Mopper, and U. Passow. 1998. The role of surface-active carbohydrates in the formation of transparent exopolymer particles by bubble adsorption of seawater. Limnol. Oceanogr. **43**: 1860–1871. doi:10.4319/lo.1998.43.8.1860

Ziervogel, K., and C. Arnosti. 2009. Enzyme activities in the Delaware Estuary affected by elevated suspended sediment load. Estuar. Coast. Shelf Sci. **84**: 253–258. doi:10.1016/ j.ecss.2009.06.022

Zindler, C., A. Bracher, C. A. Marandino, B. Taylor, E. Torrecilla, A. Kock, and H. W. Bange. 2013. Sulphur compounds, methane, and phytoplankton: Interactions along a north-south transit in the western Pacific Ocean. Biogeosciences **10**: 3297–3311. doi:10.5194/bg-10-3297-2013

8 Acknowledgments

This thesis would not have been possible nor the same without the support and guidance of my supervisors Oliver Schmale, Gregor Rehder, and Heide Schulz-Vogt from the Leibniz Institute for Baltic Sea Research and Tina Treude from the University of California, Los Angeles. With these lines I would like to thank them for the wonderful time and experience we shared together.

I thank my thesis committee comprising Oliver Schmale, Heide Schulz-Vogt, Gregor Rehder, Ulf Gräwe, and Jens Schneider von Deimling for their guidance, constructive criticism, and support throughout the time of my dissertation.

Discussions and lively exchanges of knowledge in the working groups Trace Gas Biogeochemistry (IOW), Geomicrobiology (IOW), Marine Geomicrobiology (UCLA), Uta Passow's lab (UCSB), Bubbleology Research International (BRI), and the Graduate Research College Baltic TRANSCOAST (University of Rostock) has nourished and shaped this work. I appreciated this interdisciplinary environment and am thankful to be a part of this scientific community as each field represented a facet of the project.

Furthermore, I thank Stefan Otto, Christian Meeske, Christin Laudan, Michael Glockzin, and Julia Sweet for their support in the laboratory. I thank Janine Wäge-Recchioni, René Janßen, Johannes Werner, and Stefan Krause for fruitful discussion and their help with genetic and molecular biological methods, and analysis. I thank Eefke van der Lee for her support and analysis of water currents and Ulf Gräwe for the Lagrangian modelling.

I am grateful for all the support of the captain and crew of RV Poseidon (POS504), and thank Christoph Pierre, Christian Orsini, Eric Hessell, Andreas Frahm, Jens Müller, Sebastian Krause, and Jiarui Liu for support during scuba dives and fieldwork.

A huge thank you goes to all my friends and fellow PhD students/sufferers Jana Geuer, Sebastian Krause, Erik Jacobs, Theresa Grunewald, and Laura Käse.

I thank my family, who supported me on my life's journey, the friends I made along the voyage, and my beloved partner in life, karate and science Juliane Gottwald, who never gets tired of motivating and supporting me, and always enriches my life with new projects, adventurous hikes, and her mere company.

This thesis was conducted in the framework of a multidisciplinary project funded by the German Research Foundation (DFG, SCHM 2530/7-1 and SCHU 1416/1-4) at the Leibniz Institute for Baltic Sea Research Warnemünde (IOW).

9 Eidesstattliche Erklärung

Doktorandinnen/Doktoranden-Erklärung gemäß § 4 Absatz 1 Buchstaben g und h der Promotionsordnung der Mathematisch-Naturwissenschaftlichen Fakultät der Universität Rostock

Name: Sebastian Friedrich Alfons Jordan, geb. 08.08.1988

Ich habe eine Dissertation zum Thema:

Bentho-pelagic transport of methanotrophs at methane gas seep sites
Parametrization, identification, and contribution to the pelagic methane sink

an der Mathematisch-Naturwissenschaftlichen Fakultät der Universität Rostock angefertigt. Dabei wurde ich von Frau Prof. Heide Schulz-Vogt betreut.

Ich gebe folgende Erklärung ab:

1. Die Gelegenheit zum vorliegenden Promotionsvorhaben ist mir nicht kommerziell vermittelt worden. Insbesondere habe ich keine Organisation eingeschaltet, die gegen Entgelt Betreuerinnen/Betreuer für die Anfertigung von Dissertationen sucht oder die mir obliegenden Pflichten hinsichtlich der Prüfungsleistungen für mich ganz oder teilweise erledigt.

2. Ich versichere hiermit an Eides statt, dass ich die vorliegende Arbeit selbstständig angefertigt und ohne fremde Hilfe verfasst habe. Dazu habe ich keine außer den von mir angegebenen Hilfsmitteln und Quellen verwendet und die den benutzten Werken inhaltlich und wörtlich entnommenen Stellen habe ich als solche kenntlich gemacht.

Rostock den 02.08.2022